Precision Cold Forming Modelling,

Interfacial Thermal Parameter Investigation

and Tool Design Optimisation

Volume One

By

XUESHENG CHEN

This thesis is submitted to the Department of Design, Manufacturing Engineering and Management, University of Strathclyde for the degree of Doctor of Philosophy

Glasgow, January 2002

CONTENTS

ABSTRACT

Precision cold forming process modelling, thermal contact conductance and optimum shrink-fitted die with profiled interference were studied. The aims of this work have been achieved using analytical, numerical and experimental approaches to the relevant subjects. Several features of the work are presented: (i) an application of systematic modelling IDEF0 language, (ii) an equivalent asperity of surface that enables FE simulation of surface deformation and (iii) a shrink-fitted die with profiled interference, which enables compensation for component-error and necessary die surface pre-stresses.

Cold forming process was modelled systematically by IDEF0 language in general. The most often used iterations, including design and error-compensation procedures, were constructed; basic activities, inputs, resources and constraints were defined and decomposed. These provide a general procedure for precision cold forming design and a base for the following research of this work.

A thermal contact conductance (h-value) experimental investigation was conducted based on steady-temperature measurements and devices. h-value as a function of surface texture and interfacial pressure was experimentally investigated; typically, the value changes from $10\ kWm^{-2}K^{-1}$ to $150\ kWm^{-2}K^{-1}$ for changes in surface texture from $R_a = 0.3 \sim 0.5\ \mu m$ to $R_a = 3 \sim 5\ \mu m$, depending on interfacial pressure (<180 MPa). Based on surface measurements and mathematical work, an equivalent asperity for isotropic surface was presented to represent surface geometry. Uniqueness of the equivalent asperity enables simulation of surface deformation by FE technology. Surface textures under interfacial pressure up to 300 MPa were successfully predicted by FE simulations, results being in agreement with surface measurements. h-value is defined as a function of either contact area ratio or local interfacial pressure; a FE model and an approach of integration of local h-value were developed; value of h was successfully predicted by the established FE model and integration.

A profiled interference for shrink-fitting die was designed for component-errors compensation and die surface pre-stress. This was achieved by considering the relationship between die pre-deflection and the profiled interference by FE simulations and a minimisation procedure. Both, the equation and minimisation procedure to determine the profiled interference were established analytically. Uniform die surface direct compensation is combined with shrink-fitted die. Component-errors can be controlled to within a few microns.

ACKNOWLEDGEMENTS

The work presented here was carried out at the Department of Design, Manufacturing and Engineering Management, University of Strathclyde through a full-time study. Financial support provided by the University is gratefully acknowledged.

Firstly, the author would like to express his deepest gratitude and appreciation to his supervisors Professor Raj Balendra and Dr Y Qin for their invaluable scientific guidance, encouragement, support and care throughout his study, and meticulous checking of the manuscript.

The author is also sincerely grateful to Dr X Lu for his helpful advice, assistance and contribution to this work through many informative and beneficial discussions on numerical issues and computer problems. Thanks and gratitude are also due to Mrs. Rosochowski for her indispensable contribution and support in the experimental investigation, to Dr K. Chodnikiewicz for his smart design of experimental device, and to all other laboratory staff for their skilful technique support throughout the experimental research.

Lastly, the author's recognition must go to the colleagues of Manufacturing Engineering Research Group for their encouragement and constant support that provided a friendly research environment for the investigation of this work.

Chapter One

Introduction

1.1 Nomenclature

C	Material constant determined by experiment
m	Material constant determined by experiment
N	Number of loading cycles to initiate cracks
S	Strain or stress amplitude during a loading cycle
a	Length of crack
ΔK	Stress intensity
σ^*	The largest tensile principle stress
ε	General strain in the direction of σ^*

Subscripts

1	Constant one
2	Constant two

1.2 Cold forming development and trends

Cold forming is a process in which raw material is transformed into the near-form of an engineering component at room temperature. Precision cold forming refers to the configuration in which "ready-to-assembly", nett-form or near nett-form component, as more often used in literature, are manufactured. Nett-forming [1] is a relative term and is open to interpretation depending on the current expectation of a particular forming process. However, the features of all precision forgings operation are improved surface finish, without a draft, without flashes or webs, inclusion of shape details that traditionally are incorporated by machining and, higher and consistent dimensional accuracy.

1.2.1 Work-materials development

Minimum material consumption, high dimensional accuracy, good surface quality, mechanically high-strengthened components, and most importantly, higher productivity, have led to rapid growth of precision cold forming technology [2]. Fig 1.1 shows types of work-materials usable vs. time in cold forming. Earlier cold forming activities mainly concentrated on manufacturing gold, silver, copper and brass components. Modern cold forming of both, ferrous and non-ferrous metals, become feasible due to the invention of phosphate coating by Singer [2]. Today, not only aluminium and its alloys, but also low-carbon steels, special heat- and corrosion-resisting steels, medium-carbon steel, and even stainless steel and some non-metal materials are cold formed. It is predicted that more materials that are currently not formable will be cold formed in the near future due to the development of tool materials, effective lubricants and progress of processing configurations.

1.2.2 Processes development

A trend in cold forming is the development of new, complex and multi-stage cold forming processes and the required tooling. Traditionally, cold forming has been restricted to small, symmetrical parts made from low carbon steel or non-ferrous metals because the stresses required to deform the work-material at room temperature was relatively high [2]. In recent years, larger, more complex parts have been successfully cold-formed as a result of the improvement of forming equipment and the development in die- and work-materials, heat treatment, die coatings and lubricants, and the progress in new process design. Fig. 1.2 shows typical cold-formed automotive components [12-14]. Most of these had been hot-forged components in earlier decades. This new cold-forming process development was possible, in part, because of the design support provided by numerical simulation techniques.

1.2.3 Development of numerical simulation techniques

Conventionally, developing tooling for a new cold-formed component is a difficult, time-consuming and expensive task [15]. Preliminary tool design is followed by validation trials. The formed component is measured and the tool geometry is

modified to iterate towards the designed component form. This procedure is expensive due to tooling modifications for every iteration. This characteristic of cold forming rendered it only suitable for mass-manufacturing of engineering components. Fortunately, numerical simulation techniques provide the scope for shortening this costly iterative procedure. Process simulation is applied to enable detailed process information, such as stress- and strain-distributions, pressure contour, displacement, forming-force history and final formed component-form. This technique can also predict forming problems such as laps, folds and micro-cracks [16]. The geometry of the final component-form provides information necessary to modify the tooling instead of costly validation trials; the stress-distribution in tools may be used to assess the viability of tool design. Obviously, numerical simulation, as a tool, has partly replaced conventional trial-and-error cold forming process design. Numerical simulation is occasionally refereed to as numerical experimentation. However, necessary trial iterations are still required because of difficulties in acquiring accurate input data for FE simulations. Numerical simulation has become a development tool in R&D, as well as a design tool in forging.

Numerical simulation is also employed to predict tool life and component microstructure, and different numerical simulation methods are being used in current precision cold forming; these will be reviewed bellow.

1.3 Technological requirements of precision cold forming

Component-forms achievable by cold forming depend on the techniques to be used, for example, the tooling developed by Vazquez et al [17] made the hot-formed inner-racer to be cold-formable; more accurate profile of spur gear with smaller forming load was obtained by the novel cold forming processing design by Choi [12]. Development of new techniques may mean more available precision cold-formed components.

Materials First of all, cold forming processing design significantly depends on knowledge of materials, including both tool- and work-materials. Currently available work-materials require more advanced tool-materials and tool construction

techniques [5,7]. Although there are many advantages of cold forming over other forming processes, the cold forming tool must be able to sustain larger stresses and severe friction on die surface during forming. Thus, a tool-material for cold forming has to be tough, hard and wearing resistant.

The availability of high performance tool-materials is important to the practice of cold forming. The formability of work-material is also a key factor of cold forming design. Knowledge of forgeability of work-material continues in progress. In fact, the development of tool-material and lubricant would result in new cold-forgeable materials that were not cold forgeable before. For example medium-carbon steel and stainless steel are now available cold forming work-materials [6-11]. The forgeability of material is dependent on the forging process configuration, strain-path and the stress-state. The hard and brittle composite material Al/SiCp was successfully cold formed into a gear [18] without defects by the introduction of a high hydrostatic stress into forming process. The relation between formability and forming strain-path and the stress-state is worth investigating.

Tooling Tool design and forming process design, closely related, are important economically and for accuracy. Tooling configuration is often a dominant factor determining work-material flow pattern. A typical such example was provided by Vazquez et al [17], in which carefully designed tool structure enabled material to flow in expected pattern, thus quite complex component was cold-formed. Cold forming process and tool design normally includes forming sequences design [19], tool materials selection, tool geometry and forming-parameters determination [12]. The tool design and the processes rely on a clear understanding of stress and strain distribution in the tool during cold forming and the work-material flow pattern in the die-cavity. The design of an advanced nett-forming process has to consider the means by which high dimensional accuracy can be achieved.

Lubrication The resistance to deformation of the work-material at low working temperature leads to high contact pressures, resulting in high/severe friction and wear. Further, billet surface expansion in cold forming could be as high as 3000%

[20]. Lubrication procedure should be used for cold forming process. Conventional lubricants, such as gear, worm and ISO VG oils [21], or mineral oil hydrocarbons [20], are not always suitable in this case. The application of conversion coatings, such as zinc phosphate, zinc iron phosphate, calcium aluminate and aluminium fluoride coatings [20], acting as lubricant carrier, is necessary.

Error-compensation A fundamental problem faced by precision cold forming is form-error compensation. A cold-formed component is often not an exact negative of the die cavity surface. A difference between component-form and die-cavity form is inevitable; component-form error is the result of this difference. Component-form error arises from tool behaviour during cold forming, tool- and work-material properties, as well as the process-related parameters. Although cold forming takes places at room temperature, plastic deformation energy and energy generated by friction at the tool/billet interface may lead to increases in tool and billet temperature; temperature as high as 600 $^{\circ}C$ have been reported [1]. This temperature increase will lead to thermal expansion and subsequently contraction of both, the tool and billet. Thus thermal properties of tool-material, work-material and thermal contact properties at the tool/billet interface will also influence the final component accuracy [22]. The overall component-form error is the result of die elasticity, temperature, billet elasticity and Secondary Yielding which refers to the possible yielding after withdraw of punch during forming and was reported by Rosochowski and Balendra [23]. The traditional component form-error compensation approach is by modifying the die cavity geometry with reference to direct measurement of component-form errors, or changing the forming physical parameters, such as lubrication conditions [24].

Forming equipment. Forming equipment parameters also influence the cold forming process. Several press parameters will effect the final component accuracy, the most important of these being machine frame stiffness, perpendicularity of slide stroke against bolster top surface, parallelism between slide bottom and bolster top surfaces and clearance at slide guide. They may influence the motion accuracy of slide, and further affect the accuracy of formed component [25].

The feasibility of cold forming relies on tool-material properties, forgeability of work-material and suitable lubrication conditions; the expected product depends on tool geometry design and effective approach to component form-error compensation. However, these technique requirement analyses are only part-job of process design decisions. The practical process decisions in cold forming include choosing a forming sequence, tooling configuration, selection of equipment, lubricant and post-forging treatment, such as heat treatment or machining.

1.4 Research and development of precision cold forming

1.4.1 Research in cold forming processes

The application of cold forming has grown because of the development of modern cold forming technologies. Different kinds of forming configurations for cold forging have resulted in more precision components appearing in the market.

Onodera [26] showed the current range of automotive components manufactured by Aikoku Alpha Corporation. – refer to Fig. 1.3. These quite complex nett-form components illustrate the combination of extrusion, upsetting, and other cold forming processes to form multi-stage cold-forming operations. Shivpuri et al [9] investigated the cold forming of fuel injector nozzle for combustion engine from stainless steel. – refer to Fig. 1.4a. It had previously been manufactured by machining from AISI 8620. High injection pressures are required to fuel to achieve better combustion in the engine. These high pressures impose severe strength and corrosion-resistant requirements on the sac region of the nozzle. Thus stainless steel M501 or the equivalent was selected as work-material. Numerical techniques were employed to simulate the feasibility of different forming processes, the conclusion being that direct extrusion, reverse coining, double extrusion, to form the sac region were not practical. The successful multi-stage forming sequences are shown in Fig. 1.4b. However, work-material was assumed to be rigid-plastic and tool material to be rigid for the FE simulations, which would influence the accuracy of simulation results.

Osakada et al [27] presented a novel approach in which axially driven container was used to improve die-cavity filling of cold extrusion processes, including radial extrusion and backward/forward can-can extrusion. – refer to Fig. 1.5. The container oscillates with given frequency and amplitude during forming. It was claimed that the movement of container improved metal flow into the die cavity. The approach was validated by FE simulation and experiments. Fig. 1.6 compares forging forces under different container movements with the same filling conditions and punch stroke. The reduction of forming force can be observed. It was assumed that the friction coefficient at tool/billet interface was 0.25 for radial extrusion and 0.13 for forward/backward can-can extrusion; lubricant conditions were not specified. Although a "movable container" was referred to [27], it was, in fact, in direct contact with the billet in both extrusion cases, as shown in Fig. 1.5. Thus the inner surface of the container is part of die surface. This kind of "movable container" under very high contact pressure is difficult to design in practice and more energy may be consumed due to the relative movement between billet and the container. Practical tool configurations of this complex structure with actively "movable container" relative to billet is difficult to design.

Aida Engineering Ltd. of Japan [28] combined sheet forming and cold forming to produce near nett-formed components with reduced forming force. Fig. 1.7a shows examples of such components that were formed by blanking, drawing, ironing and sizing. Its benefits are obvious, drawing to replace usual extrusion, sizing to achieve dimensional accuracy with reduced forming load. Fig. 1.2b and Fig. 1.7b~d show a complex automotive components manufactured by machining and by cold forming [13]. The forming sequence of the flanged cylinder is shown in Fig. 1.7d. Fig. 1.7c compares between machined and cold-formed components. Cold forming not only reduces the weight of this component, but also increases the strength of the component due to work hardening.

Choi [12] studied the cold forming of spur gears, one of which is shown in Fig. 1.2a. Conventional guiding type and clamping type processing, as shown in Figs. 1.8a~b, requires large forming forces, often with filling defects at top of tooth even for

aluminium alloys. It was predicted that if alloy steel (SCM415) spur gears were cold formed in the same way, greater forming forces and more defects could be expected. The newly designed two-step cold-formed steel spur gear process is schematically shown in Fig. 1.8c. During the first step, a toothed punch moves down, forcing the work-material to flow in a controlled manner in the toothed die-cavity. The ejector is changed during the second step, in which the toothed punch continues to move down to the lowest position. FE simulation was used to obtain the best up part geometry of the ejector and the toothed punch stroke at which to change the ejector. Limited by the software and hardware, teeth of the gear were ignored during FE simulation to enable two-dimensional analysis possible. Thus, the spur gear was simplified into a cylinder. The errors caused by this simplification were difficult to predict. The final successful product is shown in Fig. 1.2a. The change of ejector during forging process is quite a big disadvantage of the design, as it requires quite complex tooling configuration.

Complex configuration would be required to let punch move down and rotate precisely at the same time under forging load. The toothed punch is, thus, not usually used to cold form helical gear, as reported by Park and Yang [29] due to the spiral form of teeth. A type cold forging process, as shown in Fig. 1.9, was employed successfully to cold form steel helical gears. The billet, product and tooling configuration are shown in Figs. 1.9a~b. 3D FE simulation was used to simulate the forging process.

Lee et al [30] investigated the cold forging of a constant-velocity joint housing used in the transmission system of car, as shown in Fig 1.9c. The billet is shown in Fig. 1.9d. Two different forging sequences labelled case II and I respectively, are shown in Fig. 1.9e. In sequence I, the billet was forward extruded to form a shaft in the first operation and upset in the second. The head was compressed by closed-die forging to form a flange with a radius approximately to the outer diameter of the cup. After annealing, so as to give the preform the required degree of cold formability, backward extrusion was performed. A second annealing was necessary due to work hardening. The fourth operation was a deep backward extrusion. And finally for a

more accurate component, an ironing operation was carried out. In sequence II, a closed-die-forging operation was used to replace the upsetting and the first backward extrusion in sequence I, thus saving one annealing process. FE simulation was used to validate the formability of the forging sequence design. However, the socket details inside the housing were ignored to enable 2D FE simulation. At the same time, rigid-plastic FEM was used. Thus, elasticity of the billet and tool was ignored. This approach is only suitable for the case where high form-accuracy is not required and determined.

Forward-rod/backward-can extrusion is popular forming configuration in the cold forming industry. Controlling material flow in two directions in a specified given ratio is a difficult task. Kuzman et al [31] used FE simulation to investigate this complex forming process. The forming force in this case determines material flow pattern. The required forming force for backward extrusion varies much more rapidly than that for forward extrusion. Thus, as shown in Fig. 1.10, forward extrusion occurs first. The situation remains till the forming force is large enough to initiate backward extrusion. Then flows in both directions occur simultaneously. In the circumstance where the extrusion force does not reach a sufficiently high value, backward extrusion would not occur. The most forming force sensitive parameters in extrusion are work-material properties, frictional condition and extrusion ratios. Different parameters were used in FE simulation for modelling material flow. It was concluded that material property does not influence the direction of material flow. Friction is the most important process parameter that affects material flow. The results of FE simulation are shown in Fig. 1.11. If process conditions are favourable for the formation of both, the rod and cup, the friction value must lie inside the triangle confined by three dotted lines. This calibration curve was validated by experiments. However, it is still difficult to design a material flow pattern for the combined extrusion process due to the dependence on friction coefficient. Friction coefficient changes continuously with lubrication conditions, surface geometry, wear and even temperature.

Vazquez et al [17] designed the process for the forming of the inner race used in vehicle transmission systems. The function of the component is quite similar to the inner race of a bearing. The component and the corresponding tooling are shown in Fig. 1.12. First the conical ring moves down to configure the die cavity. Then both inner punches move toward each other and outer punches retract; material flows radically to form the race. Finally both the outer punches move toward each other and inner punches retract to let material flow both outward and inward to form the final product. Rigid-plastic FE simulation and physical modelling were used to simulate the die-cavity filling. How the required high dimensional accuracy was achieved was not mentioned.

Yoshimura and Tanaka [10] described many precision cold-formed automotive components of steel and aluminium, as shown in Figs. 1.13a~d. The typical tooling configuration for bevel gears is shown in Fig. 1.13e. The technique requires controlling the speed ratio of the upper and lower punches. The optimum speed ratio was established in iteration. Although technical details were not reported, the products have shown to appear to be successful nett-forms.

The parts discussed above are only a few of the examples presented in the late a few years on cold forming processes investigation and industrial practice. As a result of developments in cold forming, components with more complex geometry, higher form-accuracy, and tougher strength requirement are being manufactured by precision cold forming processing. The direct consequence of these efforts is the rapid development and appearance of more and more complex cold forming processes and tooling configurations, especially multi-stage processes, and the combination of different basic cold forming operations.

1.4.2 Development of work-materials

Kaiso et al. [32] reported the application of cold forming for the production of a structural component for machinery, from medium carbon steel with or without spheroidisation. Usually, medium carbon steel is softened, by carbide spheroidising, before cold forming; in the absence of such treatment cracks might be initiated

during a cold forming operation. The cold forgeability of medium carbon steel that had not been completely spheroidised was studied using a cold upsetting test. The fracture limit increases with the increase in strain-path slope of the circumferential strain versus axial strain diagram. Better cold forgeability, by shortened spheroidising, was observed in the specimen with greater strain-path gradients. This suggests that the cold forgeability of incompletely spheroidised steels can be improved by suitably designed strain-paths. Thus the prospects of manufacturing medium carbon steel structures by cold forming are high. Similar research was conducted by Janicek and Maros [35]. However, how to apply the experimentally proven strain-paths to the design of cold forming process requires further investigations.

Metal matrix composites (MMCs) have mechanical properties which are superior to unreinforced metal. The mechanical, physical and chemical properties can be tailored for different applications by incorporating different types of reinforcements. Components with special performance could be obtained by cold forming metal matrix composites. Cold die-forming of Al-based metal matrix composites reinforced with 10% - 15% volume of SiC particulates have been successfully conducted in the manufacturing of gears [18]. Normally, MMCs exhibit brittle behaviour, and non-uniform deformation will lead to the initiation of fracture during processing. Plastic deformation under high hydrostatic pressure was adopted to enable the forming of components from these brittle composites without initiation of defects. Microstructural analysis has revealed a reduction in grain size, a decrease in defects and the fracturing of the secondary phase and SiC particulates. Large crystal distortion due to plastic deformation enhanced the mechanical properties, for example, the hardness of the gears formed from MMCs material had been found to increase from HB80 to HB138. Microstructural analysis has shown that microvoids and cavities were reduced by cold forming. However, it would be difficult for an engineer to apply isostatic pressure into a cold forming process to achieve the required minimum pressure of 650 MPa.

Bay [3], Yoshimura and Tanaka [10] and Siegert et al [33] summarised the wide applications of cold forming of aluminium, aluminium alloys and steels. The needs for cold-formed aluminium alloy components in industry have paced the ongoing development of cold-forming technology. Precipitation hardened alloys components which have significant strength to weight ratios are currently comparable in performance to those manufactured from unalloyed steel. Fig. 1.14 shows a pre-stressed die design, used in cold forming of aluminium and aluminium alloys, and the typical aluminium and al-alloy components. Not only aluminium and aluminium alloys, steels are also widely applied as cold forging work-materials. Typical steel cold-forging components are shown in Fig. 1.13 as examples.

Components, produced by compaction of metal powder, have relatively poor mechanical properties due to porosity, but quite complex component geometry can be achieved with fewer die-filling problems than in forging from billets. Further, cold forming the preforms manufactured in this way, can have a minimum or even no porosity. The mechanical properties of the metal-powder products manufactured in this way are comparable, and in some cases even superior, to those of cast and wrought products. Thus, combining powder-compaction technology with cold forming can produce geometrically complex high quality products [34]. The cold forming of these powder-compacted preforms is different from that of conventional materials; the variation of forming force with height reduction during upsetting is shown in Fig. 1.15, and is different from that for upsetting common engineering materials, particularly volume variation during upsetting. More research on forgeability and properties of this kind of powder-compacted preforms to achieve precision cold-forming products is required before mass production.

The classical approach for producing high strength fasteners is by cold forming annealed steel wire into the required geometry, followed by, usually, a time-consuming quench-and-temper heat treatment process to achieve the target mechanical properties. If fasteners are made from work hardening carbon steel, the required mechanical properties of fasteners are obtainable by suitably designed cold forming process. Thus, wire annealing and quench-and-temper heat treatment

processes can be saved. Goss [7] investigated successfully this new fastener cold forming process. Not all kinds of fasteners can be produced in this way and reach the expected component properties by plastic deformation because of the limitation of types steel stock which can be provided.

A measure of cold forgeability of work-material remains elusive; an effective measure would assist designers of cold forming process. Janicek and Maros [35] proposed an approach for experimentally determining cold forgeability of work-material; there are similarities with the approach adopted by Kaiso et al. [32]. This approach was used to investigate the forgeability of heat-resistant steel X25CrNi24.20, corrosion-resistant steels X8CrNiTi8.11 and X6CrNiTi8.11. Plastic deformation (compression) of work-material in upsetting is usually limited by free surface cracking. Thus, the strain-state, under which free surface cracks are initiated, can be a measurement of ductility of the work-material. The upsetting test is thereby a coarse approach for characterising cold formability of work-materials. For example, the maximum obtainable reduction in height in upsetting operation, such as heading, is limited by the onset of cracking on the free expanding surface. The maximum reduction depends upon upsetting conditions and material ductility. Failure limit diagrams (FLD) were produced using upsetting tests. For these tests, a cylindrical specimen with an axial notch on the free surface was used. The devised FLD for one of the material is shown in Fig. 1.16 with the symbols defined in the diagram. Strain-path below the dashed line is feasible without the onset of fracture. Theoretically, when the strain-path traverses the dashed line, surface cracks would occur. The strain-path is defined by the forming conditions, such as contact conditions, current geometry of the workpeice and properties of the material. Using this approach, the forgeability of three materials was assessed. However, upsetting test experience suggests that specimen would not remain exactly axisymmetrical due to anisotropy; notches are rarely of the same configuration to be repeatable means of initiating fracture. This being the case, it is difficult to measure sizes referred to and to establish the initiation of fracture. The applicability of the findings to cold forming process design, for example, to determine the maximum reduction ratio of forward extrusion without initiation of cracks, requires further research.

The introduction of cold plastic working of polymeric materials depends on the development of techniques to overcome elastic recovery and dimensional changes with the lapse of time. The cold-rolled solid polymer billet was subjected to heat treatment in boiling-water bath after forging into a component [36]; this procedure reduced elastic recovery of cold-formed polymer components. Fig. 1.17 shows the elastic recovery after cold-upsetting the cold-rolled specimen with different area reduction ratios, and examples of cold-formed products, the dimensions and forms of which were similar to the corresponding metal products. Obviously, using billet with big area reduction of pre-rolling treatment, recovery after forming can be efficiently reduced. This investigation showed that a cold rolled preform is an essential requirement for the cold forming of polymers. However, there is a gap between the scopes of current processes and the requirement, in terms of accuracy.

Since the appearance of cold forming processes, the range of cold forming work-materials has expanded continuously. Progress has been made since the days when soft gold and silver were cold formed; hard medium-carbon steel and stainless steel are currently cold formed. The range of work-material depends not only on knowledge of the forgeability of materials, but also on the development of tool-material, lubrication, and the forming process configuration.

1.4.3 Tool materials and tool life

Tooling is one of the main cost contributors to a precision cold forming operation. Significant research has been conducted on tool materials and tool life.

Investigation of tool materials includes research into the behaviour of available materials and the formulation of new materials. In cold forming tool design and fabrication, high strength, strong fracture toughness and tough wear-resistant tool-materials (substrate) are requirements; further coatings, such as TiN, TiC and CrN are used to enhance abrasion resistance. The behaviour of the substrate and the coating may be understood by tool designer separately; however, the combination of substrate and coating, may have an unpredictable characteristic. Although most cold

forming process analysts assume that the cold forming tool is rigid or elastic during forming processes, plastic strain can occur locally in the tool. This local cyclic plastic strain is responsible for the initiation and propagation of tool cracks that finally lead to the fatigue failure of tools. Attention should be paid that elastic stress may also cause fatigue of tool material. Verleene, et al [37] investigated the combined substrate-coating behaviour, especially the plastic characteristics. Brinell hardness tests and inverse FE simulation techniques were combined to obtain the hardening law of the tool material AISI M2 with TiN coating. The main results are shown in Fig. 1.18. The hardening curves of the tool material AISI M2 and coating TiN, the FE geometry model are shown in Fig 1.18a. The comparison of hardening curve of AISI M2 coated with TiN and that without coating is shown in Fig. 1.18b. The combined hardening curve is not that of AISI M2, nor of TiN. The coating, although just being a few microns thick, plays an important part in die surface strength. However, it should be noted that in this research, the experimental results were obtained by recording the indentation load and the diameter of indentation on the test specimen. The measured indentation diameter was compared with that predicted by FE simulation to enable modification of the hardening law. The constitutive equation which enabled the matching experimental results to the FE simulation was assumed to be valid data. For most cases, the indentation would be not clear enough for accurate measurements. Besides, the trial-and-error modification hardening law in simulation will be quite time consuming and analyst-dependent, and the errors from measurement and FE simulation are difficult to control.

New tool materials are a great attraction to both tool designer and process researcher. Berns et al [38] developed a new cold forging tool material with two phases - a hard phase (HP) of particles distributed discretely in a continuous second phase produced by powder compaction. The HP phase is carbide; the second phase is a mixture of high-carbon and high-speed steel powder and hot-working tool steel powder. It was established that the overall material properties were closely related to the distribution pattern of HP particles. The basic idea was to find an optimised distribution of this two-phase material by simulating different distribution patterns of hard particles within the metal matrix. Both micro- and macro- FE simulations were used.

Continuum mechanics FE simulation was used to model the cold forming process to locate crack-risk location and its stress-state at a macroscale; meso-micromechanics FE simulation was used to simulate the stress-strain-state further. The distributions of the hard particles were simplified into a few patterns, - dispersion, net, double-dispersion and band patterns, in unit cell-, which identifies in the crack-risk location. The boundary condition of the unit cell depends on the stress-state obtained at the macroscale level. Usually, the unit cell is simplified as a plane stress or plane strain problem. The simulation showed that a double-dispersion distribution pattern of hard phase would provide the best fracture toughness. In order to validate this analysis, samples of the material were used as die-inserts for cold heading of bolts. Compared to a conventional die-insert, 6~8 times more forgings were formed before failure of the die-insert made from the new material. The detailed metallurgical process was not reported; the double-dispersion distribution pattern of the hard phase in metal matrix in practice remains unknown. Besides, the optimisation with FE simulation was confined to the selected distribution patterns of HP particles, which may not include the best consideration. In fact, the number of patterns of randomly distributed HP particles is infinite. Thus, the conclusions drawn are somewhat dependent on the selected distribution patterns of HP particles.

Besides the development of new tool-materials, research on techniques for improving available tool materials and coatings is being undertaken. Seidel et al [39] reported on a technique for ion-implanted hard coatings for cold forming tool surfaces. Hard coatings, formed by physical-vapour deposition (PVD) or chemical-vapour deposition (CVD) to improve wear resistance were effected with nitrogen, chromium and carbon ions. The mechanical property of a coating after ion-implantation treatment depends upon the coating material and the type of ion-implantation. Chemical-vapour deposited TiC-TiN coating implanted with N_2^+ showed significant reduction in the adhesion of the work-material to the tool surface. Comparison between ion-implanted coatings and unimplanted coating showed that after 20000 production cycles, no detectable transmitted material could be found on the implanted tool surface; by contrast, the work-material adhered to the unimplanted tool. Physical-vapour deposited Cr_2N coatings implanted with N_2^+ showed

substantial wear resistance. By comparative testing [39], it was showed that ion-implanted hard coatings would be attractive to future process designers. It has also been shown that the implanted material has a low coefficient of friction.

For the production of high-volume, cold-formed components of complex geometry, fatigue cracking of the active tool elements is the leading cause of disruption [40]. The tool life is usually much shorter than in the case of failure by wear [41]. Generally, a combination of cold forming process FE simulation with fracture mechanics is the approach used in cold forming tool life and fatigue analysis [40-42]. FE simulation is used to determine risk location and strain parameters. Software which can be used to simulate finite elastic-plastic deformation would enable the determination of the risk location and strain parameters during cold forming process simulation. However, most researchers [40-42] used a two-step approach to determine risk location and strain parameters. Rigid-plastic FE simulation is performed to obtain tool surface load as function of time, which is followed by the use of an elastic-plastic package, which is initialised using the tool surface load to determine risk location and risk stress/strain on the tool. The analysis of tool stress/strain, as function of time, leads to complex loading conditions. The choosing of the most risk load case, for example, the loading condition at end stroke for closed die forging, is controversial [40]. "Using the load at the end of the stroke could lead to misleading results in the stress analysis of the tooling" [40]. The load at 98.8% rated stroke was, therefore, used. The investigation conducted by Knoerr, et al [41] and Nagao, et al [42] contained examples of this type of analysis. Knoerr [41] investigated the fatigue cause of an axisymmetric forward extrusion tool. Nagao [42] carried out the similar research on an asymmetric forward extrusion tool. The conclusions were similar: the formation of plastic zone at transition radii is responsible for the initiation of cracks and the maximum tensile principle stresses propagate the initiated cracks. However, in both process and tool stress simulations, the tool geometry [42] was simplified significantly, from an asymmetric body into an axisymmetric body to enable 2D FE simulations. Although fatigue analysis is recognised as a capable tool for the prediction of tool life, more detailed material data, and the data under different heat-treatment conditions, providing the criterion

conditions for the cracking initiation and growth, is required [43-44]. Tool material data is scarce.

Tool fracture analysis includes the initiation and propagation of cracks. Together crack initiation and propagation cycles are the total tool life. The most often used theory of initiation of crack is Wohler's approach [43,44], which has the form:

$$SN^m = C \tag{1-1}$$

The failure crack growth starts when the stress intensity is ΔK, as described by Paris' law:

$$\frac{da}{dN} = C_1(\Delta K)^{m_1} \tag{1-2}$$

This equation is based on fatigue analysis theory under standard symmetrical cyclical load conditions [44]. Cold forming processes are too complex to enable the application of this theory for predicting tool life. Several crack initiation criteria have been derived for specific problems, as summarised by Pedersen [45]. The first is the effective plastic strain criterion: when effective plastic strain reaches a critical value, crack is initiated. The second measurement of fatigue damage is the plastic work per unit volume. And the last is referred to as Latham-Cockroft criterion:

$$\int_0^{\varepsilon} \sigma^* d\varepsilon = C_2 \tag{1-3}$$

The value of equation (1-3), used to judge crack initiation, was often referred to as damage value in literature [16]. All these criteria are being used in the fatigue analysis of cold forming tools and dies. Obviously, FE simulation is the only way to compute the damage value both economically and accurately. This is why nearly all cold-forming tool fatigue analyses is performed using FE simulation [40-49]. Falk [46] presented a local strain and local energy approach to determine the number of cycles of operation to initiate cracks in cold-forming tools, which required FE simulation to determine the local stress and local strain. Regardless of the criterion used for tool life prediction, the basic material constants are always the first essential data. Data on fatigue life of tools is not reported extensively. There is evidence of more research on tool life predictions than the basic tool-material behaviour.

In the research conducted by Pedersen [47], the plastic work, tensile elastic energy and mean plastic strain energy were taken into account to compute the damage value. Strip-wound pre-stressed-ring tool construction was used in FE simulations. However, no commercially available FE packages accommodate the analysis of strip-wound tools. Thus, the strip-wound construction was simplified to a general solid ring. Strip-wound containers have got to be defined in geometrical terms to enable the prediction of its behaviour during a forming cycle. To date, this definition has not been reported.

Ahn, et al [48] combined fracture growth theory (1-2) with FE simulation to investigate the crack-growth process. The effective stress intensity factor can be derived by FE simulation. Both, the crack propagation rate and the propagation direction can be simulated using local displacement fields. Crack develops in a zigzag radial path, which is similar to the trend found in experiments, as shown in Fig. 1.19. However, in the simulation of stress intensity factor, the contact pressure at the shrink-fitted interface was assumed to be constant, according to Lame's formulation. It is well known that the contact pressure at the shrink-fitted interface changes with time since the die-cavity contact pressure contour is not constant. Besides, the root cause of zigzag development of cracks was not revealed.

Basic knowledge of cold forming tool fatigue has been well developed. Plastic strains initiate cracks and maximum tensile stresses develop cracks [40-42]. A few improvements to tools to enable tool working under high pressure have been reported in recent years, – as shown in Fig. 1.20. The stress ring approach shown in Fig.1.20d is the most popular construction technique to increase the strength of tools for cold forming [48]. However, such solid stress rings are limited by possible shrink-fitting interference. Strip-wound containers, involving quite large interference, manufactured by *STRECON Technology*, are shown in Figs. 1.20a~c. Uniform interference strip-wound (Fig. 1.20a), profiled-interference strip-wound (see Fig. 1.20b) and with axial pre-stressed construction (Fig. 1.20c) have also been developed [47~49]. Nagao, et al [42] presented an solid optimum stress-ring construction with profiled shrink-fitting interference, the FE mesh of which is shown in Fig. 1.20e; this

constitutes a substantial advance on the conventional use of stress-rings for cold forming tool design. Other methods of improving the fatigue strength of cold forming tools are to use high wear resistant and fracture toughness material for the die insert.

Cold forming tool material and tool life enhancements techniques can now enable the production of cold extrusion tool with a life of 20,000~100,000 components. However, for the objective of producing of components with larger dimensions, greater complexity, higher accuracy, better surface finish and tougher work-material of cold-formed nett-form component, improvement for longer tool life and more advanced tool-material remains a challenge. Progress in the configuration of cold forming process is dependent on tool-material development. New tool construction techniques will lead to improvement of existing processes or the development of new cold forming process.

1.4.4 Cold forging lubrication, coating and friction

Cold forging lubrication approaches. The tribological conditions between tool surfaces and billets during cold forming, especially for the production of nett-form components, are extremely severe due to large surface expansion and high interfacial pressure, combined with elevated temperatures. The cold forming of steel is effected with surface expansions of as much as 3000%, interfacial pressure at the tool/workpiece interface approaching 2500 MPa and an average tool temperature of $200^{\circ}C$ with local peak temperatures of $600^{\circ}C$ [50]. Direct metal-to-metal contact may lead to adhesion or pick-up. Conventional lubricants, such as gear and mineral oils [20-21], are insufficient for such applications. Successful cold forming operations, therefore, require more advanced lubricants. The basic requirements of lubricants for cold forming are to lower friction and prevent pick-up or galling; conversion coatings provide suitable lubricant carriers.

Different lubricants are required, depending on the different contact conditions. Bay [50] summarised the use of lubricants for cold forming. Complex surface-treatment of billet for lubrication is required for cold forming of C-steel and low alloy steel.

Initially, billets are cleaned, mechanically or chemically, in order to degrease and descale. The most often used mechanical cleaning approaches include blasting, peeling and scale breaking, suitable for different kind geometry of billets; chemical cleaning is effected by using water soluble salts and pickling. The phosphating process is applied during which zinc-phosphate or zinc-iron-phosphate coatings are formed on the billet. Phosphate coatings have to be used in conjunction with lubricants for cold forming. Due to physical and chemical reactions, the coatings adhere better to the billet. This improved adhesion prevents the breaking away of the lubricant film during sliding under high contact pressure and considerable surface expansion during forming. There are three types of lubricants for C-steel cold forming: soap, solid and oil lubricants. Normally, reactive soap lubricants are chemically bonded while oil and solid lubricants adhere physically. The billet surface structure, after lubrication treatment, is shown in Fig. 1.21a. With this structure, the lubricant can sustain large surface expansion and contact pressure without damage. However, this surface pre-processing and the post-processing present environmental control problems, and are also expensive.

Lubrication procedure for cold forming of aluminium and aluminium alloy is quite similar to that of C-steel. Treatments and lubricants are a foundation of both, material and forming process. Fig 1.21b summarises the choice of lubrication for cold forming aluminium and aluminium alloys.

Cold forming lubrication research Seidel [39] reported the research on ion-implanted hard coatings, which is reviewed in detail in section 1.4.3; this could also be considered as part of research into lubrication. A tool-material with sufficient self-lubrication is perfect for cold forming and the working environment. Ohmori, et al [51] developed the ball penetration test to assess the galling prevention function of different oils used in cold forming, as shown in Fig 1.22. The maximum radius of ball passing through the workpiece hole without galling defines the galling prevention capacity of the lubricant. Compared with conventional backward extrusion tests, ball penetration test is easy to perform and both, the specimen and the tooling, are inexpensive. Test results show that the data from the ball penetration test

could be correlated to the data from backward extrusion tests. However, in practice, ball and workpiece are discrete; and occasionally it is difficult to assess whether galling has occurred or not. It also difficult to obtain the exact maximum value of ball diameter under given lubrication conditions.

Temperature at the interface may rise as high as $400^{\circ}C$ during cold forming [22]. This high temperature will change the chemical and physical properties of lubricants and the carrier, which could modify the performance of lubricants. Steenberg, et al [52] investigated the lubrication film temperature during back-extrusion of stainless steel cans and its influence on the lubrication. Different punch force histories were observed due to different lubrication temperatures at which the phase transition of lubricant and the carrier may occur. Phase transition of lubricant leads to different lubrication performance, and would result in different friction coefficient; as a consequence, the forming force would change. From the microanalysis of lubricant and the carrier after forming, it was concluded that the interface temperature might reach as high as 450 $^{\circ}C$ when the extrusion ratio=2. The result is reliable because phase transition occurs at this temperature. However, this is only indicative.

Dubar, et al [53] developed a new experimental device to assess the performance of different coatings, as shown in Fig. 1.23. The device consists of a coated cylindrical sample which is rotated while a semicylindrical slider exerts a local pressure. The revolution number, electric contact resistance between slider and the sample and the torque required to drive the cylinder were recorded, as shown in Fig.1.23, for particular contact forces and rotation speeds. The revolution numbers *nt* and *ns* shows the anti-damage ability of the coating under given contact conditions. However, the anti-damage ability against surface expansion was not taken into account in this test. It is difficult to simulate the real contact conditions, including contact pressure, temperature, relative sliding and surface expansion during cold forming by local contact alone.

Meng and Wen [54] established a plasto-hydrodynamic lubrication model in which cold upsetting of a cylindrical billet was considered; this revealed the influence of

plastic deformation upon lubrication film. The results of simulation showed that pressure in lubricant could reach a value that is much higher than the yield strength of the work-material, and thus a concave depression full of hydrodynamic lubricant was formed between the tool and workpiece. However, the thickness of the lubrication film is usually of the order of microns and billet dimensions are of millimetre scale. In such a case it would be difficult to match the mesh of film with those of billet when FE simulation is applied [54].

Additives to lubricants may result in enhanced performance. Dong, et al [21] found that while cold-forming stainless steel products, the addition of organic borate into different gear oil ($150^{\#}$), worm oil ($46^{\#}$) and ISO VG oil ($68^{\#}$) or MoS_2 greatly improved performance thereby reducing wear. Stick-slip phenomenon which occurred was eliminated after adding suitable organic borates.

Nishimura, et al [55-56] evaluated friction at tool/billet interface by cold injection upsetting process, the conceptual diagram of which is shown in Fig. 1.24. Upper-bound analysis was used, and the frictional factors corresponding to different lubrication condition were expressed as the function of flange diameter D_F (Fig.1.24). Thus frictional data, more practical than data from ring compression test, was obtained for different lubricants, such as Dag, JF, MoS_2 and under dry conditions. The influence of strain rate, temperature and the lubricant mass, upon friction was also investigated. The frictional factor appeared to be independent of strain rate [55-56]. However, all these results were based on upper-bound analysis, which simplifies the behaviour of the tool and work-material; the tool was regarded as rigid while the work-material was rigid-plastic. Mechanical contact is a function of the material property. The influence of elasticity and work-hardening on the contact process was ignored in this research.

The friction coefficient/factor influences not only the forming process, but also the accuracy of component. The evaluation of friction upon tool/billet interface will be still a focused research point in the future.

1.4.5 Application of FE simulation in cold forming

1.4.5.1 FE development and general objectives

The application of FE simulation technology to model forming, mainly as research and development tool, started in the late 1960s [57]. During 1970s and earlier 1980s, two-dimensional steady forming process, such as drawing/extrusion of round bar and wide sheet rolling, which did not require remeshing, were analysed. FE simulation of more complex processes requiring remeshing to continue the analysis was developed much later. Mesh quality influences not only the accuracy of FE simulation outcome but also convergence of the process of simulation. Mesh deformation due to non-uniform metal flow, may terminate the analytical process unless remeshing was attended to. Between 1980s and 1990s, some of non-steady metal flow processes were simulated by manual remeshing. Since automatic meshing and remeshing technology was developed in the late 1980s and earlier 1990s, FE simulation of forming processes has been increased. Commercially available FE packages, such as Marc, Autoforge and DEFORM, remesh automatically; ABAQUS, to date, can automatically remesh for explicit analysis only. Remeshing does not only redefine the nodes and elements in the domain of workpiece geometry; all field variables, such as strain, stress, temperature and displacement, must be equivalently reorganised according to the new nodes and elements, as well. This reorganisation of all data is a time consuming and error-prone process [58]. To date, automatically remeshing is available for both, two-dimensional and three-dimensional problems [29]. Fig. 1.25 shows the mesh of a three-dimensional FE simulation of helical gear at a given moment. With the development of software and hardware, FE simulation is not considered as just as R&D tool to support forming process design [58]. Development trends are shown in Fig.1.26. The rapid development of FE simulation techniques are based on their capability of providing information which enables critical design approaches; Fig. 1.27 shows the information available from FE simulation and its advantages [57]. The main objectives of FE simulation can be summarised as follows [58]:

- checking die cavity filling
- preventing flow induced defects such as laps, folds, etc.
- predicting processing limits that should not be exceeded in order to avoid defects

- predicting and improving grain flow and microstructure
- reducing die try-out, leads times and reducing rejects.

1.4.5.2 Classification

FE simulation is often classified according to the materials constitutive equations. The use of different constitutive equations in FEM results in different FE simulation methods [59]. Work-material may be plastic or elastic-plastic; stress-strain curve may or may not include the influence of strain-rate and temperature; tool material may be rigid, elastic or elastic-plastic. For example, rigid-plastic FE simulation, in which the tool material is considered rigid and the work-material as plastic, is widely used in simulation of hot forging process, in which both the elasticity of the tool and billet are ignored. This allows high computational efficiency. For precision cold forming process simulation, the most common analysis involves thermo-mechanically coupled elastic-plastic FE simulation, in which the elasticity of both, tool- and work-materials, and temperature are considered in order to determine the component dimension accurately. If the analysis involves fatigue behaviour, work-material elastic-plastic properties, as well as tool-material elastic-plastic properties should be considered [35,38,40-49], although different techniques are employed for computational efficiency. To date, most commercially available FE packages allow users to define different materials properties, as well as subroutines for user-defined material descriptions.

1.4.5.3 Applications

Process simulation and design As was discussed in section1.4.1, nearly all cold forming processes, such as extrusion (forward/backward and radial extrusion), upsetting, ironing or sizing, and the combination of these, have been simulated using FE techniques. Process design, using simulation support, enables the balancing of many complex parameters to define a workable process; it also enables failure diagnostics. These parameters include the number of intended operations and forming sequences, required tools displacements, final component geometry, starting work-material dimensions, available forming equipment, and the final component-form error [60]. Besides, identifying the inherent latent process problems, such as

laps, unfilling or overfilling, overloading and cracking problems, are important aims of FE process simulations as well. Typical investigations and practical examples have been reviewed in section 1.4.1. FE simulation has been used to develop complex processes, such as inner race [17], helical gear [29], spur gear [12] and bevel gear [15].

Microstructure simulation Welo [61] presented an approach for establishing relationship between grain size and plastic strain. Initially, the axisymmetric extrusion of the process was simulated by FEM. After metallographic analysis of the extruded component, a correlation between strain distribution after forming and the grain-size was established. This suggests that by combining FE simulation with experimental measurements, the microstructure of components as function of plastic strain, can be defined; subsequent analysis relied on this correlation [61]. Grain size was empirically expressed as the function of strain; the tool form was optimised to obtain the most uniform grain size distribution in the component. The reliability of simulation depends on experimental data. Prior to the simulation of work-material microstructure, sufficient experimental data defining the correlation between microstructure and plastic strain has to be conducted. Specific research is required as this is absent from publications.

Microstructure may also be simulated using a combination of meso-mechanics and continuum mechanics FE techniques. Continuum mechanics FEM is used to determine the local stress or strain state of cold formed components in macroscale; meso-mechanics FEM is used to further analyse the local microstructure evolution under this stress state at meso-level. The element cell is given the distribution pattern of different phases prior to the simulation [38]. An optimum cold forging tool material was developed with 30% increase in fracture toughness; this was reviewed in section 1.4.3.

Cracking initiation simulation Micro-crack initiation prediction [18,63] by FE simulation has also been performed based on Cockcroft and Latham's crack criterion; a technique was presented to simulate crack initiation in cold-formed

components during forming. Thus, it is possible to predict both surface and internal crack defects in cold-formed components. However, the FE analyst faces the same problem as that encountered for simulation of microstructure. Effective prediction of crack formation, sufficient experimental data is required, particularly the material constants. This is why damage value was taken as a minimum objective of optimisation instead of the assessment of crack initiation [18].

Material separation simulation Material separation is defined as the propagation of the initiated crack. Thus material separation simulation refers to the modelling of crack growth. Taupin, et al [64] reported on material separation criterion and the corresponding material separation simulation technique. From fracture propagation point of view, investigation of material separation in blanking is of general significance. The McClintock fracture criterion was implanted in the FE package, DEFORM. The material damage value thus was evaluated according to McClintock criterion from element to element during FE simulation. If the damage value of an element was found to be equal to or greater than the **specified critical value,** this element would be deleted to form a local material separation (crack) after the subsequent remeshing. The coalescence of the local separations leads to the overall material separation. Fig. 1.28 shows material separation under different tool clearances. The material critical damage value was obtained by a reverse iteration method from FE simulation, i.e., modifying material critical damage value, until the simulation results have a good correlation to the experimental observation. The corresponding damage value was then defined as a material constant. However, only the geometry at the fracture location was compared visually with that of experiment, without comparing the parametric values reported, such as blanking force. This kind of fracture propagation simulation needs extremely fine meshes. Deleting an element will lead to finite variation of material volume and a finite length of crack at an instant instead of gradual growth of a crack; this conflicts with volume constancy considerations in plasticity theory and crack growth theories. Thus, this approach, if used in other cold forming operation, may introduce errors if the mesh is too coarse.

Tool design and tool life improvement FE simulation of cold forming processes provides tool stress and strain information during forming; these are necessary for the analysis of tool fatigue strength. Thus, the proximity considerations to failure types would be revealed at design stage. Different approaches for improving tool strength can be validated by FE simulation, or based on FE simulation to determine the optimum tool structure [40].

Optimisation Due to the complex boundary conditions of processes and non-linear constitutive models of materials, it is impossible to obtain analytical solution of a practical finite plastic deformation problem in cold forming; FE simulation can be a key tool for determining the related parameters or field variables. Joun [65] investigated the optimisation of axisymmetric forward extrusion, aimed at minimisation of extrusion force. Rigid-perfectly plastic work-material was used in the optimisation and co-ordinates of tool profile were selected as design variables. The result showed that friction is a major factor affecting the optimal die contour. Work hardening of work-material was ignored in the analysis. Duggirala, et al [66] conducted research to determine the optimal design for cold forming an automotive outer race; minimum damage value was set as the reference. Genetic algorithm optimisation technique, which is based on probabilistic transition rules, was used in the optimisation. Genetic algorithm is a searching approach to minimise objective. A relatively better scheme can be determined by comparison of objectives from current available schema and is kept; genetic algorithm operator reproduces new schema by reproduction, crossover or mutation from the current schema [67]. New comparison is conducted among the reproduced available schema for the better scheme again, until the process converges. Six die and process related geometric parameters were chosen as design variables for a forging process. Forming limits, avoiding defects, permissible forging force, were selected as constraints. The optimum result showed that the damage value of the component under optimised processes was reduced from the original 0.203 to 0.117. However, the original two-step cold forming process, as shown in Fig. 1.29, was increased to four steps. Forming cost would greatly be increased. On the other hand, the permissible damage value of the material used was unknown. If it was less than 0.203, the above optimisation is significant. If it was

much great than 0.203, then optimality is not of significance. Only two options were considered; whether either of these was the most suitable for the comparative study is not known.

Cold forming process optimisation is an expensive design process since the objective function is often forming process related, and hence repeated FE simulation validation of the design result is required [65-66].

State-of-the-Art. FE simulation of cold forming has advanced at a rapid pace over the past two decades. Ongoing developments and new applications continue to become available. The current process models account for elastic and plastic deformation, thermal influences, forming equipment and different contact conditions. Developments are in process that will allow users to analyse crack initiation and propagation, microstructure evolution, residual stress and spring back as well as thermo-mechanical influences. Full three-dimensional simulation is becoming available for more complex geometries. Automatic three-dimensional remeshing techniques are available on some FE packages. However, some basic research which supports the application of FE simulation, such as material data to describe material forgeability, fracture behaviour and specific techniques, for example profiled stress ring to improve die life and component accuracy, await further research. It can be expected that more complex three-dimensional cold forming processes can be simulated without cost and technical problems in the near future [58-59].

1.4.6 Cold forming component-errors and compensation methodology

1.4.6.1 Component-errors factors

Component-error analysis and error compensation is of critical importance to the implementation of precision cold forming. Component-errors are caused by different factors. Lange pointed out that factors affecting dimensions, form, surface, position, strength, and weight due to process, material, tool, machine, and process layout are numerous, and hence a thorough analysis is not possible [68]. A schematic representation in Fig. 1.30 gives several interacting factors with regard to workpiece accuracy.

First the **material** related factors such as the random fluctuations in work-material chemical composition, microstructure and grain sizes will affect the flow curve of the work-material. The result is a spread of the deformation forces and springback. Variations in the forming forces affect the elastic deflection of the tool and the forming machine directly and hence the dimensional accuracy (such as bottom and flange thickness). Dimensional accuracy can generally be improved though (1) careful heat treatment of billet, perform, or interstage; (2) favourable lubrication conditions; and (3) more rigid tooling.

Product accuracy is also sensitive to the initial sizes and volume of the billet. Volume fluctuations in the parting of bars are a result of variations in the cross sections, and the variations in the parted-off lengths (caused by the process). Volume variations in forming with closed dies result in force fluctuations with changing of elastic deflections of the tool and the machine. The danger of overloading exists when the used volume becomes larger than permissible.

Tools affect component accuracy in different ways. The accuracy of tools is very important for the accuracy of deformed products since forming is in a way coping in which the tool can be considered as analogy storage for the dimensions and shape. Deviations from desired values in the tool show up as systematic errors in the products. In production the dimensions of the tool change because of wear and deflection or deformation. The wear can be reduced by using wear-resistant tools and good lubrication. As a general rule, in tools subject to very high normal pressure there is a large region of linear wear pattern, –wear proportional to time, after an initial plastic deformation. Failure of the tool starts at the end of the linear region. Production tools must be changed before reaching this stage [68]. The tool deformation can be elastic or plastic. Plastic deformation occurs generally at the beginning of the production. The plastic deformation continues until the tool material gets sufficiently work-hardened. Selection of materials with large Young's modulus for cold forming tool is desirable with a view to decreasing tool deflection and increasing component accuracy.

Forming **equipment** parameters such as ram guidance, stiffness behaviour controlled by travel and force, and fluctuations in the work capacity of machines controlled by energy affect the accuracy of the formed products. A forming tool is generally made of two parts, one part is amounted on machine bed; the other is attached to the slide of the forming machine. Thus a proper guidance of the slide is important for good relative positional accuracy; or offset, different wall thickness, eccentricity of products may occur. The positional error of a tool is the sum of positional error of equipment during contact (without load) and the positional error due to drifting (under loading), resulting tilt. Guidance clearance, local elastic deflection of the guide and sideward tilt of the slide are root causes of positional error. An absolutely rigid press dose not exist. The frame and drive system components deform depending on their stiffness and forming load. For variations in the force transmitted because of changes in billet volume, lubricant, material properties, and so on, fluctuation in elastic deflections of the press will be smaller in a more rigid press. This is why rigid presses are used in processes of die-forging and coining. When a screw press is used in cold forming, the fluctuations in work capacity also influence the production accuracy, in particular the thickness dimensions of the products. The energy used for forming in every cycle is determined by the stroke that can be adjusted through control system of the machine [69]. Thus, in case of screw presses, either a stroke-limiting procedure or control of the screw speed can be used to control the work capacity.

Forming **process design and layout** greatly affect component form-error. The various factors of manufacturing that contribute toward achieving the designed accuracy are material, annealing, descaling, lubrication, temperature, interstage design and finishing process. By proper design of the initial billet shape, the interstage, and the finish form, more can be achieved as far as accuracy is concerned than by a single machine finish forming. Cold forming conditions, especially working temperature caused by heat conduction from the billet affect the spread of forming force, 12-15% at beginning with a reduction at stable stage, and further affect the component accuracy. Changes in the lubricant conditions caused variations of up to 20% in the average forming force, while the thickness of the phosphate

coating in the case of steel had no appreciable effect [68]. It is the job of process designer to design process sequences to achieve the necessary quality level without large investments. From the point of view of optimum tool utilisation, it is advisable to make the allowable tool wear and deformation as large as possible.

Dean [1] also defined major factors such as die wear and lubrication that influence the component dimensional accuracy, as mentioned as following.

Workpiece/billet: The consistency of the weight of both, billet and lubrication will directly effect dimensional accuracy, especially for closed die forging operations. Excessive material results in oversized components under given press shut-height; insufficient material may lead to underfilling defects. Thus, the accuracy of the weight of the billet has to be controlled within ± 0.5 per cent of the nominal specifications. Billets are weighed before further processing and may be graded so that heavier billets are used later in the process when tool wear results in cavity growth. Variation in lubrication treatment of the billet may lead to variation in friction coefficient which may also result in variation in component accuracy.

Tooling: Tooling design refers to the dimensions of tools which form the surfaces of die cavity. Die cavity, in turn, defines the accuracy of formed component. Elastic deflection of tools during use should be considered; thermal expansions of both, tools and workpiece, as well as the contraction of workpiece after ejection from die-cavity due to cooling, have to be taken into account in the tooling design.

Process-machine interaction must be considered especially when a multi-stage mechanical press is used. Shut-height of the different stations defines the forging stroke of the station. Thus the shut heights must adjusted for every station, independently. However, shut-heights set under zero-load condition change during forming owing to the elastic deflection of both, press and tooling. Adjustments at one station, by altering the forming load at that station, may alter the press/tool distortion and, therefore, the shut-height at other stations. This makes the adjustment a difficult iterative task. Zhang and Dean [72] developed an approach which would enable

right-first-time tool setting to be achievable. The forging-stroke of a station consists of the compression of the billet in height, the corresponding die deflection, and the forming equipment deflection at the location. Deformation/deflection consistent condition at a station results in a non-linear equation. Thus, the consideration of n stations leads to a non-linear simultaneous equation group. The solution of the equation predicts the correct shut heights at each station. Due to the nonlinearity, computer-modelling technique has to be applied to model the tool loads and press/tool deflections. It is still difficult to apply this approach widely in present, due to the difficulties in modelling of forging force simply and quickly for general forming processes. Analytical approximation of forming loads of upsetting and extrusion was applied in the modelling [72].

Workpiece-tool interaction includes the correct initial positioning of billet and the friction coefficient on the interface, which influence the final component dimensional accuracy [1]. Correct positioning of billet in die cavity is determined by the form tolerance of billet under normal feeding operation. Positioning influences material flow in die cavity and the forging load [70]. The thermal behaviour of the interface also affects component form. Different thermal contact property leads to different temperature in tool and workpiece. Thermal expansion or contraction of workpiece and tool change the dimensions of component [22].

The advantage of this component-errors-factors classification is that forming equipment, tooling, billet and the interaction between them are considered at the same time. However, the influence of forming equipment usually can be minimised by adjustment based on experience and skill. The iteration for modification of die/tool geometry is a much more time- and money-consuming task. From this point of view, the details of die-cavity factors that influence component-form error should be emphasised. Die-cavity related factors are considered as main contributing factors [22-24, 74-76].

Die-elasticity is one of the main factors influencing cold forming component-form errors. While a billet with simple geometry and given volume is forced to deform in

a die cavity, the die surfaces are expected to sustain high contact pressure owing to the flow-resistance of the work-material and friction at the billet/tool interface. The die/tool surfaces will deflect under this high contact pressure. Therefore, the final component form is not exactly a negative copy of the die cavity. A die/tool cavity deflection is, in part, replicated on the final component form. Contact pressure at tool/billet interface is a function of location. Thus, die deflection is also a function of die/tool surface location and time, and usually reaches its highest value at the moment when the tool reaches its final position [40] in closed-die forming. The influence of die-elasticity on component accuracy is not only determined by die-elasticity; factors enhancing or weakening this influence are billet accuracy, press shut-height adjustment, friction condition at the tool/billet interface and work-material properties. All factors which influence die surface contact pressure will influence die deflection, and further influence the die-elasticity related component-form error.

Secondary Yielding was presented by Rosochowski and Balendra [23]. For closed-die-forming, high forming loads are applied to achieve complete filling of the die cavity, which results in high contact pressure on die surfaces. This pressure deflects die, thus storing elastic energy. This die deflection and elastic energy increase with the increase of forming load till the forming load reaches a maximum. When the tools retract the contact pressure at tool/billet interface decreases; work-material return to elastic state and a new equilibrium is established at the billet/tool interface. Under specific conditions, it is possible for the product to be subjected to stresses corresponding to plastic state in this new equilibrium state. This process occurs over a short time-span compared to the whole forming process. However, since this deformation occurs after the termination of force applied, the dimensional accuracy of component is affected. The variation of the dimensions of the component due to Secondary Yielding depends, on an extent, on the elastic energy stored by the tools and material properties. Thus billet weight accuracy and forming stroke adjustment accuracy will effect the extent of secondary yielding. Secondary yielding would not occur in all cold forming process. Work-material properties are assumed to remain

the same during the initial plastic deformation and the subsequent secondary yielding; this has yet to be verified.

Temperature has an influence on component-form errors; this has been considered by most researchers. Local temperature due to plastic deformation may reach as high as $600^{\circ}C$ [1], and research on cold forward extrusion shows that thermal influence upon component accuracy is of the same order as that resulting from die deflection [22]. The influence of temperature upon component accuracy can be partitioned into several components. Thermal expansion of the tools is a component which results in the production of oversized products. Temperature increasing in both, products and tools, is determined by the thermal properties of work-material and tool-materials as well as by the thermal contact properties between these. Temperature elevation of product and tools is also sensitive to forming cycle time. High rate of production will increase the influence of temperature change on component accuracy.

Spring-back was often neglected because of simulation cost considerations. Plastic flow leads to work-hardening of the work-material and consequently results in high stresses in the billet. During retraction of the forming tool and ejection, the component will gradually return from a plastic to an elastic state. All elastic deflection during forming will be restored and the recovery, depending on the stress distribution before ejection, is non-uniform. Recent investigations show that the change on dimensions due to spring-back is comparable to that due to die expansion elastically [22]. This change in dimension depends mainly on the property of the work-material and the flow stress reached during forming. In fact, local elastic recovery is determined by the local flow stress and elastic constants from plasticity theory [71]. The higher the flow-stress and the lower the Young's modulus, the bigger the dimensional change due to elastic spring-back will be.

Cooling of cold-formed component after ejection from die cavity also influences component dimensions. Most of the energy expended to plastically deforming the billet is transformed into heat and is transferred to the tools; the average temperature of product after ejection is higher than that of the environment. The temperature

change in an aluminium component ranges from a few tens to hundred Celsius degrees in forward extrusion [22]. Thermal properties of the work-material and temperature variation determine the shrinkage of the product after cooling down. The thermal properties, thermal contact properties and mechanical contact properties, as well as forming cycle time would influence cooling shrinkage.

Forming equipment kinematic accuracy also influences the accuracy of the products. The die-cavity component-errors factors referred to in the preceding text are based on perfect tool motion. However, the accuracy of tool motion relates not only to the construction and assembly accuracy of tooling but also the press stiffness and kinematic accuracy [25,68]. Fig. 1.31 shows the main equipment-related contributors to the accuracy of the formed component. The most important parameters, from a product-accuracy point of view, are perpendicularity of stroke to the top surface of the bolster, parallelism between slide bottom surface and the top surface of the bolster, slide guide clearance and stiffness of the press frame. These parameters directly influence the motion of the tool and therefore, influence the accuracy of the formed product. Accurate guiding systems with high stiffness are recommended to reduce the influence of these factors on product accuracy. Component-form errors caused by inaccuracy of forming equipment may involve such form-errors that may be difficult to compensate by the re-definition of die-cavity.

1.4.6.2 Component-form errors compensation methodology

Forging equipment related component-form errors could usually be minimised by careful adjustment of tooling configuration and forging machine, such as adjustment of shut height, and main accuracy-related parameters. Die-cavity related component-form errors could only be compensated for by die-cavity compensation. Owing to this reason, most investigation upon cold formed component-form error compensation is focused on die-cavity factors [24,74-76].

Generation of form-errors during cold forging Assuming that A is a point on perfect component surface, thus is also a point on die surfaces without compensation,

as shown in Fig. 1.32a. After the tool reaches its limit position, the position of A moves to A_2 due to die deflection, including elastic-deflection and thermal expansion, and the distance $\overline{AA_2}$ shows the component-form error due to die deflection at position A. During withdrawal of the tool, the die surface contracts to release the stored elastic energy, and thus leads to the point A_2 (i.e., A_{21}) on die surface to retract to A_3. The horizontal-distance between space points A and A_3 shows the component-form error after Secondary Yielding at position A. The component-error caused by die deflection is always in opposite direction with that caused by die surface contraction during Secondary Yielding. After ejection, the component will expand due to elasticity of the work-material. Then the component cools to environmental conditions. The distance of point A_5 on the component surface corresponding to perfect component surface position A defines the overall component-errors at position A. An example of component-form error cumulation is shown in Fig. 1.32b [75]. Conceptually, the radial component-form errors in this example could be expressed as $\overline{AB}+\overline{BC}+\overline{CD}=\overline{AD}$, where $\overline{AB}$ is die-deflection, $\overline{BC}$ is caused by Secondary Yielding and $\overline{CD}$ is the result of spring-back and cooling contraction after ejection, $\overline{AD}$ is the final radial component error. It would be difficult to attain a constant radial component-form error along the component height. If Secondary Yielding occurs in the process, the resulting errors are opposite to those sustained by die deflection. In the same way, errors caused by spring-back are opposite to those caused by thermal contraction during cooling.

Errors-compensation. The first requirement for error-compensation is the analysis of deflection and expansion data as a function of die-surface location, from which the modified die-cavity surface contour can be defined. Experimental research in die-cavity compensation concerns the determination of die-cavity compensation data. Errors-compensation activities in cold forming have, in the past, been iterative [24,75]. It is essential, as the first stage, to measure the component-form after forming trials. These are compared with the specifications to determine component-form error [24]. If these errors exceed the permissible tolerances, the die surface contour or other forming parameters would be modified to enable new forming of

trials. Thus the iteration is continued till form-error is of an acceptable value. This approach is expensive, as reported in [24]; for example, the cost of iterations to achieve the nett-form of aerofoil section was of the order of hundreds of thousand pounds sterling. However, all factors that influence component accuracy can be compensated in this way.

Currently, the popular approach for the prediction of component-form with a view to compensation is FE simulation. However, a software package requires the input of accurate elastic-plastic work-material and elastic tool-material properties. Qin and Balendra [74] defined the influence of die-elasticity upon component-form errors for axisymmetric forward extrusion. The influence of the work- and tool-materials properties, frictional condition, die geometry, die-construction, as well as loading and unloading history on errors was researched. In the FE simulation model, basic monobloc die construction was used. The outside surface of die was considered to be fixed and free respectively. A shrink-fitted die has pre-deflected die surface contour, which can compensate for die elasticity more or less. Therefore, a shrink-fitted die construction is assumed to have a radial stiffness larger than that of a free outside monobloc construction, but smaller than that of monobloc construction with fixed outside surface. Thus the die deflection of a shrink-fitted die construction for forward extrusion was assumed to be between these two extreme cases and studied.

Different simulation techniques may display different computational efficiencies and accuracy. Lu and Balendra [75] presented three FE simulation models to predict die-cavity compensation data. The first was an elasto-plastic model in which the work-material was elasto-plastic and the tool-material was elastic. Thus die-deflection, Secondary Yielding and the elastic expansion of the component after ejection were simulated. The second model considers only the deformation of the billet, while the die/tool was treated as a rigid body. Thus, die-deflection in this model was ignored. This model was used by many researchers to obtain metal flow pattern and pressure contour in the die cavity during cold forming [40-42]. In the third model, both component and die/tool were treated as elastic bodies and, it was assumed that the component did not undergo plastic deformation during unloading. This linear model

could be used to simulate deflection of the die and relaxation of component individually using predefined pressure contours. Since the pressure contour after retraction of the forming tool could be chosen, the die-cavity compensation data obtained by this linear model could yield results which were a good approximation to those derived from the first model. However, the pressure contour is a prerequisite for simulation. This could be developed using rigid-plastic FE simulation or physical modelling [24]. In this investigation, the influence of temperature on compensation was neglected.

In FE simulation, mechanical contact of two bodies is activated by specifying the contact conditions between them. Whenever the contact conditions are removed, the mechanical contact/constraint between them does not exist any more. Thus, the approach of removal of contact conditions is often used to simulate retraction of tool and ejection process [77]. In order to simulate the effect of possible Secondary Yielding, correct simulation procedures should be adopted. Contact conditions between the punch and work-material should be removed before the removal of contact conditions between the die and work-material. This means withdrawal of tool should occur before ejection; Secondary Yielding just occurs between these two operations. This simulation sequence cannot be reversed; or different component-form error might be obtained. In this way, Long and Balendra [22] investigated the die-cavity compensation data for axisymmetric forward extrusion considering different work-materials, mechanical and thermal contact conditions, die deflection, temperature effect, and Secondary Yielding. The typical conceptual diagram of dimensional errors at different forming stages is shown in Fig. 1.33. "EXTRUSION" shows the radial errors of the component caused by die elasticity and thermal expansion; "UNLOADING", after secondary yielding; "EJECTION", after spring-back and "COOLING", after thermal contraction. The final result is the component-form errors. A similar description of component-errors cumulation was shown in Fig. 1.32a. The simulation of form-errors at different forming stage validated the procedure of superposition of errors by different errors-factors. The final form-errors are essential to the formulation of die-cavity compensation.

Die deflection compensation is a complex iterative process, even using FE simulation techniques. Ou and Balendra [76] investigated the die deflection compensation by FE simulation for cold forging of aerofoils. A two-dimensional plane-strain analysis of this aerofoil was conducted to analyses die deflections under different friction conditions and work-material flow patterns. Different deflections were observed when the friction coefficients, typically, are 0.03, 0.1 and 0.2 respectively. Deflection values were used to re-define the die-cavity contour by iteration. Several iterations reduced the component-form errors from 125 μm to less than 8 μm. However, it is inadvisable to use deflection values as essential data for modifying die surface since the aim of compensation is the minimisation of component-form errors rather than die-deflection. Using only die-deflection data to modify die cavity contour would result in over-compensation because the elastic expansion of the product after ejection is ignored. The overall component-form errors are the superposition of die deflection and elastic expansion of the product if influence of temperature is ignored. Fewer iterations would be required if using component-form errors as essential data to re-define die cavity contour.

A systematic investigation on elasticity-dependent error compensation methodology was developed by Balendra, Qin and Lu [24]. Form-errors and the dominant parameters were analysed and a form-comparison methodology, with the support of software and a CMM for error analysis, was presented. An illustration of the compensation procedure is shown in Fig. 1.34. The pressure contour, during forming cycle, could be measured using a 3-axis transducer; thus the measured pressure contour could be further used in FE simulation to quantitatively evaluate die deflection. Elastic- and elastic-plastic FE simulation could also be used to simulate complex component-forms, when combined with the developed form-comparison technique to determine elasticity-dependent errors. Component-errors formed the basis for defining the die-form compensation requirements. The geometry of the compensated dies was then translated to CAM software that enabled the NC programming to machine new compensated dies. Automatic preparation of FE simulation model-files enabled quick repeated FE validation simulations. Several loops are shown in Fig. 1.34, for example, $\overline{DEFHGD}$ being one of these, which is a

compensation procedure in which errors are determined by component-form measurement. $\overline{CEFC}$ is the compensation procedure used currently in which the die-cavity compensation is determined by iterations of FE simulations. Different compensation procedure could be obtained using combination of these procedures. Temperature changes were not considered in this research.

Die/billet interface parameters, such as friction coefficient/factor and thermal contact conductance, influence the cold forged product accuracy. It has been shown that research in thermal contact behaviour during cold forming is at its infancy. The review of investigations on die/billet interface parameters research will be conducted into details in related chapters.

Component-error compensation is the basic support technology to achieve the nett-form of a product. Although FE simulation has become the major tool to simulate forming procedure, the reliability of results depends on the accuracy of the input data. Iterations, in particular the iterations for modification of die surface geometry, are necessary because of the inaccuracy of input data. Thus effective error compensation depends on the knowledge of the methodology of error compensation and material property and friction data.

1.4.7 Considerations and problems

The die-elasticity and temperature influence the form of the component. However, the extent of the influence is determined by a variety of factors, such as die/tool geometry and construction, friction coefficient, thermal contact conductance, tool- and work-material properties. Nett-form cold-formed components can be achieved using suitable errors-compensation approach, including re-definition of die surface geometry and change physical forming conditions. Modification of the physical conditions, especially friction condition is difficult [24]; some of the fundamental relationships between forming parameters and form-errors have been recognised; both experimental modelling and FE simulation have been admitted as effective approaches to model component-form. However, the influence of interfacial

parameters has not been thoroughly investigated. Data that governs heat transfer between die/tool and billet at high contact pressures is scarce.

Although precision cold forming has already had a quite long history of development, a comprehensively and systematic modelling of the process has not developed yet. A thorough modelling of the processing is important to both, the forming research and industrial practice.

Based on the literature review and considerations on cold forming, insufficiency of previous research is summarised as follows:

1. Compensation for overall component-form errors has not been paid much attention; current error-compensation methodology was established based on die elasticity.
2. Directly modifying die-surface form is often difficult and expensive due to manufacturing die-cavity surfaces at accuracy of microns level.
3. Thermal contact conductance at billet/tool interface has not been researched sufficiently for cold forming.
4. The relation between thermal contact behaviour and contact conditions (surface texture, contact pressure, and temperature) remains unknown; in particular, experimental supporting data at high contact pressure is scarce.
5. Precision cold forming, as an advanced manufacturing method, has not been systematically modelled; most investigation emphasises one of aspects of the forming process. A systematic modelling of precision cold forming decision-making procedure is required.

1.5 Aims of the research

Based on above discussion, aims of the research are defined as follows:

1. Modelling precision cold forming process systematically by IDEF0 language, leading to a decision-tree for the design and analysis of precision cold forming. This provides the base for the rest of this research.
2. Experimentally investigating the thermal contact conductance as a function of interfacial pressure and surface texture.

3. Establishing a surface geometric model that enables FE simulation of surface contact and prediction of surface deformation, the real contact area and the thermal contact behaviour.
4. Optimising precision cold forming die by using profiled shrink-fitting interference, aimed at die elasticity or overall component form-error compensation and providing necessary pre-stress of die surface.

1.6 Research approaches

Different research approaches were used in this work. IDEF modelling language was used to systematically model precision cold forming as a system. Experimental investigation was used to study thermal contact conductance as a function of contact conditions, such as interfacial pressure and surface texture. Analytical and mathematical methods were used to establish necessary models. A surface model was established by surface geometric analysis; die optimisation model for most accurate component was established by least-squares approach. EF simulations, including thermo-mechanical coupled elastic-plastic FE simulation, were extensively used in many cases, especially used for FE simulation of thermal contact conductance and die optimisation. In this work, ABAQUS package, used as a tool to calculate objective function, was built in an optimisation program, written by the author.

1.7 Organisation of the thesis

The thesis is divided into six chapters. The first Chapter introduces the general literature review of precision cold forming development and the aims of this research. The second Chapter presents the systematic modelling of the precision cold forming process by IDFE language, resulting in a decision-making tree. Cold forming design procedure was divided into a series basic activities in sequences. IDEF software was used in modelling each activity. All necessary input data, resources, constraints and results of each activity were defined and modelled, especially those iteration paths which character the precision cold forming process. Chapter three reports the experimental investigation of thermal contact conductance, including experimental equipment, experimental principles, specimen preparation,

data processing and errors analysis. A novel FE simulation model of surface deformation for surface mechanical contact was established in the Chapter four, providing a theoretical preparation for the heat transfer simulation of thermal contact. Surface textures after different interfacial pressures under different initial textures were successfully predicted by the technique presented in this Chapter; the FE simulation results were compared with the data of surface measurements after contact under different interfacial pressures. Based on this, thermal contact conductance was simulated by FEM in the Chapter five using two thermal models: thermal contact conductance as a function of the local interfacial pressure and as a function of the ratio of real contact area to nominal contact area. Simulation results were compared with the data of experiments in agreement. In Chapter six, an approach using shrink-fitted die with a profiled interference to compensate for die deflection or overall component form-error by FE simulations was presented. Die deflection under forming interfacial pressure is opposite to that under shrink-fitting interference. Thus linear superposition principle could be applied with a view to negating the die deflection under forming pressure by specifying a profiled shrink-fitting interference. Based on the research of the previous chapters, an optimisation model for axisymmetric cold-formed component has been also established in this Chapter. Sum of squares of nodal errors on component surface is chosen as the objective with nodal shrink-fitting interference on the interface as design variables. Die manufacture and assembly conditions were considered as constraints. The influence of material properties, thermal properties, frictional coefficient and forming stroke on component accuracy were analysed and discussed.

1.8 References

1. T. A. Dean, Precision forging, Proceeds of the Institution of Mechanical Engineers Part C-Journal of Engineering Science, 214: (1) 113-126 2000
2. K. Lange, Cold forging today and tomorrow, 7th International Congress Cold-Forging, University of Birmingham, April 24-26, 1985
3. N. Bay, Cold Forming of Aluminium-State of the Art, Journal of Materials Processing Technology, Vol. 71, pp. 76-90, 1997

4. O. Jensrud, K. Pedersen, Cold Forging of High Strength Aluminium Alloys and the Development of New Thermomechanical Processing, Journal of Materials Processing Technology, 80-1: 156-160 AUG-SEP 1998
5. A. Pale, R. Shivpuri and T. Altan, Recent Developments in Tooling, Machines and Research in Cold Forming of Complex Parts, Journal of Materials Processing Technology, Vol. 33, pp. 1-29, 1992
6. T. Steenberg, J. S. Olsen, Christensen E, N. J. Bjerrum, Estimation of Temperature in the Lubricant Film during Cold Forging of Stainless Steel Based on Studies of Phase Transformations in the Film, WEAR 232: (2) 140-144 OCT 1999
7. David C Goss, High Strength Cold Forged Out of Work Hardening Steel, Journal of Materials Processing Technology, 98: (1) 135—142, 2000
8. R. Matsuoka, Effects of Cold-Rolling on the Cold Forging of Solid Polymer, Journal of Materials Processing Technology, 84: (1-3) 175-180 DEC 1 1998
9. R. Shivpuri, et al, Recent Advances in Cold and Warm Forging Process Modelling Techniques: Selected Examples, Journal of Materials Processing Technology, Vol. 46, pp. 253-274, 1994
10. H. Yoshimura, K. Tanaka, Precision Forging of Aluminium and Steel, Journal of Materials Processing Technology, 98: (1) 196—204, 2000
11. S. Onodera and K. Sawai, Modern Cold Forging Applications for the Manufacture of Complex Automotive Parts, Journal of Materials Processing Technology, Vol. 46, pp. 169-183, 1994
12. J. C. Choi, Y. Choi, Precision Forging of Spur Gears with Inside Relief, International Journal of Machine Tools & Manufacture, 39: (10) 1575-1588 OCT 1999
13. H. Nagele, H. Worner and M. Hirschvogel, Automotive Parts Produced by Optimising the Process Flow Forming-Machining, Journal of Materials Processing Technology, 98: (1) 171—175, 2000
14. M. Meidert and M. Hansel, Net Shape Cold Forging to Close Tolerances under QS 9000 Aspects, Journal of Materials Processing Technology, 98: (1) 150—154, 2000

15. A. G. Mamlis, D. E. Manolakos and A. K. Baldoukas, Simulation of the Precision Forging of Bevel Gears Using Implicit and Explicit FE Techniques, Journal of Materials Processing Technology, Vol. 57, No. 1-2, pp. 164-171, 1996
16. S. Roy, S. Ghosh and R. Shivpuri, A New Approach to Optimal Design of Multi-Stage Metal Forming Processes with Micro Genetic Algorithms, International Journal of Machine Tools & Manufacture, Vol. 37, No. 1, pp. 29-44, 1997
17. V. Vazquez, et al, Tooling and Process Design to Cold Forge A Cross Groove Inner Race for A Constant Velocity Joint - Physical Modelling and FEM Process Simulation, Journal of Materials Processing Technology Vol.59: No.1-2, pp. 144-157, 1996
18. H. He, et al, Microstructure and Mechanical Properties of An Al/SiCp Composite Cold Die Forged Gear, Materials and Design Vol. 17, No. 2, pp. 97-102, 1996
19. R. Shivpuri, et al, Recent Advances in Cold and Warm Forging Process Modelling Techniques: Selected Examples, Journal of Materials Processing Technology, Vol. 46, pp. 253-274, 1994
20. N. Bay, The State of the Art in Cold Forging Lubrication, Journal of Materials Processing Technology, Vol. 46, pp. 19-40, 1994
21. J. Dong, J. He and J. Gu, The Effect of Organic Borate in Cold Forging and Extrusion, Journal of the Society of Tribologists and Lubrication Engineers, Vol. 51, No. 6, pp. 519-524, 1995
22. H. Long, R. Balendra, FE Simulation of the Influence of the Thermal and Elastic Effects on the Accuracy of Cold-Extruded Components, Journal of Materials Processing Technology, Vol. 84, pp. 247-260, 1998
23. A. Rosochowski and R. Balendra, Effect of Secondary Yielding on Nett-Shape Forming, Journal of Materials Processing Technology, 1996, Vol. 58, No. 2-3, pp. 145-152.
24. R. Balendra, Y. Qin, X. Lu, Analysis, Evaluation and Compensation of Component-Errors in the Nett-Forming of Engineering Components, Journal of Materials Processing Technology 106: (1-3) 204-211 OCT 31 2000
25. N. Ishinaga, An Advanced Press Design for Cold Forging, Journal of Materials Processing Technology 71: (1) 100-104, 1997

26. S. Onodera and K. Sawai, Modern Cold Forging Applications for the Manufacture of Complex Automotive Parts, Journal of Materials Processing Technology, Vol. 46, pp. 169-183, 1994
27. K. Osakada, X. Wang and S. Hanami, Precision Forging Process with Axially Driven Container, Journal of Materials Processing Technology, Vol. 71, pp. 105-112, 1997
28. T. Nakano, Modern Applications of Complex Forming and Multi-Action Forming in Cold Forging , Journal of Materials Processing Technology, Vol. 46, pp. 201-226, 1994
29. Y. B. Park, D. Y. Yang, Finite Element analysis for precision Cold Forging of helical gear using recurrent boundary conditions, Proceeds of the institution of mechanical engineers Part B-journal of engineering manufacture, 212: (3) 231-240 1998
30. J. H. Lee, B. S. Kang, J. H. Lee, Process design in multi-stage Cold Forging by the Finite-Element Method, Journal of Materials Processing Technology, Vol. 58, No. 2-3, pp. 174-183, 1996
31. K. Kuzman, et al, Control Material Flow in a Combined Backward Can-Forward Rod Extrusion, Journal of Materials Processing Technology, Vol. 60, No. 1-4, pp. 141-147, 1996
32. M. Kaiso, et al., Cold Forgeability in Medium Carbon Steel with Insufficiently Spheroidized Microstructure, Journal of the Iron and Steel Institution of Japan, 1998, Vol. 84, No. 10, pp. 721~726
33. K. Siegert, et al, Recent Development on High Precision Forging of Aluminium and Steel, Journal of Materials Processing Technology Vol. 71, PP. 91-99, 1997
34. G. Sutradhar, A. K. Jha and S. Kumar, Cold Forging of Sintered Iron-Powder Preform, Journal of Materials Processing Technology, Vol. 51, pp. 369-386, 1995
35. L. Janicek and B. Maros, The Determination of the Cold Forgeability for Specimens with Axial Notches of Heat Resisting and Corrosion Resisting Chromium Nickel Steels, Journal of Materials Processing Technology Vol. 60, pp. 269-274, 1996

36. S. Matsuoka, Effects of Cold-Rolling on the Cold Forging of Solid Polymer, Journal of Materials Processing Technology Vol. 84, pp. 175-180, 1998
37. A. Verleene, M. Dubar, L. Dubar, A. Dubois and J. Oudin, Determination of A Hardening Behaviour Law for a Cold Forging TiN-Coated Tool Steel , Surface & coatings Technology 127: (1) 52-58 MAY 1 2000
38. H. Berns, et al, A New Material for Cold Forging Tools, Computational Materials Science, 11: (3) 166-180 MAY 1998
39. F. Seidel, H. R. Stock, and P. Mayr, Development of Ion-Implanted Hard Coatings for Industrial Applications in Low Lubricated Cold Forging , Surface & Coatings Technology, No. 84, No. 1-3, pp. 506-511, 1996
40. V. Vazquez, D. Hannan, T. Altan, Tool Life in Cold Forging - An Example of Design Improvement to Increase Service Life, Journal of Materials Processing Technology, 98: (1) 90-96 JAN 15 2000
41. M. Knoerr, K. Lange and T. Altan, Fatigue Failure of Cold Forging Tooling: Causes and Possible Solutions Through Fatigue Analysis, Journal of Materials Processing Technology, Vol. 46, pp. 57-71, 1994
42. Y. Nagao, M. Knoerr and T. Altan, Improvement of Tool Life in Cold Forging of Complex Automotive Parts, Journal of Materials Processing Technology, Vol. 46, pp. 73-85, 1994
43. P. Brondsted, P. Skov-Hansen, Fatigue Properties of High-Strength Materials Used in Cold-Forging Tools, International Journal of Fatigue, 20: (5) 373-381 May 1998
44. P. Skov-Hansen, et al, Fatigue in Cold-Forging Dies: Tool Life Analysis, Journal of Materials Processing Technology, 95: (1-3) 40-48 OCT 15 1999
45. Pedersen TO, Numerical Modelling of Cyclic Plasticity and Fatigue Damage in Cold-Forging Tools, International Journal of Mechanical Science, 42: (4) 799-818 Apr. 2000
46. B. Falk, U. Engel and M. Geiger, Estimation of Tool Life in Bulk Metal Forming Based on Different Failure Concepts, Journal of Materials Processing Technology, 80-1: 602-607 Aug.-Sep. 1998
47. Pedersen TO, Numerical Studies of Low Cycle Fatigue in Forward Extrusion Dies, Journal of Materials Processing Technology 105: (3) 359-370 SEP 29 2000

48. S. H. Ahn, et al, A Study on the Prediction of Fatigue Life in An Axi-Symmetric Extrusion Die, Journal of Materials Processing Technology, Vol. 71, pp. 343-349, 1997
49. J. Groenbaek and E. B. Nielsen, New Developments in the Design of High Performance, Strip-Wound Cold Forging Tools, Journal of Materials Processing Technology, Vol. 46, pp. 87-97, 1994
50. N. Bay, The State of the Art in Cold Forging Lubrication, Journal of Materials Processing Technology, Vol. 46, pp. 19-40, 1994
51. T. Ohmori, K. kitamura and M. Kawamura, Evaluation of Galling Prevention Properties of Cold Forging Oils by Ball Penetration Test, Wear, Vol. 155, pp. 183-192, 1992
52. T. Steenberg, J. S. Olsen, E. Christensen, N. J. Bjerrum, Estimation of Temperature in the Lubricant Film during Cold Forging of Stainless Steel Based on Studies of Phase Transformations in the Film, Wear 232: (2) 140-144 OCT 1999
53. L. Dubar, J. P. Bricout, C. Wierre and P. Meignan, New Surface Processes for Cold Forging of Steels, Surface & Coatings Technology, 102: (1-2) 159-167 Apr. 1 1998
54. Y. G. Meng and S. Z. Wen, A Finite Element Approach to Plasto-Hydrodynamic Lubrication in Cold Forging , Wear, Vol. 160, pp. 163-170, 1993
55. T. Nishimura, et al, A Method for the Evaluation of Lubrication Using Injection Upsetting, Journal of Material Processing Technology, Vol. 53, pp. 712-725, 1995
56. T. Nishimura, T. Sato and Y. Tada, Evaluation of Frictional Conditions for Various Tool Materials and Lubricants Using the Injection-Upsetting Method, Journal of Material Processing Technology, Vol. 53, pp. 726-735, 1995
57. H. Kim, T. Yagi and M. Yamanaka, FE Simulation as a Must Tool in Cold/Warm Forging Process and Tool Design, Journal of Materials Processing Technology, 98: (1) 143—149, 2000
58. T. Altan and V. Vazquez, Status of Process Simulation Using 2D and 3D Finite Element Method 'What Is Practical Today? What Can We Expect in the Future?', Journal of Materials Processing Technology, Vol. 71, pp. 49-63, 1997

59. S. Tjotta and O. Heimlund, Finite-Element Simulation in Cold-Forging Process Design, Journal of Materials Processing Technology, Vol. 36, pp. 79-96, 1992
60. J. Walters, et al, Recent Development of Process Simulation for Industrial Applications, Journal of Materials Processing Technology, 98: (1) 205—211, 2000
61. T. Welo, et al, Cold Forging and Grain-Size Control in An Al-1.2wt-Percent-Si Alloy, Journal of Materials Processing Technology, 1992, Vol. 34, No. 1-4, pp. 533-539
62. J. Kusiak, A Technique of Tool-Shape Optimisation in Large Scale Problems of Metal Forming, Journal of Materials Processing Technology, Vol. 57, pp. 79-84, 1996
63. H. S. Kim, et al, Prediction of Ductile Fracture in Cold Forging of Aluminium Alloy, Journal of Manufacturing Science and Engineering-Transactions of the ASME, Vol. 121, No. 3, pp. 336-344, 1999
64. E. Taupin, Material Fracture and Burr Formation in Blanking Results of FEM Simulation s and Comparison with Experiments, Journal of Materials Processing Technology, Vol.59, pp. 68-78, 1996
65. M. S. Joun and S. M. Hwang, Optimal Process Design in Steady-State Metal Forming by Finite Element Method-I. Theoretical Considerations, International Journal of Machine Tools & Manufacture, Vol. 33, No. 1, pp. 63-70,1993
66. R. Duggirala et al, Computer Aided Approach for Design and Optimisation of Cold Forging Sequences for Automotive Parts, Journal of Materials Processing Technology, Vol. 46, pp. 185-198, 1994
67. K. Kalmanje, Micro-Genetic Algorithm for Stationary and Non-Stationary Function Optimisation, Intelligent Control and Adaptive Systems, SPIE, Vol. 1196, pp. 289-297, 1989
68. K. Lange, Handbook of metal forming, pp. 15.1-15.99, McGraw-Hill, Inc. 1985
69. P. W. Li and G. D. Hong, On the Stiffness of Screw Presses, International Journal of Machine Tools & Manufacture, Vol. 37, No. 1, pp. 93-100, 1997
70. A. O. A. Ibhadode and T. A. Dean, The Effect of Billet Location on Completely Closed Cavity Die Forging , Proc. Instn. Mech. Engrs, Part B, Journal of Engineering Manufacture, Vol. 202, No. B4, pp. 227-235, 1988

71. R. Hill, The Mathematical Theory of Plasticity, Oxford: Clerandon Press, 1983
72. H. G. Zhang and T. A. Dean, Computer Modelling of Tool Loads and Press/Tool Deflections in Multistatge Forging , International Journal of Machine Tools & Manufacture, Vol. 35, No. 1,pp. 61-69, 1995
73. E. Doege, J. Thalemann and F. Weber, Conditions for A Structured Layout of Precision Forging , Journal of Materials Processing Technology, Vol. 46, pp. 41-53, 1994
74. Y. Qin and R. Balendra, FE Simulation of the Influence of Die-Elasticity on Component Dimensions in Forward Extrusion, International Journal of Machine Tools & Manufacture, Vol. 37, No. 2, pp. 183-192,1997
75. X. Lu and R. Balendra, Evaluation of FE Models for the Calculation of Die-Cavity Compensation, Journal of Materials Processing Technology, Vol.58, pp. 212-216, 1996
76. H. Ou, R. Balendra, Die-Elasticity for Precision Forging of Aerofoil Sections Using Finite Element Simulation , Journal of Materials Processing Technology, 76: (1-3) 56-61 APR 1998
77. Hibbitt, Karlsson & Sorensen Inc., ABAQUS User Manual, 1997.

Chapter Two

Modelling of the Precision Cold Forming Design Procedure

2.1 Summary

Systematically understanding precision cold forming process design is important to both process designer and investigator alike. Modelling precision cold forming process by means of IDEF0 methodology may be a simple, concise and accurate approach systematically to understand the process as a whole.

Design and manufacture for precision cold forming is decomposed into six basic activities: (1) forming sequence selection/design, (2) tool design, (3) FE simulation, (4) form-comparison, (5) tool manufacturing, and (6) component manufacturing. Emphasis is stressed at tool design activity; very detailed decompositions of this activity were conducted. Therefore, the notable iterative characteristics of precision cold forming tool design procedure were successfully modelled.

Compensation for component form-error is the key task of die surface design for a precision cold forming process. Two paths of iteration for component form-error compensation were modelled, *small* and *big iterations*. FE simulation to predict computational component-form and enable form-error compensation, without involving manufacture of tool and component, is defined as small iteration; if manufacturing activities are involved, the design iteration procedure is referred to as big iteration. Both iterations were modelled into fine details, and their applications and combination were discussed. These iterative procedures can be regarded as the design of last operation in a multi-staged process. Therefore, multi-staged cold forging process can be modelled in the same way in this study.

IDEF0 modelling precision cold forming provides an overall picture of the process. The significance of component-error compensation, in particular by shrink-fitting approach, the importance of interface parameters, such as friction and thermal contact, are presented.

2.2 Glossaries

Computational component form	Geometry and dimensions of the component predicted by FE simulation
Manufactured component form	Component form obtained by measuring the manufactured component
Computational form comparison	Comparison between the specified component form and the computational component form
Manufactured form comparison	Comparison between the specified component form and the manufactured component form
Die surface form comparison	Comparison between specified die surface form and manufactured die surface form

2.3 Introduction

2.3.1 IDEF methodology

IDEF methodologies have been developed in projects sponsored by the US Air Force in order to describe, specify and model manufacturing systems in a structured graphical form [1-2]. It was developed from the structured analysis and design concept in 1970s [3] and has been widely applied in intelligent system simulation [4], manufacturing systems analysis and design [5-6], manufacturing system scheduling optimisation [3], risk assessment [7], modelling and design of flexible manufacturing systems [8], development of nett shape process environment [9], manufacturing process management [10] and business process simulation [11]. When combined with other methodologies, it is possible to develop on-line manufacturing control systems [12]. The term IDEF is the abbreviation for ICAM (Integrated computer Aided Manufacturing) DEFinition. It is a graphic language to model and describe a system in a "structured-analysis" approach [1].

This methodology enables the rapid development of the corresponding software tools. The basic members of the IDEF family are IDEF0, IDEF1, IDEF2 and IDEF3, with different modelling functions, although many IDEF methods (IDEF0-IDEF14) are available or being developed nowadays [13], while the most often used one, perhaps, is IDEF0 [14]. IDEF methods can be classified into two major categories. The first includes those methods used to describe existing or proposed systems. The second category includes those methods used to design proposed systems. IDEF0, a function modelling method [2], is used to decompose functions of a system into their component activities, or to identify activities in a system through capturing the information such as inputs, constraints, outputs, and mechanisms; it is therefore classified as the first category. Activities are represented by boxes. In the context of IDEF0, a system is defined statically and hierarchically through activities and the relationship between the activities using a graphic language, and the corresponding model of a system is often referred to as the " as-is" model, which means "what the system does" [9,14].

IDEF1 methodology can be applied to abstract, classify, and define the information objects of a system, referred to as information requirements modelling [1,10,13]. There are three components of the information model: entity, attribute, and relationship. These components provide a rigorous yet simple portrayal of the information structure of a system. IDEF1 model, which describes the information structure of a system, is referred to as the information-based "to-be" model, – "how the system does" [9,14].

To enable the analysis of performance, dynamic information, such as time and time-related parameters, are incorporated into IDEF0 model in the form of text files, attached to relevant boxes or arrows. Thus in an IDEF0-based IDEF2 model, the dynamic modelling of a system can be conducted by corresponding software. Both IDFE0 and IDEF2 model collectively define "how things are to be done". At implementation description level, the IDEF0-based IDEF2 dynamic model is further extended to include details such as exception handling rules, activation rules, and

data communications addresses, to enable execution of the model for workflow control [2].

Development of IDEF3 is with a view to identifying the need to distinguish between the description of what a system is supposed to do and the "model" which is used to predict what a system will do [1]. Instead of creating a model of the system, IDEF3 captures precedence and causality relations between situation and events in a form that is natural to domain experts; instead of building predictive mathematical model, IDEF3 builds structured description with two types of diagram: process flow diagrams which capture the knowledge of how things work and object-state, and transition network diagrams which summarise the allowable transition of an object [1]. Thus, an IDEF3 model is also a collection of diagrams, texts, and glossaries with boxes and arrows that present activities and interfaces [7]. The relationship between activities is modeled with three types of links: precedence, object flow and relational. The precedence and object flow links express the simple temporal precedence between activities. The relational links highlight the existence of relationships among activities. The logic of branching within a process is modeled using *AND* (&), *OR* (*O*) and exclusive *OR* (*X*) junction boxes [7].

Table 2.1 Summary of IDEF methodology [1]

Method	Function	Descriptive	Modelling
IDEF0	Function modelling		*
IDEF1	Information requirements modelling		*
IDEF1X	Database design		*
IDEF2	Dynamic simulation modelling		*
IDEF3	Process description capture	*	
IDEF4	Object oriented design		*
IDEF5	Concept/ontology description	*	
IDEF6	Design rationale capture		*

Table 2.1 is the summary of the IDEF methodology [1]. The majority of these are models except for IDEF3 and IDFE5, which are descriptive. It is worth pointing out that IDEF0 is the most basic foundation of the IDEF family. Most of other models can be derived from deliberately designed IDEF0 models from prescribed design rules and communication agreements and corresponding software tools. Therefore, IDEF0 is one of the most important approaches in the IDEF-methodology family.

2.3.2 Introduction of IDFE0 methodology

IDEF0 methodology will be used to model precision cold forming design procedure. Therefore, a more detailed IDEF0 methodology is introduced in the following text.

IDEF0 is referred to as a graphic language for modelling manufacturing processes in a concise and rigorous way [14]. Both, manufacturing and development processes can be partitioned into a series of activities or operations, each of which has predictable results. The relationship between activities, operations, or interfaces, is expressed by arrows with text label. Generally, there are four descriptions for every activity at any description level; these are input, output, mechanisms/resources and controls/constraints, as shown in Fig. 2.1. Each of them is defined in the following text:

- Activity is a named process, function or task that occurs over time and has recognisable results. The activity-name is placed inside the box.
- Input is the information/material, or data needed to initialise the activity; the input position is to the left of the activity box.
- Controls/constraints are the conditions that constrain the defined activity. Controls/constraints are above the activity box.
- Mechanisms/resources refer to people, machines, or existing systems that perform the defined activity; these are located below the activity box.
- Output is the result derived from the activity; this is positioned to the right of the activity box.

The box and inputs/outputs were originally defined for the purpose of describing of manufacturing activities. Therefore, inputs were usually manufactured materials; mechanisms/resources show the machine and operators required by the activity; control/constraints shows the condition of the machine; and finally the output shows the product of the activity. Although IDEF0 is not used exclusively for the modelling of manufacturing process, the inputs/outputs labels retain the originally definition. For example, upsetting can be defined as an activity in which billet is an input; press, operator and die/tools are mechanisms/resources; the parameters of the press (capacity, stiffness, precision and control functions) are controls/constraints and the

product is the output. The wide application of IDEF0 nowadays has extended the definitions of inputs, outputs, mechanisms and controls. For example, if meshing is defined as an activity, geometric specifications of simulated object will be input, the corresponding software, computer, analyst are mechanisms/resources, memory size, CPU speed, capacity of disk are controls/constraints and the final mesh data is the output.

An advantageous aspect of IDEF0 modelling is its hierarchical structure, which can be used to model complex systems. For example, Fig. 2.2 shows an activity referred to as $A0$ which requires input $I1$ and $I2$, controls $C1$, $C2$ and $C3$, mechanisms $M1$, $M2$ and $M3$ to produce outputs $O1$, $O2$ and $O3$. A more detailed level of the process can be modeled further. Activity $A0$ can be further decomposed into, for example, three sub-activities $A1$, $A2$ and $A3$ respectively, as shown in Fig. 2.3. Generally, the higher level activities represent more general and abstract concepts, which can be decomposed into levels of activities representing more specific and detailed concepts [9].

2.3.3 Applications of IDEF0 in metal forming

Lee, et al [15] reported the application of IDEF0 for modelling die-design procedure for a cold forging process. The top level is shown in Fig. 2.4. There are three groups of required input data, seven necessary resources and three constraints, resulting in five outputs. Decomposition of the system is shown in Fig. 2.5, resulted in three sub-activities shown as $A1$, $A2$ and $A3$. Sub-activity $A2$ was further decomposed into the third layer by sub-activities A21 and A22, shown in Fig. 2.6. Finally, activity A22 was decomposed into activities A221, A222, A223 and A224 shown in Fig. 2.7. By IDEF0 methodology, all activities involved in a system can be modeled into the required details. All activities, according to their decomposing relationship, referred to as parents-child relationship in IDEF methodology [2,9], can be illustrated as in Fig. 2.8, which was referred to as a decision-tree. The decision-tree can grow new branches if new decisions are to be made; some of its branches can also be pruned if some decisions are considered redundant. A similar fault-tree was constructed by Kusiak [7] using IDEF methodology, to enable a risk assessment of process models.

Chen [9] investigated the IDEF0 modelling of nett-shape casting process, as shown in Fig. 2.9. The activities of nett-shape product and process development were divided into conceptual design, preliminary design, process selection, design for nett-shape processes, process design, die or mould design, and die or mould manufacturing process planning. In conceptual design stage, a sketch or a conceptual product model is configured based on the product requirements. The task of preliminary design involves the construction of the preliminary product geometry. The preliminary product geometry contains components that meet the product functional requirements and the interrelationships.

At the process selection stage, the decision to use a particular process is constrained by preliminary product geometry, lot sizes, equipment availability, component tolerances, material requirements and desired mechanical properties of the final product.

After a manufacturing process is selected, the design for nett-shape process is performed to refine the preliminary product geometry into one that is functionally acceptable and compatible with the selected manufacturing process. It involves a wide variety of design expertise, knowledge of engineering and the selected process. Generally, if manufacturability was excluded, factors which affect life and cost of tools and optimisation of manufacturing process are also considered relative to quality, cost and throughout time.

Manufacturability and cost of tools are the major considerations in tools design. These factors are influenced by the shape of the product and the process design. Tool design involves procedures similar to those for the product design.

At the process design stage, decisions are made to reduce manufacturing cycle time and to determine the overall manufacturing maintenance associated with a specific component. The decision depends substantially on the geometric characteristics of the component and the results of tool design. However, this relationship is not clear defined in the IDEF0 model shown by Fig. 2.9.

Process planning for tool fabrication can be defined as the systematic development of the methods by which tools can be manufactured economically and competitively. In general, the inputs to process planning are data on technical requirements, raw material, facilities and quality specifications. Both technical and quality data are defined and specified at tool design stage based on the specifications and requirements of the component/product.

In general, nett-shape process design, casting or forging, is an iterative process for the purpose of achieving high precision product. However, this iterative design process is not modelled; neither iterative path is shown in Fig. 2.9.

2.4 Significance of IDEF0 modelling

IDEF0 modelling of precision cold forming process can assist the product designer, process analyst, dies/tools design engineer and dies/tools manufacturer, to acquire a complete understanding of the entire design procedure in a systematic manner. Precision cold forming is one of the technologies to manufacture nett- or near-nett shape product. From the manufacturing system point of view, a manufacturing system involving precision cold forming as main manufacturing process is complex due to the required precision level. Using the IDEF0 structural analysis methodology, the conventional nett-shape product and process development procedure is presented as an "as-is" development model, with a structured and hierarchical diagrammatic representation of requirements and controls [9]. The diagram enables all designers and analysts with different responsibilities to appreciate the activities/operations required, the characteristics of nett-shape product and processes involved, their constraints, supporting resources needed, as well as information flow in the process. Hsu and Lee [16] proposed an intelligent cold forging system, the structure of which is shown in Fig. 2.10. The whole system was divided into five levels. The first is the tasks/activities level of the system, which was modeled efficiently and effectively by IDEF0 modelling [15]. At the same time, IDEF0 modelling provides the links to connect individuals to the whole program.

IDEF0 modelling of a precision cold forming process is a general and overall recognition to the entire precision cold forming system, which defines the involved

activities and the relationship among them. Activities, such as determination of interfacial parameters (thermal contact conductance and friction) and component precision compensation are only a few very necessary activities involved in the precision cold forming. Therefore, IDEF0 modelling precision cold forming process is the foundation for any individual activity research; IDEF0 model shows the position and function of every activity and every design parameter in the system. In this research, IDEF0 methodology will be used to model the precision cold forming process design to a sufficiently detailed level to guide a few specific activities involved in the entire process, such as modelling of thermal contact conductance and component-error compensation, which consist of the basic schema of this research.

2.5 IDEF0 modelling of precision cold forming process design and activities analysis

Precision cold forming process design is only part of a cold forging manufacturing system. This research is limited only to IDEF0 modelling of precision cold forging process design.

2.5.1 Level zero

The preliminary inputs for precision forging are component/product requirements and specifications that refer to form accuracy, surface finish, mechanical properties, material and batch size. The main outputs are divided into three parts: processing, tooling and component/product related respectively. The processing related outputs are forming sequences and the forming equipment. Tooling includes CAD definition of dies/tools geometry, tool-materials, surface finish requirements, lubrication, billet specifications, and punches movement profiles. Component/product related outputs are product, the form-error and tolerance. To achieve this, several supporting resources/mechanisms are required; each of which is subjected to constraints or controls, referred to in Fig. 2.11, for the precision cold forming process design. The activity A0 can be divided into many sub-activities; each sub-activity will rely on different supporting resources specified at this level.

2.5.2 Level one

2.5.2.1 Forming sequences selection/design

The level zero IDEF0 diagram remains abstract; therefore, it is decomposed into six sub-activities: forming sequences selection/design, tools design, FE simulation, form comparison, tools manufacturing and product manufacturing, as shown in Fig. 2.12. Forming sequence selection/design activity determines the required forming sequences, the corresponding forming equipment, the billet and middle workpiece geometric CAD definitions and the required punches movement profiles during different forming sequences. These outputs depend on the required product geometry, the product accuracy and the batch manufacturing size. Currently, this is based on experience. Thus cold forming design experience and skills are important input resources. Besides, the precision cold forming sequence is an iterative process if FE simulation is incorporated into the process, in particular when optimisation of forming sequence is required [17]. Thus, the FE simulation results, based on the design result of last design cycle and the tools design results, are fed back as parts of the inputs of the forming sequences selection, as shown in Fig. 2.12. Die-filling, fracture initiation, folding, forging force signature, dies/tools stresses from FE simulations and component form-error by form-comparison activity are also fed back as inputs into the forming sequences selection/design activity. Iterative design procedures, which are the most notable characteristics of precision cold forming, is rigorously modeled in IDEF0 methodology. These iterative characteristics of precision cold forming had not been previously modelled [9, 15-16].

2.5.2.2 Tools design

After determination of the forming sequence, the outputs of the forming sequence selection/design become some of the inputs for the tool design activity. Tool design is the most important iterative procedure of precision cold forming process design. The required component information (component geometry, surface finish requirements, properties requirements, batch size, work material), FE simulation information (die filling, fracture initiation, folding, tool stresses) from previous design cycle and component form-error from form-comparison of the last design cycle, are fed back as inputs to the tool design activity, as shown in Fig. 2.12. The

output of tool design activity is a description of the tool geometry, specifications of tool materials, tool surfaces requirements, heat treatment and lubrication which will become inputs to the tool manufacturing activity.

The specifications of tools should include the compensation for component form-error arising from elasticity and thermal considerations. The procedure for the activity at this specification is further decomposed into a more specific level, as shown in Fig. 2.13. The tool design activity is decomposed into four sub-activities: die surface geometry design, die structure design, punch and ejector design and functional component design. The functional component design activity refers to the design of structural components of the tools, which retain the tools on the press; supporting rings, punch and die locks, stress rings, pressure pads and connectors are some of the items referred to [16].

Die structure design is defined as the design of die inserts or the components that consist of die surfaces and contact directly with work material. This design is closely related to the interrelationship between billet and tooling configuration. Lange [18], using a systematic approach to metal forming processes, classified the general metal forming configuration as six main different functional areas, as shown in Fig. 2.14. Area 1 is plastic zone that concerns the determination of the material behaviour in the plastic state; most tool design parameters are determined by the work-material behaviour inside this area, such as stress, strain, and forming load. The second area is referred to as stock material that deals with the characteristics of the workpiece before deformation, which more or less influence the behaviour of the material in the deformation zone. Area 3 concerns the characteristics of component material. Area 4 considers the tool/work-material interface; friction and thermal contact on this interface play important part in tool design and component precision. Area 5 is the forming tool, dealing with the many-sided problems connected with tool layout and tool material. Area 6 is about the interface between work-material and forming environment; heat exchange on the interface and spring back influence the final component dimensions. Different forming processes may have different tool layout

and forming environment; however, their functional areas classification may be systematically the same [18]. A similar analysis for extrusion is shown in Fig. 2.14b.

Die surfaces geometry design means the design of die surface form according to the specifications of product dimensions, accuracy, and the current form-error of the component; this die surface will contact with work-material and forms the interface specified by Lange [18]. The inputs, resources and constraints for every activity at this level are not identical. For example, to functional components, the installation of tools on the forming equipment may be common; thus, the design, and the structural design of tools, should take into account the installation space as well as the distribution of T slots on press tables. There may not be a need for such considerations to consider the installation during the design die-surfaces.

The form and accuracy of the formed component are determined by the form and accuracy of the die surface. Thus, die surface design is an important link in process design. Component accuracy requirement, component form-error and possible forming defects (incomplete die filling, fracture initiation and folding) of the last design cycle should be considered during tool design iteration and die surface geometry design activity. Therefore, part of outputs of form comparison activity and FE simulation activity are feed back as part of inputs of tools design activity (Fig. 2.12); these are the inputs $I10, I12$ and $I13$ in Fig. 2.13. But these are not the original inputs; they are results of inter-middle design in the design iterations. In a similar way, die surface stresses, which are die surface strength related, should also be included. Component-forms are not replicas of the die-cavity. Die-elasticity, thermal effect on tools and workpiece, spring back of the formed component after ejection as well as the influence of secondary yielding [19] result in a difference between component-form and die cavity-form. The nett-shape forming of a component relies substantially on form-error compensation technology. The die surface design activity has been decomposed into preliminary die-surfaces design and form-error compensation design, as shown in Fig. 2.15.

The preliminary die-surface design activity refers to the design of die surface without form-error compensation. At this stage, a key input is the CAD definition of component geometry. Considering a multi-stage precision cold forming process, billet form, and the forming information from FE simulation activity of last design cycle are still required generally. Die surface finish requirements, lubrication conditions required during forming and the die-surfaces geometry without compensation should be determined by this activity.

The next activity begins with the pre-compensation, component form-error and compensation data from the form comparison activity, and the required component accuracy; conducting of the error-compensation design activity results in a CAD definition of new defined die surface to start a new iteration of error-compensation for die surface.

The new die surface with the required level of compensation can be derived using two approaches. One is direct die surface compensation, as shown in Fig. 2.16. During this activity, dimensions of the die surface without compensation, CAD definition of product geometry, product accuracy requirement and the component form-error or compensation data by form comparison activity (referred to Fig. 2.12) are required. Theoretically, compensation data can be determined by the form difference between specified component-form and the manufactured component-form (or the predicted component form using FE simulation). The compensation approach and procedure have been investigated into details [20]: form comparison determines component form-error; form-error is transited into new die-surface compensation-data that leads to a new CAD definition of die-surface.

The second method is a novel compensation approach proposed in this research. A profiled interference that depends on component geometry, work-material and die-stiffness, is specified between stress-ring and die insert. The die surface is profiled as a consequence of the prescribed distributed interference. The profiled interference can be determined by the form-difference between specified product form and the form predicted by FE simulation or the manufactured component form. The design

target is to obtain a profiled interference at shrink-fitting interface to render to the die surfaces a profile which would compensate for component form-error. To achieve this, all inputs required by direct die surface compensation, and tool stresses during forming are required, as shown in Fig. 2.16. These will be discussed into details in late related chapter.

Details of shrink-fitting form-error compensation approach are shown in Fig. 2.17. Four sub-activities of shrink-fitting compensation activity are defined. Shrink-fitting compensation data design is the first. Then, the design of a nominal die insert is required, which requires die design skills and special design knowledge from handbooks, and are modelled by the necessary mechanisms of the activity (Fig. 2.17). These would enables the development of a FE analysis model to establish the stiffness matrix describing the relationship between nodal deflection on the die surface and nodal interference at the shrink-fitting interface. The required profiled interference can be predicted further by the established matrix and required shrink-fitting compensation data acquired from activity at level A21221. From FE simulation, the nominal die insert and required distributed interference, the required die insert can be finalised.

2.5.3 FE simulation

The next activity is FE simulation of the precision cold forming process (refer to Fig. 2.12). Due to nonlinearity of the constitutive equations of most work materials, complexity of the geometry of the component and the interface conditions (friction, thermal contact conductance) [21], it would be difficult to predict the mechanical and thermal behaviour of work material during cold forming without FE simulation. Generally, the activity of FE simulation can be decomposed into three sub-activities: FE pre-processing, FE analysis and FE post processing, as shown in Fig. 2.18. The aim of pre-processing activity is to create the results of selected forming sequence and the designed tools into a format acceptable to the FE code. The CAD definition of tool geometry is transformed into mesh data; material properties, into material data; lubrication, surface texture are converted into contact conditions and interfacial data, and the forming sequence is transformed into different FE simulation stages.

Pre- and post-processing softwares are essential resources of process design (Fig. 2.18). After preparation of all necessary data, the FE analysis procedure can be initiated. The results of analysis are usually text and binary files containing information of stress, strain, displacement, velocity and forging force history. FE simulation is an iterative procedure. Termination of the analysis may be due to the selection of unsuitable forming sequences or tool design; for example, too large extrusion ratio may lead to simulation failure due to distortion of mesh. In such cases, information of failure simulation is fed back for the next iteration on forming sequence selection and tool design (see Fig. 2.12). However, suitable processes may not be simulated, either. The control parameters for FE analysis, –time increment, accuracy control or mesh control–, may prevent the convergence toward a solution. In this case, the information of failure analysis should be fed back into the pre-processing activity to update the corresponding control parameters or mesh to initiate a new simulation process.

2.5.4 Form comparison

As shown in Fig. 2.12, form comparison is an activity in which the component form-error and die surface compensation data are evaluated and designed. Form-error is determined by the difference between the required form specifications and the manufactured component form. The form difference is a consequence of the fact that either the compensation data was insufficient to achieve the required accuracy level or the manufacture error of the die-form. Component form can be either manufactured component-form measured by three-dimensional measurement equipment or computational component-form predicted by FE simulation [20]. Form-comparison can be achieved either by comparing the computational form and the specified component form, or by comparing the manufactured form and the specified component form. Thus, form-comparison is decomposed into four sub-activities: die surface form comparison, manufactured component form comparison, computational component form comparison and form-error and compensation data analysis [20], as shown in Fig. 2.19. Die surface form-comparison, which is the comparison between manufactured die surface form and specified die surface form, would indicate the departure of the die surface form from the designed die surface.

Manufactured component form comparison shows the difference between the manufactured component form from the specified component specifications. And computational form comparison determines the difference between computational component form and component specifications. And finally all these form differences are converted into a component form-error, and die surface compensation data if necessary, using form-error analysis software [20] by the form-error and compensation data analysis activity. The form-error analysis will result in only two consequences: either the form-error is within the specified accuracy requirement, or a new iteration is required.

2.5.5 Tools and component manufacturing activities and the iteration cycles

The designed tools should be manufactured by tool manufacturing activity. Manufactured tools then can be used to manufacture the component in the component manufacturing activity, as shown in Fig. 2.12. All information about tools is required by the tool manufacturing activity, the output of which is provided to the component manufacturing activity. Given all the information in the preceding activities, the manufacturing activity will produce a component, the accuracy of which depends on the current stage of iteration.

There are a few important iterative design cycles that show the notable characteristics of precision cold forming process design, as shown in Fig. 2.12. The first is the iteration between forming sequence selection and tools design, which shows interdependence between these two activities. The second interdependence is between activities A1, A2 and A3. These are the cycles using FE simulation to verify forming defects, forming parameters and tools strength. The preliminary forming sequences and tools are simulated by FE analysis. The simulated results are then fed back into forming sequence selection or design activities in order to refine the design. The activities A2, A3 and A4 would be the commonly used design cycle, referred to as *small design iteration*. The designed tools would provide the computational component form after FE simulation, which is transported into the form-comparison activity to obtain the predicted computational component form-error and compensation data. Thus, the obtained compensation data is fed back to the

tools design activity to determine the die surface compensation and obtain new tools design which can be verified by FE simulation and form-comparison activities, again. Several iterations can be performed, till the computational component form error is within requirements [23]. The accuracy and number of these iterations depends on the accuracy of the inputs to the FE simulation activity, component form, especially the material properties and interface parameters.

A *big design iteration* cycle is also provided by the output of product manufacturing activity. The manufactured component (in fact, component form) is fed back into the form-comparison activity to evaluate the component form-error and compensation data. The form-error or compensation data are further fed back into tool design activity or forming sequences selection/design activity to guide the die surface compensation design or forming sequence selection/design. This is the general iterative approach for design precision cold forgings without FE simulation [23]. If the tool manufacturing and product manufacturing cycles were incorporated, this procedure would prove to be expensive with long leads time. However, the product form-error is measured through form-comparison and includes the influence of die elasticity, thermal expansion/contraction, and possibly secondary yielding [19]. Therefore, all compensable form-error factors can be considered for the compensation. The precision cold forming process design iteration can be symbolically expressed by the graph in Fig. 2.20, where, DFORM refers to die-form, CFORM to component-form, CSFORM to the specified component form and ERR refers to component form-error and compensation data. During the n^{th} iteration, the n^{th} component form is manufactured by the n^{th} die-form and trial; comparison of the n^{th} component form with the specified component form results in the n^{th} component form-error and compensation data for next iteration. The n^{th} component form-error, compensation data and n^{th} die form would lead to the $(n+1)^{th}$ new die form by die surface compensation design, from which the new component form can be obtained. This iteration is continued, till the component form-error is within required accuracy. Both small iteration and big iteration can be described by Fig. 2.20; the difference lies in that in case of small iteration, component form is predicted by FE simulation

while in case of big iteration, it is determined by manufacturing process and component form measurement.

The above-discussed iterative procedure is also applicable to multi-staged precision cold forging processes. Generally, the component accuracy is determined by the last stage-operation. Therefore, the above-discussed iterations can be also considered for the design of the last operation for a multi-staged cold forging process.

The combination of small and big iterations is shown by a flowchart in Fig. 2.21. Perhaps the most effective and economical design iteration is the combination of small and big design iterations. Both iterations begin with tools design. In small iteration, tool design results are used to initiate FE simulation of forming process; thus the computational component form can be obtained. After form-comparison and evaluation of component-error, the continuation of small iteration can be determined by the computational component-error: if it is within component requirement, small iteration can be terminated; or next small iteration starts. If computational component-error is predicted small, big iteration can be initiated by tools manufacturing and component manufacturing. After manufactured component form-comparison, manufactured component form-error is evaluated. If all parameters used in FE simulation, such as material constitutive equations, interface parameters, are sufficiently accurate, theoretically, both computational and manufactured component form-errors should be nearly equal and small, as the result of small iterations. However, interface parameters (friction and thermal contact conductance) are difficult to control and unstable. Therefore, the manufactured component form-error is still probably exceeded the requirements. There are two paths to continue the iterations. One is direct use of manufactured component form-error to generate die surface compensation data to continue the big iteration till the manufactured component form-error within requirement. The other path is update the parameters used in FE simulation to return to the small iteration again, as shown in Fig. 2.21.

Theoretically, if the input data of FE simulation activity are accurate, the form-error predicted by FE simulation should be the same as that achieved by measurement.

From this point of view, improving accuracy of the input data of FE simulation activity is an economically effective way leading to low cost design of precision cold forgings. However, all constitutive equations used to describe material mechanical behaviour are not accurate; interfacial parameters (friction, thermal contact conductance) are difficult to control and sometime unstable; composition of work-material is variable even in the same stock. It is impossible to control all input data to FE model sufficiently accurate for all these reasons. Therefore, the big design iteration would remain necessary for precision cold forging process design. At the same time, the fluctuation of work-material composition, leading to variable mechanical properties, will influence the form-error of component during manufacturing.

2.6 Decision-tree of precision cold forging design process

Finally, the decision-tree of precision cold forming process design is shown in Fig. 2.22. The so-called decision-tree is actually the checklist of decomposition of necessary activities of the precision cold forming process design. From this tree, it is clearly seen how every activity is suitably decomposed and which activity needs more detailed decomposition and which one will need more efforts to develop. With the development of precision cold forming technology, some activities may need more detailed decomposition and new activities may be developed which will lead to the growth of the tree. For example, the new forming process development and process optimisation may lead to the growth of the branch of forming sequence selection/design activity. On the other hand, redundant activities may be pruned from the tree. Activity of pruning and growth of the tree reflects the development of precision cold forging technology.

2.7 Conclusions

1. The IDEF0 methodology has been successfully used for the functional modelling of precision cold forming process design.

2. The component form-error compensation process and the iteration design procedures are modelled into detailed activities. The required inputs, supporting

resources and constraints of every activity or sub-activities are defined; especially the possible iterative design procedures are modelled into details.

3. The established IDEF0 model for precision cold forming process design provides a basis for further investigation of precision cold forging process.

4. The basic ideas for the rest investigation of this research are presented in the section by IDEF0 modelling, in particular the importance of interface parameters and the idea of shrink-fitted die surface form-error compensation proposed, which will be further researched and discussed in late section.

2.8 References

1. A. Plaia and A. Carrie, Application And Assessment of IDEF3-Process Flow Description Capture Method, International Journal of Operations & Production Management, Vol. 15, No. 1, pp. 63-73, 1995
2. C. L. Ang, et al, IDEF*: A Comprehensive Modelling Methodology for The Development of Manufacturing Enterprise Systems, International Journal of Production Research, Vol. 37, No., 17, pp. 3839-3858, 1999
3. K. Jeong, Conceptual Frame for Development of Optimised Simulation-Based Scheduling Systems, Expert Systems with Applications, Vol. 18, pp. 299-306, 2000
4. T. H. Soon and R. D. Souza, Intelligent Simulation-Based Scheduling of Workcells: An Approach, Integrated Manufacturing systems, Vol. 8, No. 1, pp. 6-23, 1997
5. A. M. A. Al-Ahmari and K. Ridgway, An Integrated Modelling Method To Support Manufacturing System Analysis and Design, Computers in Industry, Vol. 38, pp. 225-238, 1999
6. T. Perera and K.Liyannage, Methodology for Rapid Identification And Collection of Input Data in The Simulation of Manufacturing Systems, Simulation Practice and Theory, Vol. 7, pp. 645-656, 2000
7. A. Kusiak and A. Zakarian, Risk Assessment of Process Models, Computers & Industrial Engineering, Vol. 30, No. 4, pp. 599-610, 1996

8. K. Santarek and I. M. Bueif, Modelling and Design of Flexible Manufacturing systems Using SADT and Petri Nets Tools, Journal of Material Processing technology, Vol. 76, pp. 212-218, 1998
9. Y. M. Chen, Development of A Computer-Aided Concurrent Net Shape Product And Process Development Environment, Robotics & Computer- Integrated Manufacturing, Vol. 13, No. 4, pp. 337-360, 1997
10. N. Nagarur, et al, Methodology for Developing Maintenance Management Systems Using Object orientation, Human factors and Ergonomics in Manufacturing, Vol. 9, No. 1, pp. 27-47, 1999
11. D. M. Min, et al, IBRS: Intelligent Bank Reengineering System, Decision Support Systems, Vol. 18, No. 1, pp. 97-105, 1996
12. D. C. Gong and K. F. Lin, Conceptual Design of Shop-Floor Control System from IDEF0, Computers & Industrial Engineering, Vol. 27, No. 1-4, pp. 119-122, 1994
13. L. Lu, et al, Integration of Information Model (IDEF1) with Function Model (IDEF0) for CIM Information Systems Design, Expert Systems with Applications, Vol. 10, No. ¾, pp. 373-380, 1996
14. C. L. Ang, Enactment of IDEF0 Models, International Journal of Production Research, Vol. 37, No. 15, pp. 3383-3397, 1999
15. R. Lee, et al, Development of A Parametric Computer-Aided Die Design System for Cold Forging, Journal of Materials Processing Technology, Vol. 91, pp. 80-89, 1999
16. Q. Hsu and R. Lee, Cold Forging Process Design Based on the Induction of Analytical Knowledge, Journal of Materials Processing Technology, Vol. 69, pp. 264-272, 1997
17. R. Duggirala et al, Computer Aided Approach for Design and Optimisation of Cold Forging Sequences for Automotive Parts, Journal of Materials Processing Technology, Vol. 46, pp. 185-198, 1994
18. K. Lange, Handbook of metal forming, pp. 15.1-15.99, McGraw-Hill, Inc. 1985
19. A. Rosochowski and R. Balendra, Effect of Secondary Yielding on Nett-Shape Forming, Journal of Materials Processing Technology, 1996, Vol. 58, No. 2-3, pp. 145-152.

20. R. Balendra, Y. Qin, X. Lu, Analysis, Evaluation and Compensation of Component-Errors in the Nett-Forming of Engineering Components, Journal of Materials Processing Technology 106: (1-3) 204-211 OCT 31 2000
21. R. Hill, The Mathematical Theory of Plasticity, Oxford: Clerandon Press, 1983
22. H. Kim, T. Yagi and M. Yamanaka, FE Simulation as a Must Tool in Cold/Warm Forging Process and Tool Design, Journal of Materials Processing Technology, 98: (1) 143—149, 2000
23. H. Ou, R. Balendra, Die-Elasticity for Precision Forging of Aerofoil Sections Using Finite Element Simulation , Journal of Materials Processing Technology, 76: (1-3) 56-61 APR 1998

Chapter Three

Experimental Investigation of Thermal Contact Conductance

3.1 Summary

Several different approaches have been used for the evaluation of thermal contact conductance; steady-temperature based, transient-temperature based, calibration and electric-resistance-based methods have been used to assess thermal contact conductance for different interfacial pressures. The influence of surface texture has not been considered. Thermal contact conductance at high pressure was usually defined using the calibration or reverse method. The surface texture of the tool and billet, and the interfacial pressure have a strong influence on heat transfer. Therefore, it is necessary to study thermal contact conductance under different surface textures and interfacial pressures.

A new steady-temperature based thermal contact conductance measuring equipment was used in the reported investigation of thermal contact conductance. Using this equipment, both, the tool and the specimen, can be changed. Thus different contact materials can be matched; interfacial pressure can be adjusted and maintained and temperature in thermal contact interface can be pre-set. This equipment allows the definition of thermal contact conductance as a function of interfacial pressure, surface texture, temperature and materials. In this investigation, thermal contact conductance was only considered as a function of surface texture and interfacial pressure. Data processing techniques were developed for variable tool conductivity conditions. FE simulation of test process enabling one-dimensional heat flow was achieved. Tool surface is smoother than that of specimen.

It is found that about 5 times thermal contact conductance can be achieved for fine specimen ($R_a \approx 0.3\,\mu m$) as those of coarse specimens ($R_a \approx 4\,\mu m$). Thermal contact conductance varies from 7~30 $kWm^{-2}K^{-1}$ under an interfacial pressure of 30 MPa to

40~150 $kWm^{-2}K^{-1}$ under 180 MPa, and is approximately a linear function of the nominal interfacial pressure, up to 180 MPa for the matched materials N910 and Ma8. Surface macro-irregularities have a strong influence on the evaluation of thermal contact conductance. Uncertainties of the computed thermal contact conductance are found to be a function of surface texture, interfacial pressure, positioning and the accuracy of the thermocouples. Threshold interfacial pressure, for the evaluation of the thermal contact conductance, is also defined.

3.2 Nomenclature

c	Specific heat of the heat transfer material	$J\,kg^{-1}\,K^{-1}$
C	Integration constant	
h	Thermal contact conductance	$kW\,m^{-2}\,K^{-1}$
k	Thermal conductivity	$W\,m^{-1}\,K^{-1}$
$\bar{k}$	Function defined by equation (3.1-6) in Appendix 3.1	
n	Number of thermocouples in a tool	
q	Heat flux density	$kW\,m^{-2}$
R_a	Surface roughness	μm
R_t	Total height of surface profile	μm
R_q	Root mean square deviation of surface profile	μm
$(R_a)_p$	Surface roughness of tool surface parallel to the grinding direction	μm
$(R_a)_t$	Surface roughness of tool surface transverse to the grinding direction	μm
$(R_a)_i$	Initial surface roughness	μm
T	Temperature	K
t	Thickness of specimen	mm
ΔT	Temperature drop or difference	K
z	Location co-ordinate along tool axis	
α	Uncertainty coefficient of h-value	
$\vec{\nabla}$	An differential operator $\nabla = \vec{i}\frac{\partial}{\partial x} + \vec{j}\frac{\partial}{\partial y} + \vec{k}\frac{\partial}{\partial z}$	

ρ	Mass density of heat transfer material	$kg\,m^{-3}$
τ	Time	s
ψ	Rate of internal energy generation	$J\,m^{-3}\,s^{-1}$
$\varepsilon_1\ \varepsilon_2$	Convergence control parameters	
$\overline{\sigma}$	Specimen material flow strength	MPa
$\overline{\varepsilon}$	Equivalent strain	
δT_0	Maximum uncertainty of thermocouple	K
δx_0	Maximum uncertainty of thermocouple location	mm
δ	Prefix shown the corresponding uncertainty, variance or covariance	
$\vec{T}$	Vector to show temperature distribution	
$\vec{X}$	Vector to show thermocouple locations	

Subscripts

0	Origin
1	Different constant
2	Different constant
an	Analytical or theoretical result
ex	Experimental
FE	FE simulation
f	Surface
i	The i^{th} thermocouple location on upper tool
m	The m^{th} thermocouple location on lower tool
j	The j^{th} iteration
ic	Inside cooler
oc	Outside cooler
s	Specimen
t	Tool
∇	Lower
Δ	Upper
H	Heater

Superscripts

(i) The i^{th} iteration

(j) The j^{th} iteration

Example: $t\nabla f$ shows lower tool surface; ΔH shows upper compensation heater.

3.3 Glossaries

Macro-irregularities of surface: When the specimen is in contact with the tool under a given nominal interfacial pressure, it was observed that the distribution of contact marks was not uniform; contact asperities were focused in some areas, while asperities in other areas were rarely in contact. This contact difference may occur in an area with dimensions comparable to those of the specimen. Therefore, it is a macro surface phenomenon. This non-uniform distribution of contact marks is different for each specimen with a random pattern. It is referred to as macro-irregularities of the specimen surface, short for *macro-irregularities*.

Threshold level of interfacial pressure: Experimental results will not be repeatable beyond a value of the nominal interfacial pressure. This interfacial pressure is referred to as threshold level of interfacial pressure.

Area ratio: Considering the actual surface geometry, contact only occurs on some local areas in the domain of nominal contact area for any of two mechanically contacted surfaces. Thus, the nominal contact area can be divided into a real contact area and a non-contact area. The ratio of the real contact area to nominal contact area is referred to as real area ratio, short for *area ratio*.

3.4 Introduction

Heat flux density through two mechanically contacted surfaces is assumed to be proportional to the temperature drop across the interface; the proportional coefficient is referred to as thermal contact conductance (h, or h-value). Thermal contact conductance is an important interfacial parameter in precision cold forming process design since it influences temperature distribution in the component and tools.

Consequently, it has an influence on component form accuracy. Experimental methods of determining h, from early 1960's [1] to the present, were based on the measurement of temperature change at interfaces in most cases. The methods used for the measurement of h may be classified, as in Fig 3.1. Generally, measurement methods can be classified as temperature and non-temperature based. Non-temperature based methods measure the interface electrical resistance across the interface; this is directly proportional to h [2]. This method has not been widely used since it was difficult to evaluate the influence of the resistance of junctions between cables and test surfaces.

Temperature-based methods can be further divided into transient and steady-state methods. The steady-state method requires the establishment of a stable, one-dimensional temperature field. Regression analysis is used to extrapolate temperature at the interface. The schematic of the experimental approach for measurement of thermal contact conductance is shown in Fig. 3.2. Heat is transferred into the upper tool by the heat source while the heat sink draws this energy through the lower tool [3]. Thermocouples are embedded along the axes of both tools. If the surfaces of the tools are placed in contact, with or without specimen between them, the heat will flow through the upper and lower tools towards the heat sink. A one dimensional heat flow can thus be effected if suitable heat insulation and temperature compensation devices are installed around the tools. Using the temperatures at the thermocouples, regression analysis and interpolation can be applied to calculate temperature at the contact surfaces. Thus, the temperature drop ΔT_{stf} at tool-specimen interface and heat flow density q through both tools can be obtained, and h can be computed using the following equation:

$$h = \frac{q}{\Delta T_{stf}} \tag{3-1}$$

This method was used extensively [4~13]; in most cases, the value of h was evaluated, however, under low interfacial pressure. Lambert [4] measured h at 1 MPa; Chung [5-6] and Parihar et al. [7] at even lower pressures; Blanchard et al. [8] and Parmenter et al. [9] conducted experiments for interfacial pressures of approximately 10 MPa; Marotta et al. [10-11] performed experiments at 4 MPa.

These results are not suitable for the analysis of cold forming due to the low interfacial pressure. Further, most of these experiments used one specimen for every measurement [4,7-8,10]; some of them used two or more specimens [5-6,9]. In some cases, h was measured without a specimen [12]; in such cases, it would be difficult to establish the relationship between h and surface texture. A tool could only provide one initial surface texture; in the event more than one specimen was required, it would be difficult to prepare specimens with identical surface texture.

The alternative method requires the measurement of temperature during a transitional process. Such approaches were said to represent the dynamic conditions on metal-forming conditions [13]. The temperature-field near the contact interface is assumed to be one-dimensional even in complex fields of heat flow [14]. This transient temperature based approach encompasses the calibration method, reverse method and surface temperature measuring method.

Before surface thermocouples were invented, sub-surface temperatures were used to extrapolate with a view to defining the surface temperature. This method was used by Beck [15]. Direct measurement of surface temperature was made possible using surface thermocouples designed by Vigor and Hornaday [16] and developed further by Kellow et al. [14]. These were used for measuring die surface temperature in drop forging by Dean and Silva [17], in rolling by Stevens et al. [18], and in upsetting by Semiatin et al. [19]. Lenard and Davies [20] placed thermocouples in a groove on surface to measure surface temperature instead of surface thermocouple. For all cases, the h-value was computed from experimental results derived from methods catalogued in Fig. 3.1. These thermocouples were, however, not always reliable for surface temperature measurement. The high pressures and temperatures encountered at the die surface, especially in hot forging, often damaged these surface thermocouples. Replacement of surface thermocouples is difficult since the preparation of surface thermocouple is an integral part of the tool surface manufacturing process [17].

The Calibration method is a combination of experiment and numerical analyses. Temperature on the tools varies with time. Numerical analysis, usually finite difference or finite element methods, is used to predict the profile of temperature, as a function of time. FE simulations were performed with assumed h-values and the temperature contour that corresponded to the measured profile was assumed to be the prevailing h-value. Brute, et al. [21] used this method to predict h-value for hot forming. Nshama and Jeswiet [22] used both, the sub-surface and surface thermocouples, to measure temperature; this was combined with Finite Element analysis to predict the h-value at the forming tool. Semiatin, et al [19], Dadras and Wells [23], Shamasundar, et al. [2], conducted similar research. The h-value was, in these cases, considered constant and provided the basis for calibration curves. This approach discounts the dependence of h on surface texture and interfacial pressure.

The reverse method was presented by Nshama,et al. [24], and developed further by Hu, Brooks and Dean [13]. This approach, similar to the calibration method, combined experiment and numerical analysis. The reverse method employed both, mathematical and finite element analyses, to obtain a value of h. Least-squares analysis was used to minimise the difference of temperature between experiment and FE prediction [13]. It is worth noting that reverse method was further developed by the research of Malinowski, et al [25]; the least-squares method was combined with finite element method to minimise the difference of temperature versus time between experiment analysis and FE simulation. In this manner, the reverse method, instead of providing an approximating value of h at the interface, regarded h as a function of temperature and pressure. However, the influence of surface texture had to be ignored due to the limitation of both, the experimental technique and FE simulation. There is a particular difficulty in modelling micro geometry of surfaces.

The surface textures of tool and billet, the nominal interfacial pressure and lubricant on the tool-billet interface may play important parts in thermal contact conductance in cold forming. The h-value at high interfacial pressure and cold forming temperature should be experimentally investigated. In this research only the

influence of interfacial pressure and surface texture on h will be considered, and the interface is considered clean.

3.5 Experimental equipment and considerations

3.5.1 Considerations in the use of the steady-state method

The general equation of heat transfer [26] is

$$\vec{\nabla}\cdot(k\vec{\nabla}T)+\psi=\rho c\frac{\partial T}{\partial \tau} \tag{3-2}$$

This equation defines the internal energy balance in an element of heat transferring material. For one-dimensional steady-state heat transfer, without internal heat generation, the equation (3-2) may be simplified to:

$$\frac{d}{dz}\left(k\frac{dT}{dz}\right)=0 \tag{3-3}$$

from which:

$$k\cdot\frac{dT}{dz}=q \tag{3-4}$$

where q is referred to as heat flux density in heat transfer, denoting the energy across unit area in unit time. Equations (3-3) and (3-4) define the characters of one-dimensional steady heat flow; heat flux density should be constant and proportional to the temperature gradient in a one-dimensional heat flow field. The coefficient is referred to as the conductivity of the material in heat transfer. If the conductivity of material is constant, from equation (3-4) we have:

$$T=\frac{q}{k}z+T_0 \tag{3-5}$$

If temperatures along the axis of the tool are measured (see Fig. 3.2), regression analysis can be applied to obtain the approximate values of q and T_0. The temperature at any cross-section of the tool can be predicted by interpolation; in particular, the temperature at the contact surface can be predicted in this way. By applying equation (3-5) to the specimen, the conductivity of which is constant, we can have temperatures $T_{s\Delta f}$ and $T_{s\nabla f}$ at contact surfaces of the specimen

$$T_{s\Delta f}=\frac{q}{k_s}z_{s\Delta f}+T_{s0} \tag{3-6}$$

$$T_{s\nabla f} = \frac{q}{k_s} z_{s\nabla f} + T_{s0} \tag{3-7}$$

The difference between equations (3-6) and (3-7) defines the temperature drop ΔT_s through the specimen

$$\Delta T_s = \frac{q}{k_s} t \tag{3-8}$$

Assuming that the surface texture on both surfaces of the specimen is the same, the temperature drops at the two contact interfaces should be also the same. Thus, the contact interface temperature drop ΔT_{stf} is

$$\Delta T_{stf} = \frac{1}{2}\left(T_{t\Delta f} - \frac{q}{k_s} t - T_{t\nabla f} \right) \tag{3-9}$$

and

$$h = \frac{q}{\Delta T_{stf}} \tag{3-1}$$

Equation (3-1) is the foundation of conventional steady-state temperature based h computational method. Summarising the above analysis, the important assumptions used in steady-state temperature measurement methods are as following:

- Temperature field is one-dimensional, or heat flux density is constant for the upper tool, lower tool and the specimen;
- Surface textures on both sides of the specimen are identical;
- Variation of thickness of specimen should be considered in the computation if plastic deformation occurred during the test;
- Surfaces of specimen and tool are clean without contaminants/oxidants;
- The conductivity of the upper tool, lower tool, and specimen are constant within the working temperature.

It should be noted that the temperature being one-dimensional is a key requirement for the analysis. One-dimensional heat flow field condition can only be made possible by an elaborate configuration of thermal balancing devices in the experimental equipment. The fact has not been emphasised sufficiently [3~12]. The second assumption refers to the preparation of test specimens: both surfaces of the specimen must be manufactured to identical specifications. Specimen thickness should be measured to evaluate the temperature drop on the specimen (refer to

equation (3-8)), especially when pressures in excess of the yield strength are applied. Surfaces of specimens should be protected form contamination and rusting. Therefore, specimens should be kept in a sealed container with desiccating agent. Before a test, the specimen surface should be cleaned with chemical solution such as ethyl alcohol.

Lately, it has been found that tool material conductivity may vary with temperature. In cases when the variation of conductivity has to be accounted for in equation (3-4), a different approach to solving equation (3-4) would be required; this is attended to in the following text.

3.5.2 Structure of the experimental equipment

3.5.2.1 Structure

Structural details of the experimental equipment are shown in Fig 3.3. Load cell 1 is used to record the force loaded on specimen 14 during an experiment. The upper cooler 2 and insulator 4 prevent heat flow from main heater 7 to the load cell. Radiation shield 3 prevents heat exchange between the tools and the environment. Upper tool 5 is connected to load cell 1 by the insulator 4. The main heater 7 is fixed at the upper part of the upper tool to provide a source of heat. Surrounding the upper tool 5 is a ceramic insulator 6 which is attached to the upper tool by the upper frame 8. Outside this frame, an upper compensation heater 9 is used to balance the possible heat exchange between upper tool 5 and the upper-frame 8. Between the upper tool 5 and lower tool 17, is the specimen 14 that can be compressed by the tools. There are four thermocouples 11 and 16 embedded in both, the upper and lower tools, labelled 1c~4c and 5c~8c respectively, for recording temperature distribution along axes of the tools. The lower compensating heater 13 is fixed outside the lower-frame 22, which is used to balance the possible heat exchange between tools and frames. The inner cooler 20 is attached to the bottom of the lower tool; the outer cooler 19 is attached at bottom of lower-frame 22 to control the temperature of lower-frame. All components attached to the upper tool are held together by the upper-frame, which is connected to the press ram cylinder through load-cell 1. All components attached to lower tool are held together by the lower-frame which is mounted onto the bed of the

press though seat 21. Thus the upper tool, together with all components attached to it, can be moved relatively to the lower tool enabling the compression of specimen 14. Interfacial pressure can be controlled by the press hydro-system and maintained by a mechanical device. Test conditions, such as temperature, pressure and specimen surface texture can be set and controlled in this experimental equipment.

3.5.2.2 Control principle

Fig. 3.4 shows the control system for the experimental equipment. The main heater controller controls temperature of the main heater 3. The upper compensation heater controller controls the temperature difference between the main heater 3 and upper compensation heater 5. A balanced state can be achieved between the main heater 3 and the upper compensation heater 5 to prevent the heat exchange between the upper tool 1 and the environment to establish a one-dimensional heat transfer field. The lower compensation heater controller controls the temperature difference between tools close to the specimen 8 and lower compensation heater 9. The outer and inner cooler temperature controllers control the temperatures of outer cooler 12 and inner cooler 13 respectively. Controlling the temperatures of the main heater and the inner cooler may provide a temperature field with different temperature gradient and different temperature at contact interfaces. Controlling the temperature of the upper compensation heater, lower compensation heater and the outer cooler can establish a temperature field matching that along the tool axes, and heat transfer between the tools and the environment is thus reduced or prevented. Therefore, a one-dimensional steady temperature field with the required temperature gradient along the tools may be established by setting the temperatures of the heaters and coolers.

Temperatures of the two compensation heaters are adjustable and controlled to within $\pm 0.1^{\circ}C$ by the control system. Temperatures of inner and outer coolers are also adjustable and controlled to within $\pm 0.1^{\circ}C$ with temperature stability to within $\pm 0.01^{\circ}C$. Principally, the design can effectively prevent the transverse heat exchange to make sure the heat flow in the tools is one-dimensional. The basic temperature control parameters are the temperature difference $\Delta T_{II\Delta II}$ between the

main heater and upper compensation heater, the temperature difference $\Delta T_{s\nabla H}$ between specimen and lower compensation heater, the outer cooler temperature T_{oc} and the inner cooler temperature T_{ic}.

3.5.3 Data processing technique with variable conductivity

Tools were made of N910 steel. Thermal Conductivity of the tool material has been considered constant [3~12]. Thermal Conductivity of N910 was measured at the National Physical Laboratory (NPL); this may be defined by the following empirical equation up to 300 $^{\circ}C$ and is shown in Fig. 3.5:

$$k_t = 19.21 + 1.43 \times 10^{-2} T \quad \left(Wm^{-1}K^{-1}\right) \tag{3-10}$$

Equation (3-10) shows that the conductivity of N910 is the function of temperature. The temperature variation along the tools in the experiments may change from 200°C to about 10°C. The corresponding variation of conductivity is shown in Fig. 3.5, which appears to be a linear function of temperature. This variation may introduce uncertainties in the experimental results if the conductivity is replaced by a constant. A numerical solution of differential equation (3-4) was obtained when thermal conductivity k_t is considered as function of temperature; based on this, a data processing approach was developed in order to avoid introducing uncertainty due to variation of tool material thermal conductivity with temperature. Details are attached to appendix 3.1.

3.5.4 Establishment of experimental settings using FE simulation

The experimental equipment enables the establishment a one-dimensional heat flow field if all four-control parameters, $\Delta T_{H\Delta H}$, $\Delta T_{s\nabla H}$, T_{ic} and T_{oc}, are suitably set. Trial-and-error to achieve a steady-state may be too time-consuming. At the same time, the correct settings of the control parameters may change as contact and environment conditions change. Settings during the early morning of the day may be not suitable in the late afternoon due to the change of environmental temperature. Therefore, it is imperative that a practical approach is determined.

FE simulation of test process turned out to be an effective approach to adjudge whether the settings of the experiment are appropriate. Considering the case when the top-most thermocouple temperature (at location $z_{i\Delta}$) is $T_{i\Delta}$, the lowest thermocouple (at location $z_{i\nabla}$) temperature is $T_{i\nabla}$, as shown in Fig. 3.6. If temperature field between them is one-dimensional, the temperature distribution is thus uniquely determined by the thermal contact conditions. For instance, when the interfacial pressure is zero, or there is a gap between contact surfaces, the temperature drop ΔT will be approximately $T_{i\Delta} - T_{i\nabla}$ since air is a good insulator [26]. In this case the value of h is small due to big thermal contact resistance which results in small heat flux density, as shown by the graph labelled 3 in Fig. 3.6. When interfacial pressure is relatively high, the temperature drop ΔT will be small due to the small thermal contact resistance under high interfacial pressure; the corresponding h can be large, and the temperature distribution is nearly a straight line, as shown by the graph 1 in Fig. 3.6. Any intermediate one-dimensional case can be described by a unique graph between curves 1 and 3, depending on the corresponding value of h. However, if the temperature field is not one-dimensional, distribution of temperature cannot coincide with any of the graphs that display one-dimensional heat flow. This fact provides the basis for verifying whether the heat transfer field in the experiment is one-dimensional by simulation of heat flow process using FE. Obviously, $T_{i\Delta}$ and $T_{i\nabla}$ as temperature boundary conditions, the measured value of h as thermal contact condition, it is possible to establish a FE model, which can predict the corresponding temperature distribution even if the conductivity of the tools is not constant. If the temperature field difference between FE simulation and experiment is small, of the order of 0.1 $^{\bullet}C$, the temperature field is considered one-dimensional. This value is based on experimental experiences. FE simulation of experiment process may also provide information for resetting the control parameters to achieve one-dimensional heat flow. In a word, in order to appropriately set the experiment control parameters as soon as possible, a FE simulation of test process, a comparison of experimental and FE simulation results, and the resetting of the control parameters according to the comparison consequence, are required.

3.5.4.1 FE geometric model and boundary conditions

In order to observe the simulation results easily and visually, an axisymmtrical geometric model was used for simulation, as shown in Fig. 3.7. It is a simple model of the upper tool, test specimen and the lower tool. The temperatures, at the top nodes corresponding to the upper-most thermocouple on the upper tool, and at the lowest nodes, corresponding to the lower-most thermocouple on the lower tool, were fixed at the corresponding temperatures obtained from the experiment. The value of h on both interfaces are set at the value obtained experimentally. Film coefficient of the cylinder surfaces of the tools and specimen were set to zero since it is assumed that there was no transverse heat flow due to the experimental settings.

3.5.4.2 Thermal properties of materials

Thermal properties which are required by the heat transfer FE simulation are shown in Section 3.6.

3.5.4.3 Control parameters settings and resetting

Complex analysis is involved in the establishment of experimental equipment setting or resetting approach; this is achieved by comparing the temperature field measured experimentally with that predicted by FE simulation. The details of the comparison between FE simulation and experimental temperature fields and the test control parameters setting will be discussed in section 3.9; the flowchart of the experimental equipment setting and resetting approach is shown in Fig. 3.8

3.5.5 Calibration of thermocouples

K-type thermocouples were employed; the accuracy of these thermocouples was specified by the manufacturer as $\pm 1.5\,^{\circ}C$. In the experimental investigation, when interface pressures of 180 MPa were used, the temperature drop across the interface is of the order of 0.2~0.8°C. Therefore, these thermocouples had to be calibrated prior to use.

Commercially available thermocouples are usually not calibrated individually. Due to random factors in the manufacturing process and the variation of the coupled

junction-materials compositions, systematic or random uncertainties are introduced. Fortunately, the main contribution to the uncertainties in the output of K-type thermocouples, as shown by this calibration procedure, is systematic. After calibration, the measuring accuracy can be as high as $\pm 0.1^{\circ}C$. Details of the calibration procedure and results are provided in Appendix 3.2.

3.6 Tools and specimen materials

Both tools were manufactured from N910 steel, the conductivity of which was verified by The National Physical Laboratory and is shown by equation (3-10). Tools were heat-treated to hardness of HRC 58~62 prior to use; therefore, tools can be considered rigid or elastic during FE simulation. Surfaces of the tools were ground with surface roughness between 0.2~0.3 μm. Specimens were made from material Ma8 steel, conductivity of which is 60.0 $\left(Wm^{-1}K^{-1}\right)$ up to 150°C and the strain-stress property can be defined by

$$\overline{\sigma} = 650\left(\overline{\varepsilon} + 0.02\right)^{0.22} \quad (MPa) \tag{3-11}$$

Temperature influence within 150 °C on flow strength is assumed to be negligible. This data is provided by Philips.

3.7 Experimental procedure

3.7.1 Specimen preparation

Material of specimen is specified in section 3.6. Owing to the simplification of late theoretical analysis, computation of h requires that contact between tools and specimen is uniform. Therefore, the surface texture of specimen should be isotropic and uniform, and the macro-irregularities of the surface should be as small as possible. EDM (Electrodischarge-Machining) was used to manufacture specimens to meet these conditions. Mechanical cutting and grinding operations were first applied to produce specimens of approximate dimensions; then EDM was used to refine the specimen to the required surface texture and dimensions. Different surface textures were obtained by changing the discharge parameters of the finish-machining operation, such as current, voltage, and discharge-gap. The selected specification of the specimens is shown in Table 3.1, in which parameter t is the thickness of the

specimen; R_a shows the surface roughness range of specimens. In practice, although manufacturing parameters can be set at the same level for different specimens, the actual specimen surface roughness varies due to random factors. All specimens are 18 mm in diameter to match the tools dimensions; different thickness, 1.00, 1.50, 2.00, 2.50, 3.00 and 4.00 mm respectively, were used to evaluate the influence of the thickness on the accuracy of test results. In order to evaluate the influence of surface texture on thermal contact conductance, six different surface texture ranges, labelled with A, B, C, D, E and F respectively (refer to Table 3.1), were used.

Table 3.1 Preparation of specimens dimensions and surface texture

R_a scale \ t (mm)	1.00	1.50	2.00	2.50	3.00	4.00
A (0.25~0.35) μm	1	1	1	1	1	1
B (0.37~0.48) μm	1	1	1	1	1	1
C (0.74~0.97) μm	1	1	1	1	1	1
D (1.74~2.21) μm	1	1	1	1	1	1
E (2.49~2.86) μm	1	1	1	1	1	1
F (3.51~4.97) μm	1	1	1	1	1	1

3.7.2 Experimental procedure

The surface texture of the specimen was measured prior to the application of pressure on a surface texture-measuring machine, SURFTEST-400 profile-meter. Specimens were coded; typically the specimen 2.0-C-000 had the specification: 2.0= nominal thickness of the specimen, C= initial surface texture range of the specimen (refer to Table 3.1), 000=interfacial pressure applied prior to the surface texture measurement. The corresponding surface texture parameters such as surface roughness R_a, root mean square deviation R_q, height of surface profile R_t, mean spacing S, the profile of the measured surface and the bearing ratio curve were recorded. Before conducting thermal contact conductance experiments, specimen surfaces were cleaned with industrial ethyl alcohol. Thermal contact conductance experiments were conducted on each specimen for a particular interfacial pressure. A one-dimensional heat transfer field must be established; control parameters should be set appropriately. The control parameters setting and resetting approach shown in Fig. 3.8 was employed to set or reset the experiment equipment according to the environment. Temperature at locations of thermocouples were recorded and

compensated with the calibrated results (Appendix 3.2) when a one-dimensional heat flow field was established; the data processing approach developed in Appendix 3.1 was used to evaluate the corresponding temperature drop and heat flux density, from which the h-value was computed. Data was recorded, as shown in Appendix 3.3, for each experiment. Upon completing of the experiment, the surface texture of the specimen was measured and recorded, again.

Experiments were repeated when the h-value appeared to be unusual for the given interfacial pressure. Experiments were also conducted for different heater-settings. The flow chart of the experimental procedure is shown in Fig.3.9. Late, it will be analysed that experimental uncertainty is dependent of interfacial pressure. Thus, experiments will continue until an interfacial pressure by which the experimental data is unstable.

3.8 Experimental results

3.8.1 Tools surface texture

Surface texture of the tools has an influence on the micro-deformation of the specimen. The tools used in experiment were manufactured under identical conditions. The surface texture of tools was verified to be similar. Surface texture measurements of the upper tool, transverse and parallel to the grinding direction, are shown in Figs. 3.10~3. 11 respectively.

3.8.2 Specimens surface texture measurement results

The surface textures of test specimens were measured prior to each test. Typical surface textures measurements after compression under different interfacial pressures are included in Appendix 3.4. The variation of surface roughness with interfacial pressure has a relationship to the surface texture of tools. The measured data enables the following conclusions which are also included in Appendix 3.4.

3.8.3 Thermal contact conductance

The experiments were conducted with all specimens listed in Table 3.1, following the procedure defined in Fig. 3.9. According to the experimental procedure (Fig.

3.9), six different initial surface textures (Table 3.1) were used for each of the applied interfacial pressure; six different interfacial pressure were applied to the specimens with each of the initial surface texture R_a scale (refer to Table 3.1). Therefore, the computed thermal contact conductance can be interpreted either as a function of surface roughness for a given interfacial pressure or as a function of the interfacial pressure for a given initial surface texture. The results of thermal contact conductance computed from these experiments are shown in Figs. 3.12~3.17, as a function of the surface roughness, and in Figs. 3.18~3.23, as a function of the interfacial pressure.

3.8.4 Repeated experiment results

For the assessment of the reliability, repeatability and uncertainties of the experiments, some of experiments were repeated, results for which are shown in Figs. 3.24~3.29.

3.9 Discussions

3.9.1 Experimental approach

All recorded temperatures were compensated according to the calibration results in Appendix 3.2. Regression analysis was used to determine the one-dimensional heat flow parameters by the method discussed in Appendix 3.1. Therefore, the temperatures on tools surface could be evaluated regardless the variation of the tool conductivity; further, the temperature drops across the thickness of the specimen, at each of the contact interfaces and the heat flux density could be computed. Thus, the equation (3-1) could be applied for the computation of thermal contact conductance. One-dimensional heat flow was achieved by the equipment compensation devices and the control parameters setting approach shown in Fig 3.8. The advantages of the equipment are that (1) specimen can be changed easily, (2) interfacial pressure can be reset and maintained by a hydro-mechanical system, and (3) interfacial temperatures are adjustable.

3.9.2 Resetting the experimental equipment according to environment

The approach has been mentioned in section 3.5.5.3, which is based on the comparison of experimental and FE simulation results.

Fig. 3.30 shows the temperature distributions by FE simulation and experiment. The critical portion of the graph is shown in Fig.3.31. FE can show the temperature drop at each interface; the experiment, however, can only extrapolate the tool surfaces temperatures. These have been analysed in section 3.5.1. The results in Figs. 3.30~3.31 show that the temperature distribution in the tools obtained from the experiment matches the temperature distribution obtained from FE simulation, the maximum difference being less than 0.1°C; transverse heat exchange between tools and frames (see Fig. 3.3) are negligible, and the heat transfer during contact can be considered one-dimensional. The difference of temperature between experiment and FE simulation is controlled within 0.1°C according to experience. The temperature field established is not perfectly steady state; due to dynamic reasons, slight temperature disturbance is inevitable; exact coinciding of results of FE simulation and experiment is unpractical. Occasionally, the comparison between measurements and FE simulation showed that the difference between measured and simulated temperatures was large, which may result form the different transverse heat exchange. Different transverse heat exchange requires a different setting of the control system, details of which are discussed in Appendix 3.5. This led to the experimental equipment resetting procedure shown in Fig. 3.8. In experiment practice, the heat flux density difference between upper- and lower tools was also controlled within 5%.

3.9.3 Design of experiments

Four types of experiments were designed. (1) Thirty-six specimens of Ma8 with different surface textures and thickness were prepared (see Table 3.1) for the purpose of experimentally investigating the influence of surface texture and interfacial pressure on thermal contact conductance. (2) Experiments with the same interfacial pressures were designed to assess the repeatability of the experiments. (3) Specimens were positioned between the two tools with different radial orientations. Thus, the

influence of the relative position of specimen to tools on the h-value can be investigated. The gap between insulators 6 and 15 (refer to Fig. 3.3) is determined by the thickness of specimen. Therefore, specimen thickness may influence the heat flow field being one-dimensional, and further influence the measurement accuracy. At the same time, computation of the interface temperature is related to the specimen material conductivity. –refer to equation (3-9). Accuracy of specimen conductivity will influence the computation of h-value. (4) Considering these factors, experiments using specimens with different thickness were also designed.

3.9.4 Surface texture of tools and surface deformation during contact

The surface texture of the tool is shown in Figs. 3.9~3.10. The measurements show that the surface texture of tools is not isotropic due to the method of production. The value was $(R_a)_p = 0.22\,\mu m$ parallel to the grinding direction and $(R_a)_t = 0.30\,\mu m$ transverse to the grinding direction. This surface roughness is much finer than that of the most test specimens; consequently, the surface roughness of the tools can be regarded as irrelevant to the analysis of results.

Three typical cases were analysed with a view to establishing the relationship between specimen surface texture, specimen surface deformation and tools surface texture. The phenomenon of the tool surface texture replication was observed, in particular, for the case when the initial specimen surface texture is close to that of the tool surface. For details please refer to Appendix 3.4.

3.9.5 Influence factors on thermal contact conductance

3.9.5.1 Surface roughness

In Figs. 3.12~3.17, the abscissa denotes specimen surface roughness before compression, and the ordinate denotes thermal contact conductance. It can be observed that thermal contact conductance varies with the surface roughness R_a under any given interfacial pressure; finer surface texture yields greater h-value. Figs. 3.12~3.16 show similar pattern in the relationship between h and surface roughness. Typically, the h-value of fine specimen ($R_a = 0.3 \sim 0.5\,\mu m$) is about 5

times greater than that of the coarse specimens ($R_a = 3 \sim 5\,\mu m$) with h-value from 10 to 150 $kWm^{-2}K^{-1}$, depending on the interfacial pressure and surface texture.

It is probably the ratio of real contact area to nominal contact area (area ratio thereafter) and the average distance between the two contact surfaces which determines the influence of surface roughness on h. It is widely recognised that larger area ratio results in greater h-value [4]. When in contact with a perfect flat plane, finer surfaces can provide a larger area ratio for a given nominal interfacial pressure. Besides, the average distance of the two contact surfaces (a rough surface and a perfectly flat surface) is the surface roughness of the rough surface [27]. Therefore, when contacting with a finer specimen, the mean distance between the two contact surfaces is less than with a rougher specimen. Larger area ratio and closer contact result in greater h-values.

However, area ratio is not a monotonously increasing function of surface roughness. Geometrically, it can be analysed that surfaces with the same roughness probably have different area ratios while under the same interfacial pressure. This may be one of the reasons why the h-values at any pressure and surface roughness may vary (Figs. 3.12~3.17).

3.9.5.2 Surface macro-irregularities

Although the specimen surfaces were prepared carefully, its contact with the elastic tool surface is not uniform. The non-uniform distribution of contact marks on the specimen surface can be observed. The area where the asperities are in contact with the tool surface is bright and more reflective; the area where there is no contact is dull, as a result of the EDM-machining operation. A conceptual diagram of contact between the tool and the specimen surfaces is shown in Fig. 3.32. This shows that some of the areas of the specimen surface are higher than others. Although the difference of the heights may be in the range of microns, the area is significant. This character of the texture is referred to as *surface macro-irregularities* and may result from flatness of surface [28-29]. Surface macro-irregularities are an important contributor to the h-value. The existence of surface macro-irregularities reduces the area ratio, and therefore, reduces the h-value.

Macro-irregularities may originate from random factors during the manufacturing operation and the accuracy of the electrode used in the EDM operation. Observation of specimen surface contact marks shows that the surface macro-irregularities of each specimen are different. Figs. 3.12~3.17 show that thermal contact conductance varies in a certain range at any given surface roughness. Macro-irregularities may be one of the contributors to this. It was observed that the variation of h-values at any given surface roughness is improved relatively when interfacial pressure increases or when the surface is coarse; the data in Fig. 3.15 is more concentrated than that in Fig. 3.12 relatively. This suggests that high interfacial pressures improve the surface contact as a result of surface deformation. Observation of variation of specimen surface contact marks supports this suggestion.

3.9.5.3 Thickness of specimen

Different specimen thickness changes the relative position of the two tools and the related components. This change of relative position may influence the heat-balance and the character of the heat flow. Although the resetting can be used to achieve the required heat-balance in different specimen thickness, thickness may have an influence on accuracy. Theoretically, value of h is a parameter which is dependant on contact conditions and contact materials, and irrelevant to the thickness of specimens. Experiments with specimens of different thickness can be used to assess the reliability of the experiment.

At the same time, the evaluation of interface temperature drop, as shown by equation (3-9), is related to the conductivity of specimen material. Experiments with specimens of different thickness were also used to verify the accuracy of the given specimen material conductivity.

The influence of the specimen thickness is not a random factor. It is difficult to obtain a trend in the variation of h with specimen thickness from results in Figs. 3.12~3.17. The h-value results under interfacial pressures of 30~180 MPa show that specimen thickness has no obvious influence. Thus the influence of specimen thickness on h-value can be neglected; specimens with thickness 1.0~4.0 mm are

suitable for the evaluation of thermal contact conductance in the experimental equipment. The influence of specimen thickness on the one-dimensional heat flow could be eliminated by appropriately resetting the experimental control parameters. On the other hand, from Fig. 3.17, thicker specimens have higher variance. Therefore, specimen thickness may influence the interfacial pressure that can be used in the experiments; or when interfacial pressure is high, specimen thickness may influence the accuracy of h-value. This has been analysed in Appendix 3.6.

3.9.5.4 Interfacial pressure

Thermal contact conductance was computed from experiments conducted under different interfacial pressures and surface textures. Thus, h can be also interpreted as a function of interfacial pressure for an initial surface texture. In Figs 3.18~3.23, the abscissa denotes the nominal interfacial pressure for the given initial surface texture and ordinate shows the corresponding h-value. The distribution suggests h varies almost linearly with interfacial pressure in the range 0~180 MPa, especially for those specimens with fine surface, as shown in Figs. 3.18~3.23. It is observed that low initial surface roughness values result in steeper gradients of the h-value. For example, the h-values of specimens with initial surface roughness $(R_a)_i = 0.25\sim0.35$ μm vary from 40 to 150 $kW/(m^2K)$ when the interfacial pressure increases from 0 to 180 MPa (Fig. 3.18), while the h-values of specimens with initial surface roughness $(R_a)_i = 3.51\sim4.97$ μm only vary from 7 to 40 $kW/(m^2K)$ for the same interfacial pressure range (Fig. 3.23). Surface texture, not only influences the current h-value, but also the trend. Increases in contact area ratio, as a function of surface texture and interfacial pressure, is the result of the deformation of surface asperities; finer surface textured specimens have larger area ratio for a particular value of interfacial pressure. Therefore, slope of the variation of h, as a function of interfacial pressure, should be a function of surface roughness.

It may also be observed that nonlinear variation of h-value also exists, in particular for those specimens with coarse surfaces. –refer to Figs. 3.21~3.23. One reason of nonlinearity of h-value is the surface macro-irregularities. If a surface is not in uniform contact, there would be a more rapid increase of the number of asperities

coming into contact as interfacial pressure increases. Interfacial pressure not only intensifies the contact area of individual asperity, but also increases the number of the contact asperities as well (refer to Figs. 3.32~3.33), which results in a more rapid increase of contact area ratio. A good example is the curve labelled A, shown in Fig. 3.19; the surface macro-irregularities of the corresponding specimen was confirmed by observation of contact marks distribution during the experimental programme. Therefore, macro-irregularities influence h-value much.

3.9.5.5 Asperity deformation character

Nonlinearity of the change in real contact area is not only determined by surface macro-irregularities, but also depends on the material properties and magnitude of the interfacial pressure. This nonlinearity of the real contact area which results from the nonlinearity of material property is a consequence of the character of the plastic deformation of asperities. The stress developing trend of contact between an asperity and a rigid plane is different from that of the macro contact between a billet and a rigid tool surface. A general form of asperity (refer to Chapter Four) is shown in Fig. 3.34a. This can be verified by the bearing-ratio-curves of all specimens surface texture measurements shown in Appendix 3.4. Due to this general form of asperity, from the initiation of contact, high local interfacial pressure and high plastic strain are induced in the contact asperity. Therefore, the plastic strain during mechanical contact of an individual asperity is always large. Since the plastic strain in the asperity is large, its constitutive relation can be approximately linearised at a strain, for example, the average asperity strain, as shown in Fig.3.34b. This analysis shows that the actual stress-strain curve of the asperity is nearly linear in the surface deformation. This surface deformation characteristic may have an influence on the relationship between the contact area ratio and nominal interfacial pressure. However, it is still difficult to quantitatively to define this influence.

It should be emphasised that the material property of asperity may be different from that of the substrate. Manufacturing process, in particular electrodischarge operation, may harden the asperity. This is why in Fig. 3.34b we specify it as a "assumed stress-strain relation".

3.9.6 Experimental uncertainties

3.9.6.1 Repeated experiments

Figs. 3.24~3.29 show the repeatability of the experiments. Uncertainties in the computation of the h-value were high as a consequence of unreliable measurements of interfacial pressures in excess of 300 MPa, as illustrated in Figs. 3.16~3.17. The thermocouple accuracy contributes to the overall uncertainty of the h-value when the interfacial pressure is high, or the surface texture is fine, or the both. Fig. 3.24a shows the repeatability of experiments under an interfacial pressure of 30 MPa; the overall maximum uncertainty of the h-value is of the order of 7%, as shown in Fig. 3.24b, where h_1 and h_2 show the h-values computed from two times experiments with the same experimental conditions. Repeatability of experiments under pressures 60, 120 and 180 MPa is also stable, with marginal increases in the uncertainty, of the order of 10%, as shown in Figs. 3.25~3.27. However, when the interfacial pressure is 300 MPa, the uncertainty increases significantly, as shown in Fig. 3.28. The main reason for this is that overall uncertainty of h-value is determined by the ratio of thermocouple accuracy to temperature drop (refer to Appendix 3.6). The temperature drop decreases rapidly with the increase of interfacial pressure, while the uncertainty of the thermocouple remains constant, which leads to the rapid increase of overall uncertainty of the h-value.

Tests under the same interfacial pressure on the same specimen with the same surface texture, but with different relative positions of tool surfaces, were conducted. One set of results is shown in Fig. 3.29. The computed values of h corresponding to four positions, 0°,90°,180° and 270°, were considered for the same interfacial pressure. Different orientations result in different h-values; the difference is larger than that in the repeated experiments (refer to Figs. 3.24~3.28). This may be the consequence of the flatness of the tool surfaces, the macro-irregularities of the specimen surface and parallelism between surfaces of tools. In order to minimise the influence of these, the relative position of each specimen to surfaces of tools were recorded and fixed in all experiments.

The repeated experiments show that the h-values computed from the experiments are reliable and repeatable up to an interfacial pressure of 180 MPa; the repeating uncertainty of the h-value is of the order of 10%.

3.9.6.2 Threshold level of the interfacial pressure and uncertainty of h-value

It is appeared that there is a limit to the interfacial pressure, beyond which, the computed h-value is unreliable. This can be illustrated by the results shown in Figs. 3.16~3.17. In Fig. 3.16, the variations of the computed h-values for the selected surface roughness under an interfacial pressure of 300 MPa, have become unexpectedly large, in particular for those of fine textured specimens. For an interfacial pressure of 420 MPa, the computed h-values appear to have a high variance, as shown in Fig. 3.17. This limit, referred to as threshold level of interfacial pressure, is determined by the initial specimen surface texture; fine initial surface texture of specimen decreases this limit. Experimental results in Fig. 3.17 show that the h-values of the coarse specimens ($R_a > 2.5\,\mu m$) are repeatable even under interfacial pressures of 420 MPa; the h-values of fine specimens are not consistent under an interfacial pressure of 300 MPa, as shown in Fig. 3.16. Theoretical analysis of the uncertainty of h-value has shown that the uncertainty of h-value is a function of interfacial pressure and the surface texture; this uncertainty is determined mainly by the thermocouple accuracy, the positioning of the thermocouples for the given surface texture and the interfacial pressure. These have been analysed in Appendix 3.6. Therefore, the threshold level of the interfacial pressure is defined by the specimen initial surface texture, the accuracy of the used thermocouples and the positioning of the thermocouples. Theoretical analysis was conducted with a view to defining the uncertainty of h-value, the threshold level and the optimal positioning of the thermocouples for minimisation of the uncertainty of the h-value. These are discussed in Appendix 3.6.

3.10 Further considerations

Specimen preparation is important for this experiment. Surface macro-irregularities are formed during this preparation. It is still not sure if macro-irregularities are related to the thickness of specimens. Interfacial pressure range for successful

experiments is still confined between 30~180 MPa; it is far less than the pressure activated on the billet/tool interface in cold forging; there is a long way to go for valid h-value data applicable to precision cold forging. The presented improvement approach for the experimental equipment is waiting for validation. Therefore, more experimental research efforts are required.

3.11 Conclusions

The experiment results and the discussions lead to the following conclusions:

1) Thermal contact conductance is a function of surface texture. Value of h increases with the improvement of surface roughness, regardless of whether this improvement is the consequence of surface pressure. Typically, the value changes from $h = 10 kWm^{-2}K^{-1}$ to $h = 150 kWm^{-2}K^{-1}$ for changes in surface texture from $R_a = 0.4\,\mu m$ to $R_a = 4\,\mu m$, depending on the interfacial pressure; the h-value of fine specimens ($R_a = 0.4\,\mu m$) is about 5 times of that of the coarse specimen ($R_a = 4\,\mu m$) at any interfacial pressure.

2) Thermal contact conductance increases almost linearly with interfacial pressure up to an interfacial pressure of 180 MPa for the specified contact materials. For fine specimens (R_a) = 0.25 ~ 0.35 μm, the h-value varies linearly from 30~150 ($kWm^{-2}K^{-1}$) for the interfacial pressure range 30~180 MPa, while for coarse specimens ($R_a = 3.51 \sim 4.97\,\mu m$), the variation of the h-value is 7~40 ($kWm^{-2}K^{-1}$) for the same range of interfacial pressure.

3) There is a threshold of interfacial pressure for the evaluation of h-value by the steady temperature based method; this threshold of the interfacial pressure is defined by initial surface texture, accuracy and positioning of thermocouples. Coarse specimens, more accurate thermocouples and optimal positioning of thermocouples can raise this threshold. Using the current experimental equipment, the threshold is about 180 MPa for specimens with specified mean initial surface textures. Both, the experimental results and analysis support this.

4) A technique, combined with EF simulation of the heat transfer during tests, has been developed for the rapid setting of the experimental equipment to ensure a one-dimensional heat flow field.

5) Uncertainty of computation of the h-value is nearly proportional to the value of h; therefore, high interfacial pressure, fine specimen surface, or the both result in large h-value uncertainty.

6) An optimal positioning of thermocouples on the tools for achieving the best computational accuracy of thermal contact conductance, or the highest interfacial pressure threshold, was developed.

3.12 References

1. C. W. Vigor, et al., A Thermocouple for Measurement of Temperature Transients in Forging Dies, Temperature, Its Measurement And Control Vol. 3, part 2, Reinhold, New York, 1961, pp. 625-630
2. S. Shamasundar, et al., Numerical and Experimental Study of The Thermal Behavior of Coining And Upsetting Processes, Journal of Materials Processing Technology, 1993. Vol. 36, No. 2, pp. 199-221
3. T. Aikawa and W. O. Winer, Thermal Contact Conductance Across Si_3N_4-Si_3N_4 Contact, Wear, Vol. 177, pp. 25-32, 1994
4. M. A. Lambert and L. S. Fletcher, Experimental Investigation of The Thermal Contact Conductance of Electroplated Silver Coatings, Journal of Thermophysics And Heat Transfer, 1995, Vol. 9, No. 1, pp. 79-87
5. K. C. Chung and J. W. Sheffield, Enhancement of Thermal Contact Conductance of Coated Junctions, Journal of Thermophysics And Heat Transfer, 1995, Vol. 9, No. 2, pp. 329-334
6. K. C. Chung, Effect of Surface Deformations on Thermal Contact Conductance of Coated Junctions, Journal of Thermophysics And Heat Transfer, 1995, Vol. 9, No. 4, pp. 681-685

7. S. K. Parihar and N. T. Wright, Thermal Contact Resistance at Elastomer to Metal Interface, International Journal of Heat And Mass Transfer, 1997, Vol. 24, No. 8, pp. 1083-1092
8. D. G. Blanchard and L. S. Fletcher, Contact Conductance of Selected Metal-Matrix Composites, Journal of Thermophysics And Heat Transfer, 1995, Vol. 9, No. 3, pp. 391-396
9. K. E. Parmenter and E. Marschall, Influence of Surface Preparation on Thermal Contact Conductance of Stainless Steel And Aluminium, Experimental Heat Transfer, 1995, Vol. 8, pp. 195-208
10. E. E. Marotta and L. S. Fletcher, Thermal Contact Conductance for Aluminium And Stainless-Steel Contacts, Journal of Thermophysics And Heat Transfer, 1998, Vol.12, No. 3, pp. 374-381
11. E. E. Marotta and L. S. Fletcher, Thermal Contact Conductance of Selected Polymeric Materials, Journal of Thermophysics And Heat Transfer, 1996, Vol. 10, No. 2, pp. 334-342
12. M. Williamson and A. Majumdar, Effect of Surface Deformation on Contact Conductance, Journal of Heat Transfer, Transactions of The ASME, 1992, Vol. 114, pp. 802-810
13. Z. M. Hu, J. W. Brooks and T. A. Dean, The Interfacial Heat Transfer Coefficient in Hot Die Forging of Titanium Alloy, Proceedings of The Institution of Mechanical Engineers, Vol. 212, No. C, pp. 485-496, 1998
14. M. A. Kellow, A. N. Bramley and F. K. Bannister, The Measurement of Temperatures in Forging Dies, International Journal of Machine Tool Design And Research, Vol. 9, pp. 239-260, 1969
15. G. Beck, The Temperature Occurring During The Upset Forging & Moulding of Cylindrical Samples of Steel, Schmeidetechnische Mitteilangen, 1958, Vol. 5, pp. 561
16. C. W. Vigor and J. R. Jr. Hornaday, A Thermocouple for Measurement of Temperature Transients in Forging Dies, Temperature, Its Measurement And Control in Science And Industry, Vol. 3, Reinhold 1961

17. T. A. Dean and T. M. Silva, Die Temperatures During Production Drop Forging, Journal of Engineering for Industry, Transactions of The ASME, Vol. 101, 1979, pp. 385-390
18. P. G. Stevens, K. P. Ivens and P. Harper, Increasing Work-Roll Life by Improved Roll-Cooling Practice, Journal of The Iron And Steel Institute, 1971, pp. 1-11
19. S. L. Semiatin, et al., Determination of The Interface Heat Transfer Coefficient for Non-Isothermal Bulk-Forming Process, Journal of Engineering for Industry, Transactions of The ASME, 1986, Vol. 109, pp. 49-57
20. J. G. Lenard and M. E. Davies, The Distribution of Temperatures in A Hot/Cold Die Set: The Effect of The Pressure, Temperature And Material, Journal of Engineering Materials And Technology, Transactions of The ASME,1995, Vol. 117, pp. 220-227
21. P. R. Brute, et al, Measurement And Analysis of Heat Transfer And Friction During Hot Forging, Journal of Engineering for Industry, Transactions of The ASME, 1990, Vol. 112, pp. 332-339
22. W. Nshama and J. Jeswiet, Evaluation of Temperature And Heat Transfer Conditions at The Metal-Forming Interface, Annals of The CIRP, 1995, Vol. 44, pp. 201-204
23. P. Dadras and W. R. Wells, Heat Transfer Aspects of Non-Isothermal Axisymmetric Upset Forging, Journal of Engineering for Industry, Transactions of The ASME, Vol. 106, 1984, pp. 187-195
24. W. Nshama, J. Jeswiet and P. H. Oosthuizen, Evaluation of Temperature And Heat Transfer Conditons at The Metal Forming Interface, Journal of Materials Processing Technology, Vol. 45, pp. 636-642, 1994
25. Z. Malinowski, et al., A Study of The Heat-Transfer Coefficient As A Function of Temperature And Pressure, Journal of Materials Processing Technology, 1994, Vol. 41, pp. 125-142
26. W. S. Janna, Engineering Heat Transfer, Boston, Mass. :PWS Engineering, c1986
27. D. J. Whitehouse, Handbook of Surface Metrology, Bristol, Institute of Physical Publishing, c1994
28. B. B. Mikic, Thermal Contact Conductance; Theoretical Considerations, International Journal of Heat And Mass Transfer, Vol. 17, 1974, pp. 205-214

29. K. Nishino, et al., Thermal Contact Conductance Under Low Applied Load in A Vacuum Environment, Experimental Thermal And Fluid Science, 1995, Vol. 10, pp.258-271
30. J. Wheeler and A. R. Ganji, Introduction to Engineering Experimentation, 1996, Prentice Hall, New Jersey, pp. 159-183
31. S. J. Kline and F. A. McClintock, Describing Uncertainties in Single-Sample Experiments, Mechanical Engineering, Vol. 75, No. 1, 1953, pp. 3-8
32. ANSI/ASME, Test uncertainty, ASME PTC 19.1-1998

Appendix 3.1

Data-Processing with Variable Tool Material Thermal Conductivity

Formula (3-10) may be defined generally as

$$k_t = k_t(T) \tag{3.1-1}$$

The NPL data is of the form:

$$k_t = k_{t0} + k_{t1}T + k_{t2}T^2 \tag{3.1-2}$$

During experiments, a constant heat flux should be achieved. Thus, if the temperature is uniformly distributed across the cross-section, the heat flux density can be considered constant along the tool axis. From equations (3-4) and (3.1-1), it can be shown that

$$q = k_t(T)\frac{dT}{dz}$$

or

$$\frac{dT}{dz} = \frac{q}{k_t(T)} \tag{3.1-3}$$

Equation (3.1-3) suggests that if the thermal conductivity of the tool material is not constant, the temperature gradient, based on the constant heat flux density q, may not be constant; therefore, the temperature distribution along the tool axis may not be linear, either. Integrating equation (3.1-3),

$$\int k_t(T)dT = qz + C \tag{3.1-4}$$

from which

$$T = \frac{qz + C}{\int k_t(T)dT/T} \tag{3.1-5}$$

The temperature distribution depends on the value of the constants q and C. Equation (3.1-4) shows that if the tool thermal conductivity is not constant, the prevailing one-dimensional temperature field is different from that defined by equation (3-5). It is usually difficult to find an explicit function $T(z)$ due to the variation in tool conductivity. Thus, the following numerical technique for processing the data was developed. Let

$$\bar{k}_t(T) = \int k_t(T)dT/T \tag{3.1-6}$$

and a function S is defined as the sum of squares of temperature difference:

$$S = \sum (T_{iex} - T_{ian})^2 \tag{3.1-7}$$

Both C and q can be determined by the minimisation of S. Let

$$\begin{aligned} \frac{\partial S}{\partial q} &= 2\sum (T_{iex} - T_{ian})\frac{\partial T_{ian}}{\partial q} = 0 \\ \frac{\partial S}{\partial C} &= 2\sum (T_{iex} - T_{ian})\frac{\partial T_{ian}}{\partial C} = 0 \end{aligned} \tag{3.1-8}$$

From equation (3.1-4),

$$\begin{aligned} \frac{\partial T_{ian}}{\partial q} &= \frac{z_i}{k_t(T_{ian})} \\ \frac{\partial T_{ian}}{\partial C} &= \frac{1}{k_t(T_{ian})} \end{aligned} \tag{3.1-9}$$

Substituting equations (3.1-5), (3.1-6) and (3.1-9) into (3.1-8), the following non-linear simultaneous equations can be obtained:

$$\begin{aligned} \sum \left(\frac{qz_i + C}{\bar{k}_t(T_{ian})} - T_{iex} \right) \frac{z_i}{k_t(T_{ian})} &= 0 \\ \sum \left(\frac{qz_i + C}{\bar{k}_t(T_{ian})} - T_{iex} \right) \frac{1}{k_t(T_{ian})} &= 0 \end{aligned} \tag{3.1-10}$$

where $\bar{k}_t$ is defined by equation (3.1-6). Theoretically, two equations are sufficient to determine the magnitude of the two parameters, C and q, which will enable the minimisation of equation (3.1-7). However, whether the analytical solutions of q and C are obtainable depends mainly on the expression of temperature T in

equation (3.1-4) or (3.1-5). If temperature T can be expressed as a constant, q and C can be analytical obtained. For example, if heat conductivity k_t is constant with respect to temperature T, the solution of equation (3.1-10) provides the conventional result:

$$q = k_t \cdot \frac{\sum T_{iex} \cdot \sum z_i - n\sum T_{iex} z_i}{\left(\sum z_i\right)^2 - n\sum z_i^2} \tag{3.1-11}$$

According to NPL data, conductivity k_t is expressed as a polynomial function of T. In this case, the analytical solution of equation (3.1-10) cannot be obtained because equation (3.1-5) fails to provide an explicit solution of T as a function of z. A numerical iterative approach for obtaining q and C is thus required. In equation (3.1-10), by assuming T_{iex} as the initial value of T_{ian}, i.e., let $T_{ian}^{(J)} = T_{ian}^{(0)} = T_{iex}$, linear simultaneous equations are obtained from equation (3.1-10) with a solution

$$q^{(J)} = \frac{\sum \frac{T_{iex}}{k_t(T_{ian}^{(J)})} \sum \frac{z_i}{\bar{k}_t(T_{ian}^{(J)}) k(T_{ian}^{(J)})} - \sum \frac{T_{iex} z_i}{k(T_{ian}^{(J)})} \sum \frac{1}{\bar{k}_t(T_{ian}^{(J)})(T_{ian}^{(J)})}}{\left(\sum \frac{z_i}{\bar{k}_t(T_{ian}^{(J)}) k_t(T_{ian}^{(J)})}\right)^2 - \sum \frac{z_i^2}{\bar{k}_t(T_{ian}^{(J)}) k_t(T_{ian}^{(J)})} \sum \frac{1}{\bar{k}_t(T_{ian}^{(J)}) k_t(T_{ian}^{(J)})}} \tag{3.1-12}$$

and

$$C^{(J)} = \frac{\sum \frac{T_{iex}}{k_t(T_{ian}^{(J)})} - q^{(J)} \sum \frac{z_i}{\bar{k}_t(T_{ian}^{(J)}) k_t(T_{ian}^{(J)})}}{\sum \frac{1}{\bar{k}_t(T_{ian}^{(J)}) k_t(T_{ian}^{(J)})}} \tag{3.1-13}$$

Substituting equations (3.1-12) and (3.1-13) into equation (3.1-4) to obtain a revised $T_{ian}^{(J+1)}$ under $q^{(J)}$ and $C^{(J)}$, and replacing $T_{ian}^{(J)}$ in equations (3.1-12) and (3.1-13) by $T_{ian}^{(J+1)}$ leads to a further $q^{(J+1)}$ and $C^{(J+1)}$. If both

$$\begin{aligned} \left|q^{(J)} - q^{(J+1)}\right| &< \varepsilon_1 \\ \left|C^{(J)} - C^{(J+1)}\right| &< \varepsilon_2 \end{aligned} \tag{3.1-14}$$

$q^{(J+1)}$ and $C^{(J+1)}$ can be regarded as the required constants C and q which can enable the minimisation of the value of S. The above iteration process is repeated till equation (3.1-14) is satisfied. It should be noted that when revised $q^{(J)}$ and $C^{(J)}$ are obtained from equations (3.1-12) and (3.1-13), the analytical result of revised $T_{ian}^{(J+1)}$ expressed by equation (3.1-4) remains analytically unobtainable. However, $T_{ian}^{(J)}$ is a

close approximation of the initial value of $T_{ian}^{(J+1)}$, thus the Newton Iteration can be used to obtain $T_{ian}^{(J+1)}$. The flowchart for this iterative process is shown in Fig.3.1.1.

Mathematically, if the values of both q and C satisfy equation (3.1-14), it can be established from the iterative process, that q, C and $T_{ian}^{(J)}$ will satisfy equations (3.1-4), (3.1-12) and (3.1-13), then (3.1-10), and finally (3.1-8); therefore, q, C and $T_{ian}^{(J)}$ will enable the minimisation of the sum of squares in equation (3.1-7). In particular, Consider $k_t(T) = k_0$ in equation (3.1-1), from which $k_t(T) = k_0$. Substituting both $k_t(T) = k_0$ and $\bar{k}_t(T) = k_0$ into equation (3.1-12) results in

$$q = k_0 \frac{\sum T_{iex} \sum z_i - n \sum T_{iex} z_i}{\left(\sum z_i\right)^2 - n \sum z_i^2} \qquad (3.1\text{-}15)$$

Comparing equation (3.1-15) and (3.1-11), it can be shown that the approach discussed is of general significance; constant heat conductivity of the tool material can be considered as a particular case of this approach.

When the constants C and q are determined, the tools surface temperatures can be extrapolated; further, the temperature drop $\Delta T_{s,f}$ defined by equation (3-9), and the thermal contact conductance h defined by equation (3-1), are obtainable. In this way, the variation of tool material conductivity in the computation of h-value is accounted for.

Appendix 3.2

Calibration of Thermocouples

A3.2.1 Calibration approach

The approach for the calibration of thermocouples is shown in Fig. 3.2.1. The instrument (1) is an INFT1000 temperature reference, calibrated by the manufacturer to an accuracy higher than $\pm 0.1^{\circ}C$. The junctions of eight thermocouples (5), which

would be used in the experimental equipment, were fixed together with the individually calibrated thermocouple junction (2), and placed in a tank (6) filled with oil (7). All thermocouples would be exposed to the same temperature in the oil tank. The signal of the calibrated standard thermocouple was transmitted to the INFT1000 Calibrator (1), which displayed the temperature of the oil at the thermocouple location. The temperature of all other thermocouples were transmitted to the data acquisition system (4), which would be used in the experimental equipment, as shown in Fig. 3.3~3.4. A computer-based monitor (3) of the system enabled the display of the temperatures recorded by all thermocouples. By comparing the temperatures displayed by the temperature reference INFT1000 and by the computer monitor system used in the experiment, the combination of all thermocouples and the data acquisition system, can be calibrated.

The adjustable electric heater (8) under tank (6) was used as a heat source; oil temperature varied in the range of 30~150 $^{\circ}C$. For the sake of safety, a special type of oil which can be subjected to a temperature range $-20\ ^{\circ}C \sim 288\ ^{\circ}C$ was used. In calibration process, it was required that the oil is heated as slow as possible to make sure the temperature filed in the oil tank as uniform as possible.

A3.2.2 Calibration results

Considering that each thermocouple was only used in a specified range of temperature, the calibration was conducted only for this specified range. By comparing the readings of the reference thermocouple and those used in the experimental equipment, the required compensation can be imposed. The calibration results of the upper and lower tool thermocouples are shown in Figs. 3.2.2~3.2.3 respectively. The required compensation temperature value is expressed as the linear function of the measured temperature. For example, for the upper-most thermocouple, the compensation temperature ΔT_c can be defined by

$$\Delta T_c = -1.40 + 1.74 \times 10^{-2} T\ ^{\circ}C \qquad (3.2\text{-}1)$$

The standard deviation for all thermocouples by regression analysis is between $\pm 0.010 \sim 0.056\ ^{\circ}C$. Therefore, the accuracy of thermocouples after compensation

has a maximum value of ± 0.06 °C. Considering the accuracy of the temperature reference is $\pm 0.1^{\circ}C$, the accuracy of the used thermocouples can be considered to be better than $\pm 0.1^{\circ}C$. The results confirm that the uncertainty of the K-type thermocouples is mainly systematic.

Appendix 3.3

Experimental Data Recording Sheet

Table 3.2 Experimental records and data processing

Date:	30/10/99	**Specimen number:**	2.0-C-30
Tools:		**Specimen material:**	
Upper tool material: N910		Material*	Ma8
$k_{rr} = 19.21 + 1.43\times10^{-2}T + 1.05\times10^{-6}T^2\ (W\,m^{-1}K^{-1})$		Conductiviy (K_m)	60 (W m^{-1} K^{-1})
		Thickness (t)	2 (mm)
Lower tool material: N910		Roughness** (R_a)	0.74 (μm)
$k_{rr} = 19.21 + 1.43\times10^{-2}T + 1.05\times10^{-6}T^2\ (W\,m^{-1}K^{-1})$		Preload (P_l)	0 (kN)

Experiment parameters:			Analysis			
	Setting	Reading	x	T_{exp}	T_{fit}	$T_{exp}-T_{fit}$
	(°C)	(°C)	35	145.13	145.22	-0.09
			25	130.41	130.28	0.13
Main heater (H_m)	200	200	15	115.23	115.35	-0.12
Upper compensating heater (H_{uc})	-39	-(39.7~38.5)	5	100.34	100.26	0.08
Lower compensating heater (H_{lc})	0	2.-5.5	0	0	92.65	
Inner cooler (C_i)	10	10	-2	0	89.46	
Out cooler (C_o)	10	10	-6.954	82.12	82.16	-0.04
Contact pressure (p_t)	32.87	(MPa)	-16.964	66.77	66.71	-0.06
Interface condition		dry	-26.95	51.32	51.3	0.02
			-36.936	35.86	35.89	-0.030

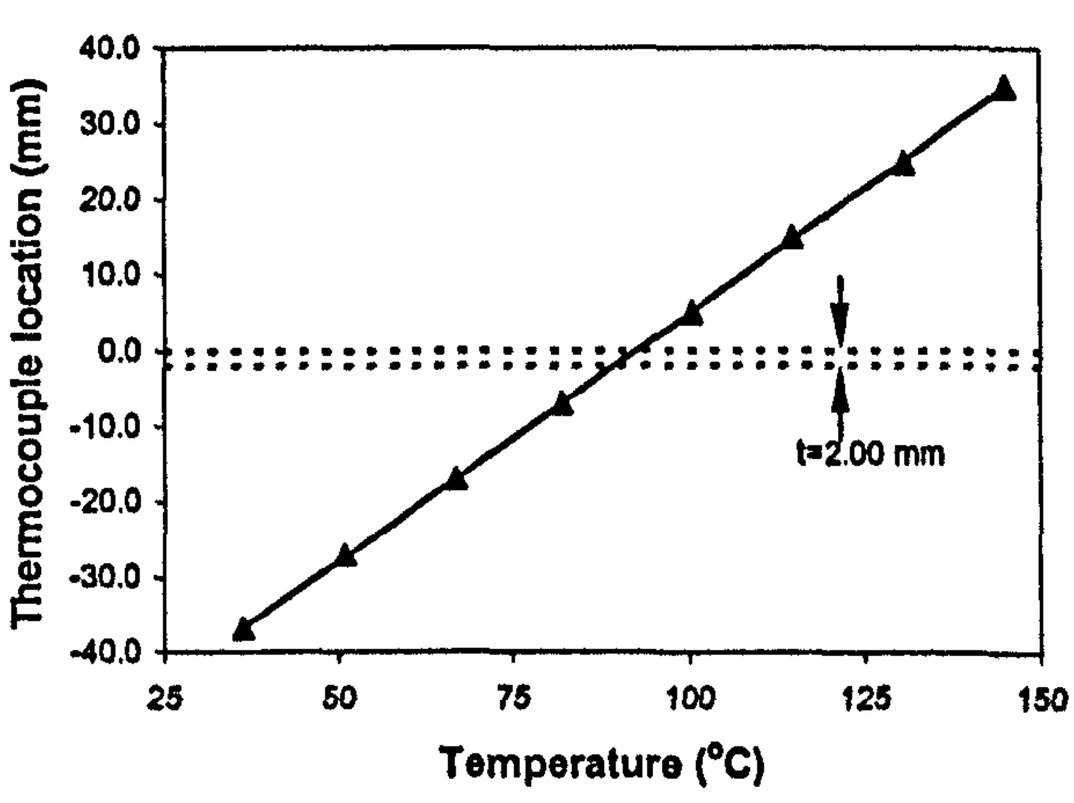

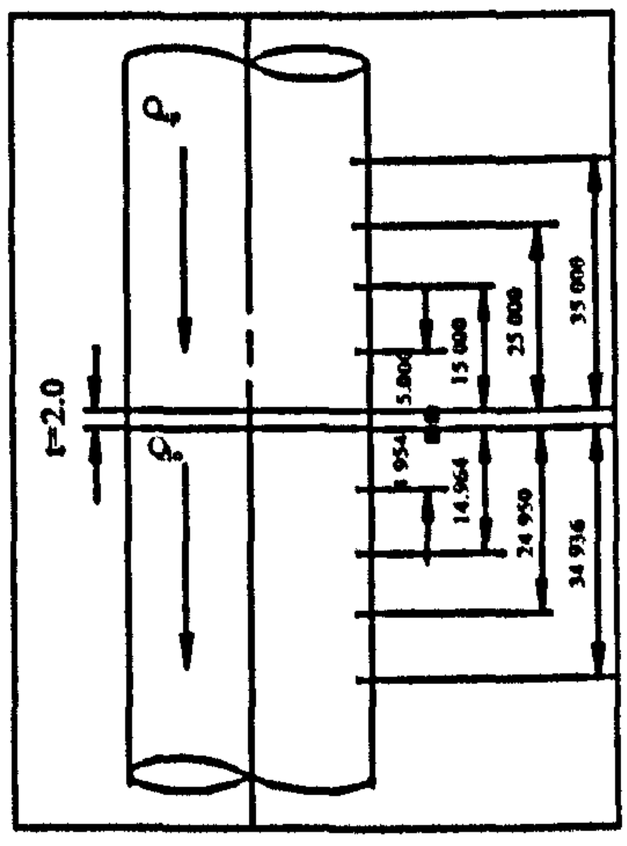

Results

Iterm	Units	Value	
Correlation coefficients r_{up}, r_{lo}		0.99	0.99
Heat flux density q_{up}, q_{lo}	(kWm^{-2})	31.33	30.82
Temperature drop ΔT	°C	1.08	
Contact conductance h	($kWm^{-2}K^{-1}$)	28.83	
Difference of heat flux δ_{flux}	%	1.62	

Appendix 3.4

Specimens Surface Texture Measurement Results and Some Conclusions

Figs. 3.4.1~3.4.7 show the surface texture measurement results of some typical specimens. Some of these are the initial surface textures while others are the textures after compression under different interfacial pressures. Considering the surface textures of the tools (Figs. 3.10~3.11) and the interfacial pressures, the following conclusions may be drawn.

- When the roughness of the specimen surface is much greater than that of the tools, the roughness of the specimen reduces with interfacial pressure. Evidence of this was provided during tests with rough specimens. Typical surface deformation is shown in Figs. 3.4.1~3.4.2; Fig. 3.4.1 shows surface specifications of specimen 4.0-E-000 (refer to Table 3.1) before compression, while Fig. 3.4.2 shows the specification after being subjected to a pressure of 420 MPa by the tools. From Figs. 3.4.1~3.4.2, it is apparent that interfacial pressure micro-deforms the surface.

- If surface roughness of specimen is less than or equal to that of the tools, increase in the interfacial pressure does not improve the surface roughness of the specimen further, regardless of interfacial pressure; the surface of the specimen remains at a value approximately equal to that of the tools. Fine textured specimens, initial $R_a \leq 0.5\ \mu m$, remain unchanged or nearly unchanged under tool pressure. Typical cases are shown in Fig. 3.4.3 and Fig. 3.4.4. The difference between the "before and after" compression textures is small; all surface parameters, including the bearing ratio curve, changed marginally after compression, even under interfacial pressures of 420 MPa.

- As interfacial pressures are sufficiently increased, the surface texture of specimen corresponds to that of the tool regardless of initial surface texture; the texture of

the hardened tool surface is replicated on the specimen surface. Figs. 3.4.5~3.4.7 illustrate this process. Fig. 3.4.5 shows the surface profile and texture of specimen 2.5-C-000 before compression. Fig. 3.4.6 shows the surface profile and texture of the same specimen after compression under an interfacial pressure of 180 MPa. The surface profile and bearing ratio curve in Fig. 3.4.6 show plastic deformation of the specimen surface; the peaks appear to have been particularly deformed (Fig. 3.4.6). However, this character is modified when the compression is increased. –refer to Fig. 3.4.7. The texture shown in Fig. 3.4.7 is similar to that of tools shown in Figs. 3.10~3.11. This suggests that the replication of the tool texture is a demonstrable phenomenon.

- The above mentioned texture replication has to be identified clearly since it may conceal the relationship between surface texture and interfacial pressure.

Appendix 3.5

Experimental Equipment Setting Approach

A3.5.1 Equivalence of constant heat flux and temperature field

Heat flux density across the tool cross-section is assumed to be uniform. Therefore, the constant heat flux condition can be replaced by the equivalent constant heat flux density condition. In practice, both, the temperature difference and the heat flux density difference, are chosen as the criterion to assess whether the heat flow field in the tools is one-dimensional. In fact, the two approaches are equivalent. Mathematically, if heat flux densities in both tools are equal and constant, transverse heat exchange does not occur; the heat flow field is, therefore, one-dimensional. If the heat flow is one-dimensional, transverse heat exchange does not occur; therefore, the heat flux densities in the two tools are constant and equal.

Assuming that a steady one-dimensional temperature field $\overline{AFEDCB}$, as shown in Fig. 3.5.1, was modelled by FE simulation, the heat flux density in part field $\overline{AF}$

should be equal to that of $\overline{CB}$ (constant heat flux density condition). Consider that $\overline{AF_1E_1D_1C_1B}$ is the corresponding experimental temperature field. If both temperature-fields, $\overline{AFEDCB}$ and $\overline{AF_1E_1D_1C_1B}$, are identical, the heat flux density in both tools will be equal, and remain the same as that of the FE simulation. On the other hand, if heat flux density is identical and constant for both tools, the heat flow fields should be one-dimensional and therefore, identical. This analysis shows that if the FE simulation, using the experimental conditions, predicts a one-dimensional heat flow field different from that of the experiment, the experimental heat flow field may not be one-dimensional; therefore, the control parameters need to be reset. By using temperature difference as the criterion, it would be easy to determine which of the control parameters is critical for control. If heat flux density is selected as the criterion, regression analysis will be sufficient to establish the parameter which is critical for the control.

A3.5.2 Re-setting of the experiment equipment

The following text refers to the approach for setting the control parameters to establish a one-dimensional steady heat transfer field. Four possible transverse heat exchange cases, as shown in Fig. 3.5.2, were considered. The first case is for the transfer of heat to both upper and lower tools from the environment; the second is the reverse case. Alternative heat transfer situations are also considered. In the first case, due to the heat transfer to the tools, the temperature measured at the location of a thermocouple will be higher than that achieved during one-dimensional heat flow. But the temperature of up-most thermocouple will not change much due to close to the main heater, and the temperature of lowest thermocouple also will not change much due to close to the heat sink. This will result in a temperature field $\overline{AF_1E_1D_1C_1B}$ (Fig. 3.5.1) which is higher than that predicted by FE. The actual one-dimensional temperature field, if without the transverse heat flow, may be $\overline{GH}$. Neither the measured nor the predicted value may be correct due to the h-value and temperature boundary conditions used in FE simulation (refer to section 3.5.4). Because of the additional heat from outside, the heat flux will continue to increase. In other words, the slope of $\overline{BC_1}$ is larger than that of $\overline{AF_1}$, therefore,

$$q_{t\nabla} > q_{t\Delta} \tag{3.5-1}$$

or $$T_{ex} > T_{FE} \tag{3.5-2}$$

Similarly, if heat is lost from both tools, the temperature field measured should be lower than that predicted by FE simulation, as shown in Fig. 3.5.3. In this case,

$$q_{t\Delta} > q_{t\nabla} \tag{3.5-3}$$

or $$T_{ex} < T_{FE} \tag{3.5-4}$$w

When the comparison between experimental and FE simulation satisfies inequality (3.5-1) or (3.5-2), the control temperatures of the lower compensation heater, upper compensation heater and outer cooler should be lowered (refer to Fig. 3.4); if these satisfy the inequality (3.5-3) or (3.5-4), the control parameters should be raised.

It is more difficult to achieve a balanced equilibrium condition for the cases three and four, as shown in Fig. 3.5.2c and Fig. 3.5.2d. If the upper tool absorbs heat and the lower tool releases heat during the experiment, the comparison between experimental and FE simulation results would be as shown in Fig. 3.5.1. Due to the absorption of heat, temperature of the upper-most thermocouple, T_A, is higher than T_H. For the same reason, slope of $\overline{AF_1}$ is lower than it should be. At the lower tool, due to loss of heat, the temperature of the lower-most thermocouple, T_B, may be higher, lower or even equal to T_G. The slope of $\overline{C_1B}$ is, therefore, greater than that of $\overline{AF_1}$ due to the loss of heat transversely in the lower tool. Thus, the relationship between temperature and heat flux density will be as defined in inequalities (3.5-1) and (3.5-2). However, in this case, the difference in heat flux density is relatively greater than that of the case shown in Fig. 3.5.2a. Similar analysis of case four shown in Fig. 3.5.2d and the relationship between heat flux density and temperature result in inequalities (3.5-3) or (3.5-4). However, in this case, the difference of heat flux density is relatively greater than that of case shown in Fig. 3.5.2b.

From above analysis there are only three possible consequences of the comparison between experimental and FE simulation results. (1) The difference between heat flux densities in upper and lower tools, or the temperature difference between

experiment and FE simulation results is small, the consequence being that the heat flux density can be considered constant and equal. (2) Heat flux density of the upper tool is greater than that of the lower tool and the temperature in the experiment is lower than that predicted by FE simulation. (3) Heat flux density of the upper tool is smaller than that of the lower tool and the temperature in the experiment is higher than that predicted by FE simulation. The first situation shows a successful test; the second and the third require the resetting of the control system.

Summarising above analysis, the general re-setting approach is shown in Fig. 3.8 as a flow chart. 15% percent of difference of heat flux density is used as a reference to define the transverse heat exchange pattern (refer to Fig. 3.5.2) based on experience. In practice, the most possible cases are the first and second in Fig. 3.5.2 and the third and fourth cases rarely occur.

Appendix 3.6

Analysis of Thermal Contact Conductance Uncertainties

A3.6.1 Uncertainty factors

The overall uncertainty of the computed h-value is the cumulation of uncertainties incurred in the following:

- thermocouple readings,
- thermocouple locations,
- tool conductivity,
- specimen conductivity and dimensions.

These factors contribute to the overall uncertainty in the specification of h-value. The contribution of these factors, whether random or systematic, varies with the interfacial pressure and surface texture. These factors are rarely referred to [5,7,9-11,29].

The experimental equipment was fitted with K-type thermocouples; these have nickel-chromium junctions and have an accuracy of $\pm 1.5\,^{\circ}C$. However, each thermocouple can be calibrated individually to provide temperature measurement to an accuracy of $\pm 0.1\,^{o}C$.

Theoretically, it can be shown that the accuracy of the computed h-value is approximately proportional to the ratio of thermocouple accuracy δT_0 (=constant) to the temperature drop ΔT at the interface. The temperature drop is a parameter that is sensitive to both interfacial pressure and surface texture. Therefore, the accuracy of h-value is a function of contact parameters, instead of a constant as indicated by previous research [5,7,9-11,29]. When interfacial pressure is high or specimen surface texture is fine, or the both, the temperature drop may be of the order of 0.1°C or even lower. In this case, the ratio of thermocouple accuracy δT_0 to the temperature drop ΔT_{stf} will have a relatively high value, resulting in unreliable experimental conditions.

A3.6.2 Analysis of h-value uncertainty

Temperature measurements are taken on the assumption that a steady one-dimensional temperature field prevails. Even if the controlling parameters are correct, it takes a long time to establish a steady-static field. The measurements that lead to the computation of h-value are typical of a single-sample experiment; it would be costly to repeat the measurements to statistically obtain the uncertainty of the measurements. Wheeler [30] and Kline [31] presented an analysis of the determination of uncertainty of such experiments by a single-sample experiment uncertainty analysis. The relevant theory is shown in Appendix 3.6.1

Obviously, the factors that cause uncertainty of h-value can be considered independent of each other, theoretically. The h-value is computed from

$$h = \frac{q}{\Delta T_{stf}}$$

It is unclear whether the temperature drop, ΔT_{sff}, and heat flux density, q, are independent of each other. (For the sake of brevity, in the following text, temperature drop on tool/specimen interface is noted by ΔT). Thus from equation (3.6.1-2)

$$\left|\frac{\delta h}{h}\right| = \left[\left(\frac{\delta q}{q}\right)^2 + 2\frac{1}{q}\frac{1}{\Delta T}\delta(q,\Delta T) + \left(\frac{\delta \Delta T}{\Delta T}\right)^2\right]^{\frac{1}{2}}$$

where $\delta(q,\Delta T)$ is the covariance estimation of uncertainties of q and ΔT. It can be shown, from statistics, that $\delta(q,\Delta T) \le \delta q \cdot \delta \Delta T$, therefore,

$$\left|\frac{\delta h}{h}\right| \le \left|\frac{\delta q}{q}\right| + \left|\frac{\delta \Delta T}{\Delta T}\right| \qquad (3.6\text{-}1)$$

Simultaneously, the heat flux q is approximately a large constant in the experiments compared to the temperature drop ΔT for different contact conditions, mathematically. q varies in a range of 30~33 $\left(kW\,m^{-2}\right)$ for different contact conditions, (refer to Appendix 3.3). Later, it will be shown that δq is a physical value, the mathematical amount of which is comparable to that of $\delta(\Delta T)$, therefore, $\frac{\delta q}{q} << \frac{\delta \Delta T}{\Delta T}$. Thus,

$$\left|\frac{\delta h}{h}\right| \approx \left|\frac{\delta \Delta T}{\Delta T}\right| \qquad (3.6\text{-}2)$$

It is noted that

$$\Delta T = \frac{1}{2}\left(T_{t\Delta f} - T_{t\nabla f} - \Delta T_s\right)$$

and that the uncertainty of upper-tool surface temperature, $T_{t\Delta f}$, is determined only by the thermocouple readings, thermocouple locations and tool conductivity of the upper-tool. It is similar to the lower-tool surface temperature $T_{t\nabla f}$ and the temperature drop ΔT_s on the specimen. Therefore, $T_{t\Delta f}$, $T_{t\nabla f}$ and ΔT_s are independent of each other. Applying equation (3.6.1-1) (refer to Appendix 3.6.1),

$$(\delta \Delta T)^2 = \frac{1}{4}\left[(\delta T_{t\Delta f})^2 + (\delta T_{t\nabla f})^2 + (\delta \Delta T_s)^2\right] \qquad (3.6\text{-}3)$$

$$q = \frac{1}{2}\left(q_{t\Delta} + q_{t\nabla}\right)$$

Similarly, heat flux $q_{t\Delta}$ on the upper-tool, and $q_{t\nabla}$ on the lower-tool can be considered independent of each other, therefore

$$(\delta q)^2 = \frac{1}{4}\left[(\delta q_{t\Delta})^2 + (\delta q_{t\nabla})^2\right] \qquad (3.6\text{-}4)$$

From equation (3-8)

$$\Delta T_s = \frac{q}{k_s} t$$

It can be known that the computation of average heat flux is irrelevant to specimen parameters, therefore,

$$(\delta \Delta T_s)^2 = \left(\frac{t}{k_s}\delta q\right)^2 + \left(\frac{qt}{k_s^2}\delta k_s\right)^2 + \left(\frac{q}{k_s}\delta t\right)^2 \qquad (3.6\text{-}5)$$

The current specimen thickness was measured with a micrometer after each test, and the measured dimension was used in the h-value computation. Therefore, uncertainty δt is small. Obviously, $T_{t\Delta f}$, $T_{t\nabla f}$, ΔT_s and q are functions of readings of the corresponding thermocouples, their locations, tool and specimen conductivity. For simplicity of analysis, uncertainty of the specimen conductivity is ignored. Thus the upper-tool surface temperature can be expressed as

$$T_{t\Delta f} = T_{t\Delta f}\left(\vec{T}, \vec{Z}, k_{t\Delta}\right)$$

Note that uncertainties of the thermocouple records, thermocouple locations and materials properties are independent of each other. Thus,

$$\left(\delta T_{t\Delta f}\right)^2 = \left(\frac{\partial T_{t\Delta f}}{\partial k_{t\Delta}}\delta k_{t\Delta}\right)^2 + \sum\left(\frac{\partial T_{t\Delta f}}{\partial T_i}\delta T_i\right)^2 + \sum\left(\frac{\partial T_{t\Delta f}}{\partial z_i}\delta z_i\right)^2 \qquad (3.6\text{-}6)$$

and,

$$\delta T_i \le \delta T_0$$

$$\delta z_i \le \delta z_0$$

By substituting both these inequalities in equation (3.6-6), we have

$$\left(\delta T_{t\Delta f}\right)^2 \le \left(\frac{\partial T_{t\Delta f}}{\partial k_{t\Delta}}\delta k_{t\Delta}\right)^2 + (\delta T_0)^2\sum\left(\frac{\partial T_{t\Delta f}}{\partial T_i}\right)^2 + (\delta z_0)^2\sum\left(\frac{\partial T_{t\Delta f}}{\partial z_i}\right)^2 \qquad (3.6\text{-}7)$$

In a similar manner

$$(\delta T_{t\nabla f})^2 \le \left(\frac{\partial T_{t\nabla f}}{\partial k_{t\nabla}}\delta k_{t\nabla}\right)^2 + (\delta T_0)^2 \sum\left(\frac{\partial T_{t\nabla f}}{\partial T_i}\right)^2 + (\delta z_0)^2 \sum\left(\frac{\partial T_{t\nabla f}}{\partial z_i}\right)^2 \quad (3.6\text{-}8)$$

$$(\delta q_{t\Delta})^2 \le \left(\frac{\partial q_{t\Delta}}{\partial k_{t\Delta}}\delta k_{t\Delta}\right) + (\delta T_0)^2 \sum\left(\frac{\partial q_{t\Delta}}{\partial T_i}\right)^2 + (\delta z_0)^2 \sum\left(\frac{\partial q_{t\Delta}}{\partial z_i}\right)^2 \quad (3.6\text{-}9)$$

$$(\delta q_{t\nabla})^2 \le \left(\frac{\partial q_{t\nabla}}{\partial k_{t\nabla}}\delta k_{t\nabla}\right)^2 + (\delta T_0)^2 \sum\left(\frac{\partial q_{t\nabla}}{\partial T_i}\right)^2 + (\delta z_0)^2 \sum\left(\frac{\partial q_{t\nabla}}{\partial z_i}\right)^2 \quad (3.6\text{-}10)$$

In circumstances when the conductivity of the tools cannot be considered constant, all equations from (3.6-5) to (3.6-10) cannot be expressed as analytical and explicit functions of T_i and z_i, due to the fact that temperature T and heat flux q cannot be expressed explicitly. However, the tool surface temperature can be expressed as a function of thermocouple readings and their relative locations through regression analysis. Therefore, the overall uncertainty of the h-value determined from equation (3.6-2) can be evaluated by numerical methods using equations (3.6-7)~(3.6-10). A numerical uncertainty analysis procedure was programmed and used to analyse the overall uncertainty of h-value.

Note that δz_0 is determined by the difference between the thermocouple installation hole diameter and that of thermocouple, and the accuracy of location measurement. The diameter of thermocouple is 0.5 mm and the installation hole diameter is 0.6 mm; the relative position of the thermocouple hole locations were measured by a microscope being accurate to microns, therefore, the uncertainty of the thermocouple hole locations can be ignored; thus, $\delta z_0 \approx \pm 0.05mm$. The National Physical Laboratory measured the tool conductivity with an accuracy of 4%, thus $\delta k_{t\Delta} = \delta k_{t\nabla} \approx \pm 0.8\left(Wm^{-1}K^{-1}\right)$. K-type of thermocouples were used in the experiments, which, after calibration, showed that $\delta T_0 = \pm 0.1\,^{\circ}C$. δk_s can be assumed as 5% of the k_s, i.e., $\delta k_s = \pm 3.0\left(Wm^{-1}K^{-1}\right)$. Under these conditions the numerical analysis was performed for pressures from 30 MPa to 180 MPa, from which the following conclusions can be drawn:

- The value of the third term in equations (3.6-7) to (3.6-10) is less than 4.5% of the middle term due to small variation of δz_0. It appears that small thermocouple location uncertainties would not influence heat flux density and the computation of tool surface temperature; contribution of δz_0 can be ignored compared with the influence of the uncertainty δT_0.

- The value of the first term in equation (3.6-7) and (3.6-8) is less than 0.75% of the middle term; therefore, small variations in tool conductivity does not affect tool surface temperature; $\delta k_{t\Delta}$ and $\delta k_{t\nabla}$ in equation (3.6-7) and (3.6-8) can be ignored. In fact, if tool material conductivity is considered constant, it can be proved mathematically that both, $T_{t\nabla f}$ and $T_{t\Delta f}$ are independent of k_t.

- In equations (3.6-9) and (3.6-10), the third term is less than 3.0% that of the first term. Thus

$$(\delta q)^2 \le \left(\frac{\partial q}{\partial k_t}\delta k_t\right)^2 + (\delta T_0)^2 \sum \left(\frac{\partial q}{\partial T_i}\right)^2$$

It can be proved by substituting the above expression into equation (3.6-5) that

$$(\delta \Delta T_s)^2 = \frac{q^2 t^2}{k_s^2 k_t^2}(\delta k_t)^2 + \left(\frac{k_t}{k_s}\right)^2 \frac{nt^2}{n\sum z_i^2 - \left(\sum z_i\right)^2}(\delta T_0)^2 + \left(\frac{qt}{k_s^2}\delta k_s\right)^2 \quad \text{(3.6-10A)}$$

In the experimental equipment, $t^2 << n\sum z_i^2 - \left(\sum z_i\right)^2$, and $\frac{k_t}{k_s} = 0.333$, therefore,

$$(\delta \Delta T_s)^2 = \frac{q^2 t^2}{k_s^2 k_t^2}(\delta k_t)^2 + \left(\frac{qt}{k_s^2}\delta k_s\right)^2$$

Pay attention to the fact that $q \approx 30\times10^3\ Wm^{-2}$, $t = 1 \sim 4\times10^{-3}\ m$, $k_s = 60\ Wm^{-1}K^{-1}$, $k_t = 20\ Wm^{-1}K^{-1}$, $\delta k_t = 0.8W$, $\delta k_s = 3.0W$. Thus

$$\delta \Delta T_s \approx T_c \frac{t}{t_0} \quad \text{(3.6-10B)}$$

where, $t_0 = 1.0\ mm$ and $T_c = 0.025\ ^\circ C$

Subsequent to the above simplifications, the uncertainty of the computational h-value can be expressed as

$$\delta\Delta T = \frac{1}{2}\left\{\left[\sum\left(\frac{\partial T_{t\Delta f}}{\partial T_i}\right)^2 + \sum\left(\frac{\partial T_{t\nabla f}}{\partial T_i}\right)^2\right](\delta T_0)^2 + \left(T_c\frac{t}{t_0}\right)^2\right\}^{\frac{1}{2}} \qquad (3.6\text{-}11)$$

Let

$$\alpha = \frac{1}{2}\left[\sum\left(\frac{\partial T_{t\Delta f}}{\partial T_i}\right)^2 + \sum\left(\frac{\partial T_{t\nabla f}}{\partial T_i}\right)^2 + \left(\frac{T_c}{\delta T_0}\frac{t}{t_0}\right)^2\right]^{\frac{1}{2}} \qquad (3.6\text{-}12)$$

The uncertainty of the computation of h-value can be simplified to:

$$\left|\frac{\delta h}{h}\right| = \alpha\left|\frac{\delta T_0}{\Delta T}\right| \qquad (3.6\text{-}13)$$

α is referred to as uncertainty coefficient. Equation (3.6-12) shows that uncertainty coefficient is determined by the differentials of tool surface temperatures to the thermocouple readings. Equation (3.6-13) shows that the overall uncertainty of h-value is proportional to the accuracy of thermocouple and inversely proportional to interfacial temperature drop. The temperature drop is sensitive to both interfacial pressure and surface texture. Therefore, the overall uncertainty of h-value is a function of contact conditions, including surface texture and interfacial pressure. This character has been ignored [5,7,9-11,29].

An approximate analysis can be carried out to show the fact that uncertainty coefficient α is a parameter only related to the positioning of thermocouples on tools. Although tool conductivity is defined as a second exponential function of temperature (refer to equation (3.1-2)), its main component is constant; the variable part is less than 10% when temperature varies in the range 0~300 °C. –refer to Fig. 3.5. Thus, the main character of tool conductivity continues to be similar to constant tool conductivity. When the tool conductivity can be approximated as constant, tool surface temperature can be expressed as linear function of thermocouple readings and thermocouple location parameters by linear regression analysis. Therefore, $\frac{\partial T_{t\Delta f}}{\partial T_i}$ or $\frac{\partial T_{t\nabla f}}{\partial T_i}$ will be the function of thermocouple locations only; uncertainty

coefficient α is a structural parameter. Numerical analysis without any simplification shows $\alpha \approx 0.725$ for the current experimental equipment.

Mathematically, if tool conductivity is constant, the one-dimensional tool temperature field is

$$T = \frac{q}{k} z + C \tag{3.6-14}$$

And linear regression analysis gives the integration constants C and q:

$$q = k \frac{n\sum z_i T_i - \sum z_i \sum T_i}{n\sum z_i^2 - \left(\sum z_i\right)^2}$$

$$C = \frac{\sum z_i^2 \sum T_i - \sum z_i \sum z_i T_i}{n\sum z_i^2 - \left(\sum z_i\right)^2}$$

In particular, if the origin of the co-ordinate system is at the tool surface, the constant C in equation (3.6-14) happens to be the extrapolated value of temperature at the tool surface. Taking the upper tool as an example,

$$T_{i\Delta f} = \frac{\sum z_i^2 \sum T_i - \sum z_i \sum z_i T_i}{n\sum z_i^2 - \left(\sum z_i\right)^2}$$

where i shows the sum of all thermocouples on the upper-tool. From this,

$$\left(\frac{\partial T_{i\Delta f}}{\partial T_i}\right)^2 = \frac{\left(\sum z_i^2\right)^2 - 2z_i \sum z_i \sum z_i^2 + z_i^2 \left(\sum z_i\right)^2}{\left[n\sum z_i^2 - \left(\sum z_i\right)^2\right]^2}$$

$$\sum \left(\frac{\partial T_{i\Delta f}}{\partial T_i}\right)^2 = \frac{\sum z_i^2}{n\sum z_i^2 - \left(\sum z_i\right)^2} \tag{3.6-15}$$

Similarly,

$$\sum \left(\frac{\partial T_{i\nabla f}}{\partial T_m}\right)^2 = \frac{\sum z_m^2}{n\sum z_m^2 - \left(\sum z_m\right)^2} \tag{3.6-16}$$

where m shows the sum on the lower tool. Substituting equations (3.6-16) and (3.6-15) into equation (3.6-12) and simplifying

$$\alpha = \frac{1}{2}\left[\frac{2\sum z_i^2}{n\sum z_i^2 - \left(\sum z_i\right)^2} + \left(\frac{T_c}{\delta T_0}\frac{t}{t_0}\right)^2\right]^{\frac{1}{2}} \tag{3.6-17}$$

Compared with numerical analysis result $\alpha = 0.725$, the value of α determined by equation (3.6-17) is $\alpha = 0.735 \sim 0.88$. It can be observed that the coefficient α is a geometrical parameter, which relates to the location of thermocouples and the total number of thermocouples on a tool. This suggests that uncertainty of h-value is not only related to the uncertainty of thermocouple but also to the positioning thermocouples. Since the accuracy of h-value is a function of the positioning of thermocouples, an optimal positioning of the thermocouples can be defined analytically, at which the most accurate evaluation of h-value can be achieved. The detailed analysis is discussed in Appendix 3.6.2.

Equation (3.6-17) results in a close h-value uncertainty to that of numerical analysis.

It is interesting to note that in equation (3.6-13),

$$\left|\frac{\delta h}{h}\right| = \alpha\left|\frac{\delta T_0}{\Delta T}\right| = \frac{\alpha|\delta T_0|}{q}\left|\frac{q}{\Delta T}\right| = h\frac{\alpha|\delta T_0|}{q} \qquad (3.6\text{-}18)$$

Uncertainty coefficient α is determined by experimental equipment structural parameters; variation of q is small and δT_0 can be considered constant. Thus, distribution of the h-value uncertainty is almost proportional to value of h. This is the reason why the computation of h will become unstable when the interfacial pressure reaches a threshold. This threshold exists no matter how thermocouples are calibrated; more accurate calibrations can only raise the level of the threshold. At meanwhile, both α and δT_0 can be considered constant, therefore, equation (3.6-18) shows that the uncertainty of h-value varies according to hyperbola function of temperature drop. The variation pattern of the uncertainty of h-value is determined by the variation pattern of interfacial temperature drop. Figs. 3.6.1~3.6.5 show the variation of h-value uncertainty to surface roughness and surface interfacial pressure. By comparing these analytical uncertainties with those of the repeated experiments, as shown in Figs 3.24~3.29, most of the data is in agreement; for fine specimens the analytical results are conservative. These may be the consequence of approximating conditions used in the analysis and the limitation of the repeated experiment times.

The following conclusions can be drawn from Fig. 3.6.1~3.6.5 and above discussion.

- Uncertainty of the computation of h-value mainly depends on four factors, the thermocouple accuracy, the interfacial pressure, the surface texture and the positioning thermocouples. For low values of interfacial pressure, of the order of 60 MPa, the accuracy is high. This agrees with previous research [5,7,9-11,29].

- The uncertainty of h-value increases with increase of interfacial pressure. For example, when interfacial pressure is 30 MPa, the uncertainty of h-value is in the order of 3%~11%. However, when the interfacial pressure is 300 MPa, the uncertainty of h-value is of the order of 20%~250%, depending on the surface texture.

- The uncertainty of h-value increases as the surface texture is improved. The improved surface texture may result from surface compression or initially fine manufacturing operations.

- No matter how thermocouples are carefully and individually calibrated, there is a threshold of interfacial pressure for steady temperature-based h-value evaluation method, beyond which the evaluation of the h-value will be unreliable; this threshold is defined by specimen initial surface texture, thermocouple accuracy and the positioning of the thermocouples.

- Too larger specimen thickness may influence the experimental accuracy. 1~2 mm thickness is preferred.

Appendix 3.6.1

Method of Single-Sample Experiment Uncertainty Analysis

Assuming that $R = R(x_1\, x_2\, x_3 ... x_n)$ is the computed result in which x_i is the i^{th} physical quality to be measured in order to compute R. If uncertainty of every x_i is

independent of each other, i.e., the uncertainty δx_i of x_i does not affect the uncertainty δx_j of another quantity x_j, then the overall uncertainty of R [30] can be evaluated in the following manner:

$$\delta R = \left[\sum \left(\frac{\partial R}{\partial x_i} \delta x_i \right)^2 \right]^{\frac{1}{2}}$$

or

$$\left| \frac{\Delta R}{R} \right| = \left[\sum \left(\frac{1}{R} \frac{\partial R}{\partial x_i} \delta x_i \right)^2 \right]^{\frac{1}{2}} \qquad (3.6.1\text{-}1)$$

If x_i is dependent of each other, the uncertainty of ΔR can be written as [32]

$$\left| \frac{\Delta R}{R} \right| = \left[\sum \left(\frac{1}{R} \frac{\partial R}{\partial x_i} \delta x_i \right)^2 + 2 \sum \frac{\partial R}{\partial x_i} \frac{\partial R}{\partial x_j} \delta x_{i,j} \right]^{\frac{1}{2}} \qquad (3.6.1\text{-}2)$$

where $\delta x_{i,j}$ is the uncertainty of covariance estimation of x_i and x_j.

Appendix 3.6.2

Optimum positioning of thermocouples

As has been pointed out, the uncertainty of the computation of h-value depends on both, the accuracy and the location of the thermocouples. Initially, the locations of the lowest and highest thermocouples must be defined by the physical and structural conditions. Theoretically, the farther away from the interface the top thermocouple is located, the better. The distribution of the remaining thermocouples to minimise the h-value uncertainty will be considered in the following analysis, with reference to Fig. 3.6.2.1. In equation (3.6-17), let

$$\frac{\partial \alpha^2}{\partial z_j} = 0$$

Thus,

$$\frac{\partial \alpha^2}{\partial z_j} = \frac{1}{2} \sum z_i n \frac{\sum z_i^2 - z_j \sum z_i}{\left(n \sum z_i^2 - \left(\sum z_i \right)^2 \right)^2} = 0 \qquad (3.6.2\text{-}1)$$

or

$$\sum z_i \left(\sum z_i^2 - z_j \sum z_i \right) = 0$$

Two alternatives can be considered: either $\sum z_i = 0$, or $\sum z_i^2 - z_j \sum z_i = 0$. $\sum z_i = 0$ is geometrically and physically not advisable. –refer to Fig. 3.6.2.1. Therefore, the following conditions are considered

$$\sum z_i^2 - z_j \sum z_i = 0 \qquad (3.6.2\text{-}2)$$

Equation (3.6.2-2) is corresponding to the j^{th} thermocouple. –refer to equation (3.6.2-1). For the $(j+1)^{th}$ thermocouple, we have

$$\sum z_i^2 - z_{j+1} \sum z_i = 0 \qquad (3.6.2\text{-}3)$$

Subtracting equation (3.6.2-3) from equation (3.6.2-2) resulting in

$$(z_j - z_{j+1}) \sum z_i = 0$$

Similarly, $\sum z_i \neq 0$, and z_1 (the lowest location) and z_n (the top location) are given, therefore,

$$z_2 = \cdots = z_{n-1} \qquad (3.6.2\text{-}4)$$

Substituting equation (3.6.2-4) into equation (3.6.2-2)

$$z_1^2 + z_n^2 - z_j (z_1 + z_n) = 0 \qquad (3.6.2\text{-}5)$$

It can be shown that $z_j = (z_1^2 + z_n^2)/(z_1 + z_n)$ is a solution which will maximise equation (3.6-17). Note that equation (3.6.2-2) is a factor of $\frac{\partial \alpha^2}{\partial z_j} = 0$ from which it can be concluded that α is a monotonously increasing function of z_j before it reaches $z_j = (z_1^2 + z_n^2)/(z_1 + z_n)$. Therefore, equation

$$z_j = z_1 \qquad (3.6.2\text{-}6)$$

defines the minimum α. However, it would not be possible to locate $n-1$ thermocouples at the same position. Any way, equation (3.6.2-4) indicates that the remaining $n-2$ thermocouples should be located as close as possible to the interface to minimise the uncertainty of the computation of the h-value.

For the determination of the highest thermocouple location x_n, equation (3.6.2-5) is considered again. As a factor of $\frac{\partial \alpha^2}{\partial z_j} = 0$, taking $j = n$ in equation (3.6.2-5), the

factor becomes $(z_1^2 - z_1 z_n)$. Obviously any $z_n > z_1$ will make $\frac{\partial \alpha^2}{\partial z_j} < 0$; and a larger z_n results in a smaller negative differential $\frac{\partial \alpha^2}{\partial z_j}$. Therefore, the larger the z_n is, the smaller the uncertainty structural coefficient will be.

Summarising the discussion above.

- One thermocouple should be located as close as possible to the interface.
- The farther thermocouple should be located as far as possible from the interface.
- Remaining thermocouples should be located close to the first thermocouple.

Fig. 3.6.2.1 shows the thermocouple positioning in the experimental equipment with an uncertainty coefficient $\alpha = 0.74$. If the positioning changed into the locations shown in brackets, the coefficient will be $\alpha = 0.45$; accuracy of computation of the h-value will increase.

Chapter Four

FE Simulation of Contact Surface Deformation

4.1 Summary

A thermal contact conductance model usually consists of three sub-models: surface geometric model, surface deformation model, and heat transfer model. In these three sub-models, the surface geometric sub-model is most controversial. Different asperity models with simple geometric forms, such as sphere, cone and cylinder, were presented. The heights of these simple asperities were assumed to satisfy a random distribution, fitted with the surface texture parameters. However, when the real contact area of an individual asperity was computed for the simulation of the contact between a rough surface and a rigid plane, difficulties were encountered when plastic deformation occurred. Therefore, most surface deformation sub-models used an intersectional cross-section area as the real contact area of an individual contact asperity. This approach does not satisfy the basic plasticity equations.

Theoretically, the bearing ratio curve or material ratio of a surface profile could be used to represent the basic characteristics of the surface profile, such as arithmetical mean deviation or root mean square deviation (surface roughness), mean line position, profile height and intersection area at any level. Therefore, the form of the bearing ratio curve of a surface profile is a general representation of the form of the surface asperities. Based on this, a concept of equivalent asperity was adopted. This equivalent asperity is a general representation of the surface texture with the same surface geometric and statistic parameters and is a unique representation of the surface. Although it does not exist in reality, it is a good representation of the actual surface profile.

Contact between an isotropic rough surface and a rigid plane may be described by the contact between the equivalent asperity and the rigid plane. Elastic-plastic FE analysis can be used to simulate this contact. Surface deformation was successfully simulated using FE; its deformation pattern satisfies the basic elastic-plastic equations from which the real contact area was obtained as a function of nominal interfacial pressure.

The developed method was used to predict the variation of surface texture under different interfacial pressures. It was found that the FE simulated surface roughness (arithmetic mean deviation to mean line) variations were in agreement with those measured.

4.2 Nomenclature

A	Area
D	Sum of squares of deviation of surface profile to mean line
L	Evaluation length used in surface measurement
$\overline{L}$	Length of the expanded bearing ratio curve along $\overline{x}$ direction
n	Number
P_c	Peak density of surface profile
R_a	Surface roughness
R_q	Root-mean-squares deviation of surface profile
R_t	Total height of surface profile
S	Mean spacing of surface profile
x, y	Co-ordinate system used to describe surface profile
X, Y	Co-ordinate system used in description of bearing ratio curve
$\overline{x}, \overline{y}$	Co-ordinate system used in description of expanded bearing ratio curve

Subscripts

b	Parameters related to bearing-ratio curve
p	Parameters related to surface profile
i	The i^{th} peak above the mean line

j The j^{th} valley below the mean line

k The k^{th} intersected area of the surface profile

l The l^{th} node on equivalent asperity profile, or the corresponding element

Δ Above mean line

∇ Below mean line

Superscripts

$\overline{(\,)}$ Expanded bearing ratio curve

4.3 Introduction

All mechanical components have functional surfaces; the mechanical relationships between components are their contact surfaces. Mechanical loads, stresses, thermal loads, or even electric loads, are transmitted through contact surfaces. Mechanical contact determines heat flow across contact surfaces. Surface contact is a subject that is closely related to kinetics, dynamics, tribology, wear, heat-transfer, micro-mechanics, surface mechanics and life of mechanical components. Therefore, surface investigation is an important research field in engineering.

Thermal contact is of special significance in metal forming. A billet, regardless of whether it is hot, warm or cold, must contact with elastic tool surfaces. Forming forces are supported by surfaces; heat, contained in the billet or derived from plastic deformation, is transferred from the work material to tool surfaces, the extent of the transfer being determined by the thermal characteristics of the interface. This heat transfer has an effect on the forming accuracy. Thermal contact conductance is the main thermal property and is determined by the "real contact area" [1]. Microscopically, surfaces are rough. Therefore, two contacting surfaces are in fact in contact only at some locations [1~3], as shown in Fig. 4.1; the really contacted area will be less than the nominal contact area. The computation of the contact area has been the subject of much research effort [1~10]. Different surface deformation models have been presented to define the real contact area or the contact area ratio.

4.3.1 Elastic surface deflection model

Greenwood and Williamson [1] presented an elastic surface deflection contact model, referred to as GW model, based on the following assumptions:

1. Contact occurs between a rough surface and a rigid plane;
2. Surface texture of the rough surface is isotropic; surface parameters are independent of measuring location and orientation;
3. All asperities on the rough surface are spherical and with the same radius;
4. The height of asperity is random and is a Gaussian distribution;
5. Asperities are distributed uniformly on the surface with known density;
6. There is no interaction between asperities;
7. Contacted asperities deform elastically according to the Hertzian contact theory.

Fig. 4.2 is geometrical representation of the GW contact model. Assumption 7 restricts the GW model to low contact pressures. Assumption 3 over-simplifies the surface texture. Later researchers presented different contact models. McCool [2], Greenwood and Trip [3], and O'Callaghan and Cameron [4] established models for anisotropic rough surfaces with randomly distributed asperity radii.

The CMY-model, presented by Cooper, Mikic and Yovannovich, was based on isotropic surfaces having no variations in surface profile heights and slopes with different orientations [5]. The Mikic-model was presented by Mikic, based on a further assumption that elastic contact area is half of the plastic contact area [6]. Bush, Gibson and Thomas [7], Whitehouse and Archard [8] developed similar models.

Although many different surface deflection models have been presented, the general approaches are similar. It is assumed that the mathematical representation of surface roughness is a set of independently deformed asperities scattered uniformly over a reference plane. Asperities are of a prescribed uniform geometry and their heights follow a known statistical distribution. Researchers have used a Hertzian approach to define the deflection law of individual asperity. By assuming the basic form of surface asperities and their distribution, the mean contact area and the elastic contact

theory formed the foundations of different classical models of surface deflection. All of these are only suitable for low contact pressure. Therefore, all these surface deflection models were referred to as a family of asperity-based model [9]. The analysis of surface contact under higher interfacial pressure was attended to using plastic surface deformation models.

4.3.2 Plastic surface deformation model

A model of the surface deformation was presented by Abott and Firestone [10] in 1933. According to this model, the real contact area is the area of geometrical intersection between a rough surface and a plane at an intersection level, instead of being determined by Hertzian contact solution. However, volume-constancy is not observed since plastic deformation is not considered. Fig. 4.3 shows two classical deformation models of asperities, -spherical [11] and conical [12], where area refers to the contact area after plastic surface deformation. Of course, from the plasticity point of view, these types of plastic deformation do not exist. More recent research addresses volume-constancy by Pullen and Williamson [11] who showed that the displaced material reappears as a uniform rise of the subsurface.

GW model [1], as well as other models of elastic surface deflection, were extended into plastic deformation models such as CMY model [5], Mikic model [6], BGT model [7] and WA model [8]. The overall approach is very similar. The intersectional area at a level was considered as real contact area. The product of the real contact area and yield strength or surface micro-hardness of the material was considered as the load on the individual asperity. The overall load and real contact area could be further determined by statistical analysis and mechanical macro-balance during contact. Many attempts have been made to solve the problem of material conservation encountered by classic plastic deformation models. However, these efforts were mainly concentrated on geometrical analyses instead of plasticity [13-14].

4.3.3 Elastic-plastic surface deformation models

The so-called elastic-plastic surface deformation model is, in fact, the combination of the elastic surface deflection model and the plastic surface deformation model [6,14]. A critical interfacial pressure was proposed at which the Hertzian contact area reaches a maximum. If contact pressure is less than the critical value, the deformation is considered elastic and the contact area is determined by the Hertzian contact solution; if the contact pressure is in excess of the critical interfacial pressure, the intersection area is considered as the contact area. The product of the geometrical intersection area and the surface micro-hardness of the material is the contact load on an individual asperity, under which the plastic contact area, as shown in Fig. 4.3, could be determined using macro-force equilibrium equations. These force equilibrium equations can be regarded as the equivalents of the stress equilibrium equations in plasticity. However, the deformation pattern determined by the geometric cross-section cannot match the constitutive equations and the plasticity equations.

4.3.4 Finite-element model of surface deformation

Kucharski [9] presented the first finite-element model of surface contact deformation in 1994. The asperity was simplified to a spherical form. Thus, axisymmetric FE analysis was used to analyse the deformation of the asperity. The radii of the geometrical models were 30 and 153 mm respectively; large asperity radii were taken to avoid numerical problems. A quarter of the sphere was considered in geometric model, as shown in Fig. 4.4a. Fig. 4.4b shows the deformation pattern of the asperity; the conclusions were that the cross-sectional area was not equal to the contact area and the displaced material does not reappear as a uniform rise of the non-contacting surfaces [14]. These conclusions were not of general significance due to the random character of rough surfaces and the form of the asperity selected for the study. Any assumption of a random distribution of asperities, either in their forms or in their heights, will result in numerous different forms of individual asperities [14-15]. However, FE simulation can be only applied to analyse a few or finite individual asperities. Therefore, a difficulty would be encountered if FE simulation was applied to predict surface deformation.

4.3.5 Real contact area-measuring methods

Two methods are available for measuring the real contact area. Kellow [16] used a model of Plasticine billet that was geometrically similar to the steel billet under investigation. One surface of this Plasticine billet represented a replica of a saw cut steel surface. A glass prism was placed in contact with this surface to determine the real contact area under different pressures. While the method offered visualisation, Plasticine does not replicate the behaviour of steel well enough for the results to be meaningful. The second method was presented by Nishino et al. [17], in which a local-pressure sensitive film with a thickness of 200 μm was placed between contact surfaces. This film would exhibit a colour change under local pressure. The colour change is permanent, this enabling the real local contact pressure distribution to be defined. However, surface roughness is of the order of microns; a film with 200 microns thickness between the contact surfaces would modify the assumed contact conditions. Real contact area can be also evaluated by ultrasonic measurements [18]. The values of contact area determined from ultrasonic measurements are related to the micromechanical interaction and topography of the contacting surfaces using a micromechanical model of two rough surfaces in contact.

Although many elastic-plastic and plastic surface deflection/deformation models have been presented, it is impossible to satisfy the basic plasticity equations by the deformation pattern presented by any of these models (excluding elastic models) even by assuming ideal asperity geometries. For example, the constitutive relationship, stress equilibrium and strain consistency equations, cannot be satisfied by these deformation models. On the other hand, the results of experiments and those predicted by these models appear to be in agreement. The reason for this may be that, most of the experiments were for low contact pressures, in which the plastic deformation is not significant compared with the elastic deflection [19-21]. The contact pressure selected for most studies is about 1~10% of the yield strength of the material [22-26]. Usually, classical surface deflection models are accurate for contact at low pressures. If surface deformation is confined to the range of elastic deformation, the application of Hertzian contact solution is relevant. At the same

time, the application of random theory to surface mechanics is also practical, which accounts for the popularity of the Greenwood and Williamson model.

Some research, to establish thermal contact conductance under high interfacial pressures [16,26-36], has been reported. However, the real contact area was rarely considered due to difficulties in modelling; where modelling was essential, an optical approach was employed to measure the real contact area [16] which is restricted to plane surfaces only. The h-value, therefore, was generally measured by the calibration method or the reverse approach. However, it is difficult to establish a theoretical relationship between h-value and contact conditions, either by calibration or the reverse method. Thus, simulation of the real contact area and surface deformation under high contact pressure remains an urgent task.

4.4 Finite element model for simulating surface deformation

FE simulation of surface deformation of a rough surface contact with a perfect rigid or elastic plane is based on a so-called equivalent asperity of the surface. The equivalent asperity provides the geometrical model for FE simulation. Basic geometric characters of isotropic surface asperities can be represented by this equivalent asperity. The establishment of this equivalence between the equivalent asperity and the surface profile is closely related to the bearing ratio curve of the surface profile. Therefore, bearing ratio curve of a random surface and the significance that it presents in this research are analysed.

4.4.1 Bearing ratio curve as the representation of surface profile

Although three-dimensional surface parameters measurement by profile-meter is possible [37], it is not widely applied due to economic factors. In this research, a two-dimensional surface-profile-meter was used to measure the surface deformation under different interfacial pressures. Therefore, all surface parameters related to the following analysis are based on two-dimensional surface profiles.

Bearing ratio curve (BRC) is a concept of surface metrology used to describe the geometry of a surface profile two-dimensionally. Its definition is shown in Appendix

4.1. The BRC defines the intersected contact "area" at any depth below the top of the surface profile. Its significance in this research, however, is that, mathematically, the BRC is a general representation of the surface profile. If the bearing ratio curve is imaged as a surface profile, it can be shown that the most important surface parameters, such as mean line position, arithmetic mean deviation to mean line, root mean square deviation to mean line, intersection area at any depth and mean spacing, will remain exactly the same as those of the actual surface profile. Therefore, an asperity which has the basic form of the BRC, will represent the character of actual surface asperities better than any other simple geometries [1~10]. Mathematical analysis was conducted to show this significance of the bearing ratio curve and to establish the equivalence between the equivalent asperity and the surface profile; details are shown in Appendix 4.2.

By summarising the mathematical analysis in Appendix 4.2, an expanded bearing ratio curve (EBRC) (refer to Appendix 4.2), in which ordinate shows the height of surface profile, can be applied to represent exactly the same

- mean line position,
- intersected area at any intersectional level,
- surface roughness,
- root-mean-square deviation,
- and total height

as those of the actual surface profile. Therefore, the form of the EBRC is a general representation of the surface asperity form; this form of the EBRC may be used to construct a form of an equivalent asperity that represents the same above-mentioned surface parameters. Most importantly, the length of the EBRC in the $\bar{x}$-axis direction can be arbitrary, without influencing its correctness in representing the corresponding surface parameters.

Let's consider a surface profile $\overline{AB}$ of an isotropic and uniform surface, as shown in Fig. 4.5. The curves shown by $\overline{CGHKNMD}$ is the EBRCs corresponding to the segments of the surface profile. For example, the EBRCs corresponding to the surface profile $\overline{AE}$ and $\overline{EF}$ are $\overline{CG}$ and $\overline{GH}$ respectively. Meanwhile, the surface

is isotropic. Therefore, all the EBRCs are identical, the same as that corresponding to the surface profile $\overline{AB}$. On the other hand, the curve $\overline{CGHKNMD}$ can be defined as a surface profile, referred to as imaged surface profile, with four asperities G, K, M and N, referred to as *equivalent asperities*. The forms of these equivalent asperities are determined by the form of the EBRC of the surface profile $\overline{AB}$; therefore, all these equivalent asperities are identical. Obviously, the BRC of this imaged surface profile is identical to that of the surface profile $\overline{AB}$ from the definition shown in Appendix 4.1 and the theoretical analysis in Appendix 4.2. Therefore, the mean line position, the intersected area at any level, the surface roughness and the root-mean-square deviation of this imaged surface profile are also the same as those of the surface profile $\overline{AB}$. On the meantime, the basic characteristics of the imaged surface profile $\overline{CGHKNMD}$ can be also determined by any of the defined equivalent asperities due to their identity. This, therefore, suggests that the basic characteristics of an isotropic surface can be described by the form of an equivalent asperity. Attention should be paid to the fact that the number of the equivalent asperities corresponding to surface profile $\overline{AB}$ can be arbitrary based on mathematical analysis in Appendix 4.2, since the dimension $\overline{L}$ can be arbitrary. Based on these, the following definition of the equivalent asperity is presented.

4.4.2 Equivalent asperity

According the theoretical analysis in Appendix 4.2, an equivalent asperity is defined: *Using any point on an isotropic and uniform surface as a centre and using mean spacing, S, as diameter, may be drawn to define the parameter. All asperities inside this circle would be equivalent to a single axisymmetric asperity, referred to as the equivalent asperity, as long as the generating line is defined by the corresponding expanded bearing ratio curve.* An equivalent asperity is schematically shown in Fig. 4.6.

The imaged surface profile with this typical equivalent asperities, as shown in Fig. 4.5, shows the same surface roughness, root-mean-square deviation, total height, intersected area at any intersectional level, mean line position and mean spacing as

those of the actual surface profile. Thus, the equivalence between the actual surface profile and the equivalent asperity is established.

The equivalent asperity is a representation of a real isotropic surface profile; it can be considered as a statistical description of the form of the surface asperities; or statistically, surface asperities have the form of the equivalent asperity. As has been analysed in Appendix 4.2, the correctness of this representation of the actual surface profile by an equivalent asperity is not influenced by the diameter of the equivalent asperity. Therefore, geometrically, the diameter of the equivalent asperity can be arbitrary. However, considering the mechanical properties of a single asperity being related to its dimensions, the equivalent asperity with different diameter may have different mechanical properties. Therefore, using the "mean diameter" of the surface asperities as the diameter of the equivalent asperity may represent the surface mechanical properties better. Mean spacing is the mean width occupied by surface asperities on mean line; it can be considered as the mean diameter of the surface asperities. Thus, the diameter of the equivalent asperity is determined by the surface mean spacing. From this point of view, the equivalent asperity also shows the same mean spacing as that of actual surface profile. Obviously, this enables the imaged surface profile with equivalent asperities to have the same mean spacing as the actual surface profile.

The equivalent asperity is derived from an isotropic and uniform surface. Therefore, the definition may only be suitable for the analysis of uniform and isotropic surface contact. If the definition is used to analyse the surface with surface macro-irregularities or flatness, uncertainties may occur. In fact, flatness or surface macro-irregularities may not be included in the BRC due to the 4-mm cut-off length of the measuring instrument.

If the mean spacing S of the surface is defined as the diameter of the equivalent asperity, the equivalent asperity of a uniform and isotropic surface is unique. Equivalent asperity, being unique for a given uniform and isotropic surface, is significant to surface analysis; the equivalent asperity transforms a surface with

random asperities into a surface which is represented by a simple form, while most of the surface parameters remain unchanged. Thus, the equivalent asperity is proposed with a view to simplifying the analysis of a real surface; the equivalent asperity is defined to enable a FE model to analyse the elastic/plastic deformation of a random surface.

Using FE simulation, based on the equivalent asperity, surface deformation pattern determined by FE analysis will, therefore, satisfy all elasticity and plasticity equations.

4.4.3 Finite element model for simulation of surface deformation

4.4.3.1 Basic assumptions

The following assumptions are presented to enable the establishment of a FE surface deformation simulation model:

1) Contact occurs between a rough deformable surface and a perfectly rigid or elastic flat plane.
2) The rough surface is isotropic; surface parameters are independent of the measuring location and orientation.
3) The surface below nR_t remains flat after contact. $n = 2$ in the analysis. This assumption shows that a plane of specimen perpendicular to axis before contact remains a plane after contact.
4) The equivalent asperity comprises an asperity atop a cylinder of diameter, S. This cylinder remains a cylinder, capable of lateral expansion during the compression of the asperity. The validity of this assumption depends on the interfacial pressure and friction coefficient at the interface. If the pressure and friction coefficient are high, the macro-scale plastic deformation would occur with "barrelling". In this case the shape of the cylinder will depend on the pattern of macro-scale plastic deformation and is location dependent. However, the aspect ratio of the specimens used ranges from 0.056 ~0.22; barrelling is unlikely at these ratios.
5) The material adjacent to the equivalent asperity expands to infinity, as shown in Fig. 4.7. The total height R_t and mean spacing S are small in comparison with

the dimensions of the specimen. Therefore, any dimension of specimen can be regarded as being of infinite dimension; any point on the contact surface can be considered the centre of the equivalent asperity; equivalent asperity can be regarded as axisymmetric both geometrically and mechanically. However, this assumption may cause uncertainties for the equivalent asperities located sufficiently close to the rim of the specimen surface; precisely considering geometric conditions in this case would be difficult, theoretically.

6) It is assumed that the deformed equivalent asperity represents the deformed surface. While this could be shown by detailed surface measurements, it would be difficult to establish this equivalence mathematically, –refer to Fig. 4.8. All surface geometric parameters are evaluated from the profile of the deformed equivalent asperity by FE simulation; for example, R_a and R_q can be simulated using the co-ordinates of mesh after deforming by using

$$R_a = \frac{2}{S}\int_0^{\frac{S}{2}} |y| dx \tag{4-1}$$

$$R_q = \sqrt{\frac{2}{S}\int_0^{\frac{S}{2}} y^2 dx} \tag{4-2}$$

Therefore, *the compressed equivalent asperity is assumed as the equivalent asperity of the compressed surface.*

4.4.3.2 FE simulation model

The FE mesh model is shown in Fig. 4.9. The dimension of the equivalent asperity is small compared to the thickness of specimen; the height of the cylinder that supports the equivalent asperity is several orders greater than the diameter of the equivalent asperity. Infinite elements were used to enable FE modelling; these can cope with large domain mechanical problems. The vertical dimension of the part with infinite elements is required the same as that of the part with two-dimensional solid elements by the infinite element technique in ABAQUS. Twice of mean spacing dimension, S, of the surface profile was used as the dimension of the part with two-dimensional solid elements, considering that a space is needed for simulation of heat transfer. A relatively fine mesh was used for the equivalent asperity in order to simulate the real

contact area after plastic deformation of the asperity. The details of the fine mesh of the equivalent asperity before compression are shown in Fig. 4.10.

Infinite elements only determine the boundary condition in the axial direction while the boundary conditions on the surface of the cylinder remain unknown. However, assumption (4) defines that the cylinder remains cylindrical with possible lateral expansion. Therefore, all nodes on this cylindrical surface should share the same radial displacement. This is an approximate simulation to the constraint between the adjacent material in the specimen. An equation technique provided by ABAQUS to constrain all nodes on cylinder enables these to experience the same radial displacement.

If the interfacial pressure is low, the surface deflection/deformation may only be focused on the summit of the equivalent asperity; therefore, no interactions occur between the equivalent asperity and the asperities around it, just as assumed by Greenwood and Williamson [1]. When the interfacial pressure is high, surface deformation becomes finite. In this case Greenwood and Williamson's assumption would not apply and the interactions would occur between the equivalent asperity and the asperities around it. A suitable modelling technique is required to prevent material overlap. A cylinder referred to as virtually "rigid" cylinder that can expand in the radial direction is added to the base of the equivalent asperity to simulate the interactions between the equivalent asperity and asperities around it (refer to Fig. 4.11); this approach has not been referred to in previous research [1-14].

While it is permissible for asperities to contact each other, these do not overlap. This "rigid" cylindrical surface is attached to a node located on the surface of the cylinder that supports the equivalent asperity, so that the "rigid" cylinder can expand together with the cylinder of substrate material, -a translation, actually. Therefore, the virtual cylinder can have a uniform expansion or contraction, but cannot bend or rotate. When the equivalent asperity deforms without the virtual rigid cylinder, the deformation pattern may be similar to that shown in Fig. 4.11b. The actual interactions between asperities are shown in Fig. 4.11a.

4.4.3.3 Material

The specimen was made from Ma8 steel. The surface was first ground to flat, and then electro-discharge machined to the final dimensions and required surface texture. The constitutive equation of the specimen is:

$$\overline{\sigma} = 650(\overline{\varepsilon} + 0.02)^{0.22} \qquad \text{(MPa)} \qquad (4\text{-}3)$$

However, surface asperities are formed during electro-discharge machining process. Therefore, they may have a mechanical property different from that of substrate material due to the processing. It is difficult to measure the mechanical property of surface asperities. The influence of electro-discharge machining processing on material property is neglected in this work.

4.5 Surface measurement equipment

Surface texture measuring instrument SURFTEST-400 profile-meter was used in the specimen surface texture measurements. The measurement can be accurate to two decimal places in microns for any of the surface parameters. Standard reference surface samples with given surface parameters were provided by the manufacturer of the profile-meter, which were used to calibrate the profile-meter prior to surface measurements.

4.6 Procedures

4.6.1 Surface measurement procedure

Calibration proceeded every batch of measurements. Initially, surface texture of specimens was measured without compression; subsequently, surface compression and surface measurement were conducted. Therefore, surface texture as a function of interfacial pressure was evaluated. Surface compression was conducted on the equipment designed for the evaluation of thermal contact conductance that has been already discussed in Chapter 3. –refer to Fig. 3.3.

4.6.2 FE simulation procedure and requirement

Special procedures are required for the simulation of surface deformation. After withdrawing of the interfacial pressure, surface asperities spring back; therefore, textures of specimen surface in compression and after withdrawal of interfacial

pressure may be different. From the surface measurement procedure mentioned in section 4.6.1, the measured surface texture is the surface texture after spring-back. Thus, simulation should consider spring-back to enable a valid comparison between FE simulation and surface measurements. The surface texture after compression under a given interfacial pressure can be simulated by compressing the equivalent asperity under the given nominal interfacial pressure. All surface parameters that can be determined by bearing ratio curve can be evaluated using this deformed equivalent asperity profile after spring-back. Thus, simulation of surface textures at different interfacial pressures requires the repetition of the simulation procedures. If interfacial pressure is high, finite plastic deformation occurs. In this process, all state-information, such as stress, strain, displacement, at different interfacial pressure intervals are recorded. Thus, the spring-back process can be restarted from different interfacial pressure interval without repeating the elastic-plastic deformation simulations.

4.7 Results

4.7.1 Surface measurement results

Surface textures of specimens after compression under different interfacial pressures were measured. Some of the measured surface texture records are shown in Appendix 3.4 in Figs. 3.4.1~3.4.7; the measured data of surface roughness after compression under different interfacial pressures are shown Figs. 4.13~4.27.

4.7.2 FE simulation results

FE package ABAQUS was used to simulate surface deformation. Initially, the equivalent asperity was compressed till the highest required nominal interfacial pressure; subsequently, simulations of the spring-back of the equivalent asperity from different specified nominal interfacial pressures were restarted respectively. The mesh of specimen 3.0-D-420, after deformation under a pressure of 420 MPa is shown in Fig. 4.12. From the simulation results, the co-ordinates of the equivalent asperity profile can be obtained and the surface parameters, such as surface roughness and root-mean-square deviation, can be evaluated based on equations (4-

1) and (4-2). Figs. 4.13~4.27 show the surface roughness results predicted by FE simulation and surface roughness measurements under different interfacial pressures.

4.8 Discussions

Variation of surface texture is affected by different factors. Interfacial pressure, tool surface texture, preparation procedure of specimen and initial specimen surface texture influence the variation pattern of the specimen surface texture. Because interfacial pressure is controlled in a limit in which without obvious plastic deformation occurs in macroscale, interfacial friction will not play important part in surface texture variation.

4.8.1 Influence of the tool surface texture

It was illustrated in Chapter 3, by Figs. 3.10 and 3.11, that the surface texture of both tool surfaces are considered similar due to identical manufacturing process; the tool surface roughness was in the range $R_a = 0.22 \sim 0.30 (\mu m)$, depending on the measuring orientation. The surface is, to some extent, anisotropic due to the finish-grinding operation. The surface roughness parallel to the grinding direction is about 0.22 (μm) and 0.30 (μm) along the transverse direction. The influence of the tool surface texture on the variation pattern of the specimen surface can be explained by two extreme cases. Under high interfacial pressures, fine specimens with texture approximating to that of the tool begin to assume the texture of the tool, – effectively, the surface is coined under high pressures. –refer to Fig. 4.28. The typical example of this case is shown in Fig. 4.13. The initial surface roughness of the specimen 2.5-A (see Table 3.1) is 0.25 μm, between the range of the tool surface roughness. The consequences of the compression of the specimen by different interfacial pressures show that the surface roughness of the specimen is between the tool texture range, regardless of the interfacial pressure. The specimen surface roughness includes orientation derived by compressing under a high interfacial pressure; the isotropic texture of the specimen was transformed to an anisotropic form. This suggests that specimen surface texture adopted the tool surface texture. All fine specimens showed this similar surface texture variation pattern.

The other extreme case concerns the coarse specimen. If the surface of the specimen is much coarser than that of the tool, the texture of the tool does not influence the deformation of the specimen, as shown in Fig. 4.29. In this case, the tool surface is a perfectly rigid/elastic plane, the texture of which can be disregarded. Typical representation of this case is shown in Fig. 4. 18. The specimen surface texture varies with interfacial pressure continuously; the surface roughness of the specimen remains coarser than that of the tool surface.

Alternative cases have also been identified, as shown by Fig. 4.14 for specimen 1.5-B. The initial surface roughness of the specimen is 0.41 μm, marginally coarser than that of the tool. The surface roughness of the specimen decreases with a pattern matching that predicted by FE simulation. However, the change in surface roughness is insignificant when the texture corresponds to that of the tool; the variation of R_a, beyond this, is random and depends somewhat on the measuring location and orientation. Significantly, the specimen surface does not undergo further change.

4.8.2 The influence of the interfacial pressure

The influence of interfacial pressure on the variation of specimen surface texture is related to the initial surface texture of specimen and tool surface texture. As discussed in section 4.8.1, if specimen surface texture is close to that of the tool surface, interfacial pressure would not change the surface roughness of the specimen. However, this does not mean the specimen surface texture does not change; in fact, the tool texture is replicated on the specimen if the interfacial pressure was sufficiently high. –refer to Fig. 4.28.

If initial surface texture of specimen is sufficiently coarser than that of the tool, interfacial pressure is the most active influential factor to the variation of the specimen surface texture. Interfacial pressure improves the specimen surface texture. – refer to Fig. 4.29. This pattern has been shown by the experimental results and FE simulation results in Figs. 4.15~4.27.

Improvement of the surface texture by compression occurs mainly at initial stage of the compression. – refer to Fig. 4.18. When interfacial pressure increases from 0 to 50 MPa, the surface roughness of the specimen decreases by a value of 0.137 μm; a further 50 MPa increment of the interfacial pressure results in a further decrease of surface roughness of 0.051 μm. Later, the decrease of the surface roughness is nearly linear to the increase of the interfacial pressure. It is predictable that this process will continue till the surface roughness is close to that of the tool. When surface roughness is close to that of the tool, surface replication will replace surface improvement regardless of the interfacial pressure. This surface deformation process is of significance to the determination of h-value variation pattern since it defines the contact area variation. A similar analysis was conducted for another specimen, 2.5-D, as shown in Fig. 4.21. The improvement of surface roughness for every 50 MPa increment of interfacial pressure is different for each specimen; the surface deformation pattern, however, remains similar for all coarse specimens.

4.8.3 Influence of initial surface texture and surface macro-irregularities

Ma8 steel specimens were manufactured by turning, grinding and finish-EDM machining. Surface measurements indicated that the surface texture was isotropic. However, some specimens did not make uniform contact with the tool surface; the distribution of contact marks on the specimen surface was non-uniform and random. The non-uniform distribution of contact-asperities is referred to as surface macro-irregularities. Surface macro-irregularities leads to non-uniform contact between the specimen and the tool; part of the surface, which is in contact, would be finer than other parts which is not in contact; surface texture became, therefore, non-uniform.

4.8.4 Comparison between FE simulation and experimental results

The experimental data and FE simulation results are shown in Figs. 4.13~4.27. A comparison between them can be made.

FE simulation of surface deformation can predict the basic variation pattern of specimen surface texture when the initial specimen surface texture is much coarser than that of tools. However, the accuracy of the prediction depends on the

corresponding surface macro-irregularities. Typical examples are shown in Figs. 4.18~4.19, Fig. 4.21 and Fig. 4.25. If the distribution of contact marks is non-uniform, the corresponding surface measurement data is randomly distributed around the curve predicted by FE simulation. The reason for this has been discussed in section 4.8.3. Typical examples are shown by Figs. 4.15~4.17, 4.22~4.23.

FE simulation of surface texture variation with interfacial pressure when the initial specimen texture is almost similar to that of tools may result in unrealistic consequence. An example is shown in Fig. 4.14. Although the specimen surface texture variation is in agreement with that predicted by FE simulation for interfacial pressure less than 100 MPa, the FE simulation prediction departed from the experimental results for higher interfacial pressures. The difference is due to the assumptions made for creating the FE simulation model. The tool surface was assumed to be a perfectly flat rigid plane; the predicted specimen texture improves continuously with the increase of interfacial pressure. This assumption is only suitable for the case when specimen surface texture is much coarser than that of tools. In fact, the tool surface is rough and comparable to the initial surface texture of the specimen 1.5-B. This suggests that tool surface texture should be much finer than that of specimen to enable a valid comparison of FE simulation with surface measurements. Therefore, tools with finer surface texture in the experiment equipment will be beneficial.

An approximately linear relationship exists between R_a and R_q with a correlation coefficient $R = 0.99$ [37] for most engineering surfaces; it has been shown that

$$R_a = 0.78 R_q$$

This equation is applicable to the equivalent asperity. Therefore, the comparison of root-mean-square deviations between experiment and FE simulation will be similar to the comparison of surface roughness R_a.

4.8.5 Different applications of the equivalent asperity FE model

Theoretical analysis, in Appendix 4.2, shows that the equivalent asperity is a more suitable representation of the actual surface profile than a two-dimensional infinitely

long ridge asperity [39] is. The two-dimensional infinitely long ridge form of asperity was used by Wanheim and Bay [39] to simulate the real contact area and further predict the friction coefficient between surfaces. Therefore, the equivalent asperity FE model can be applied to predict the friction coefficient between a rough surface and a rigid plane as a function of nominal interfacial pressure, – an analogy of the contact between tool and billet in cold forming. The details are discussed in Appendix 4.3.

4.9 Further considerations

Although the equivalent asperity is applicable to represent an isotropic rough surface and used to simulate the surface deformation in contact with a rigid/elastic plane, it is still difficult to simulate the contact between billet and tool surfaces considering sliding and surface expansion, which are involved in the contact during cold forming. Besides, surface contact conditions in cold forming are more complex considering lubrication. More investigation efforts are required to apply the equivalent asperity to simulate the actual surface deformation of billet during cold forming.

4.10 Conclusions

Summarising the above discussion, the following conclusions can be obtained for this chapter:

1) The concept of the equivalent asperity based on surface texture measurements can be used to describe surface texture. It is a stochastic description of an isotropic random surface. The equivalent asperity represents the real surface texture to which it conforms in the following critical areas,
   - surface roughness,
   - root-mean-square deviation,
   - total height,
   - intersected area at any level,
   - mean line position,
   - and mean spacing.

2) The assumption that the equivalent asperity, after deformation, represents the compressed surface has been shown to hold. Thus, an effective approach for predicting surface deformation and surface parameters by FE simulation has been proven. A surface deformation FE simulation model, based on the equivalent asperity, was established and used to successfully predict the surface deformation pattern and surface texture.

3) Surface texture of specimens improves continuously with increase of the interfacial pressure till the surface roughness is close to that of the tool, and the tool surface texture is, then, replicated on the specimen.

4) Surface macro-irregularities are a key factor that influences the difference between surface textures predicted by FE simulation and the measured.

5) The FE simulation model based on the equivalent asperity can be applied to improve the Wanheim-and-Bay friction model

4.11 References

1. J. A. Greenwood and J. B. P. Williamson, Contact of Nominally Flat Surface, Proceedings of Royal Society of London, A, Vol. 295, 1966, pp. 300-319
2. J. McCool, Predicting Micro-Fracture of Ceramics via Micro Contact Model, ASME Journal of Tribology, Vol. 108,1986, pp. 380-386
3. J. P. Greenwood and J. H. Tripp, The Contact of Two Nominally Flat Rough Surfaces, Proceeding of Institute of Mechanical Engineering, Vol. 185, 1971, pp. 625-633
4. M. O'Callaghan and M. A. Cameron, Static Contact under Load between Nominally Flat Surfaces in Which Deformation Is Purely Elastic, Wear, Vol. 45, 1976, pp. 79-97
5. M. G. Cooper, B. B. Mikic and M. M. Yovanovich, Thermal Contact Conductance, International Journal of Heat and Mass Transfer, Vol. 12, 1969, pp. 279-300

6. B. B. Mikic, Thermal Contact Conductance; Theoretical Considerations, International Journal of Heat and Mass Transfer, Vol. 17, 1974, pp. 205-214
7. A. W. Bush, R. D. Gibson and T. R. Thomas, The Elastic Contact of A Rough Surface, Wear, Vol. 35, No. 2, 1975, pp. 87-111
8. D. J. Whitehouse and J. F. Archard, The Properties of Random Surfaces of Significance in Their Contact, Proceedings of Royal Society of London, A316, No. 1524, 1970, pp. 97-121
9. S. Kucharski et al., Finite-Element Model for The Contact of Rough Surfaces, Wear, Vol. 177, 1994, pp. 1-13
10. E. J. Abott and F. A. Firestone, Specifying Surface Quantity-A Method Based on Accurate Measurements and Comparison, Mechanical Engineering, Vol. 55, 1933, pp. 569
11. J. Pullen and J. B. P. Williamson, On The Plastic Contact of Rough Surfaces, Proceedings of Royal Society of London, A, Vol. 327, 1972, pp. 159-173
12. M. Leung, C. K. Hsieh and D. Y. Goswami, Application of Boltzmann Statistical Mechanics in the Gaussian Summit-Height Distribution in Rough Surfaces, Journal of Tribology-Transactions of The ASME, Vol. 119, pp. 846-850, 1997
13. H. Ishigaki and I. Kawaguchi, A Simple Estimation of the Elastic-Plastic Deformation of Contacting Asperities, Wear, Vol. 54, 1979, pp. 157-164
14. H. A. Francis, Application of Spherical Indentation Mechanics to Reversible and Irreversible Contact between Rough Surfaces, Wear, Vol. 45, 1977, pp. 221-269
15. M. Leung, C. K. Hsieh and D. Y. Goswami, Prediction of Thermal Contact Conductance in Vacuum by Statistical Mechanics, Journal of Heat Transfer, Transactions of the ASME, Vol. 120, 1998, pp. 51-57
16. M. A. Kellow, A. N. Bramley and F. K. Bannister, The Measurement of Temperatures in Forging Dies, International Journal of Machine Tool Design and Research, 1969, Vol. 9, pp. 239-260
17. K. Nishino, S. Yamashita and K Torii, Thermal Contact Conductance under Low Applied Load in A Vacuum Environment, Experimental Thermal and Fluid Science, Vol. 10, 1995, pp. 258-271

18. Baltazar A, Rokhlin SI, Pecorari C, On the Relationship between Ultrasonic and Micromechanical Properties of Contacting Rough Surfaces, Journal of the Mechanics and Physics of Solids 50 (7): 1397-1416 JUL 2002
19. M. A. Lambet, E. E. Marotta, L. S. Fletcher, The Thermal Contact Conductance of Hard and Soft Coat Anodised Aluminium, Journal of Heat Transfer, Transactions of The ASME, Vol. 117, 1995, pp. 270-275
20. K. C. Chung, H. K. Benson and J. W. She-ffield, Thermal Contact Conductance of Ceramic Substrate Junctions, Journal of Heat Transfer, Transactions of The ASME, Vol. 117, 1995, pp. 508-510
21. M. R. Sridhar and M. M. Yovanovich, Thermal Contact Conductance of Tool Steel and Comparison with Model, International Journal of Heat and Mass Transfer, Vol. 39, No. 4, pp. 831-839, 1996
22. M. R. Sridhar and M. M. Yovanovich, Review of Elastic and Plastic Contact Conductance Models: Comparison with Experiment, Journal of Thermophysics and Heat Transfer, Vol. 8, No. 4, 1994, pp. 663-640
23. T. H. McWaid and E. Marschall, A Comparison of Elastic and Plastic Contact Models for The Prediction of Thermal Contact Conductance, Warme- Und Stoffubertragung, Vol., 28, 1993, pp., 441-448
24. M. A. Lambert and L. S. Fletcher, Review of The Thermal Contact Conductance of Junctions with Metallic Coatings and Films, Journal Thermophysics and Heat Transfer, Vol. 7, No. 4, 1993, pp. 547-554
25. K. E. Parmenter and E. Marschall, Influence of Surface Preparation on Thermal Contact Conductance of Stainless Steel and Aluminium, Experimental Heat Transfer, Vol. 8, 1995, pp. 195-208
26. M. Williamson and A. Majumdar, Effect of Surface Deformation on Contact Conductance, Transactions of The ASME, Journal of Heat Transfer, Vol. 114, 1992, pp. 802-810
27. C. W. Vigor, et al., A Thermocouple for Measurement of Temperature Transients in Forging Dies, Temperature, Its Measurement and Control Vol. 3, part 2, Reinhold, New York, 1961, pp. 625-630

28. L. D. Demidov, Method for An Experimental Determination of The Tool Temperature during Hot Forging, Kuznechno-Stampovochnoe Proizvod., No. 11, 1965
29. M. A. Kellow, et al., The Oxidation of Steel at High Temperature and Its Effect on Die Surface Temperature in Hot Forging, Proceedings of 17th MTDR Conference, 1977, pp. 335-346
30. T. A. Dean and T. M. Silva, Die Temperatures during Production Drop Forging, Journal of Engineering for Industry, Transactions of The ASME, 1979, Vol. 101, pp. 385-390
31. T. Altan and A. F. Gerds, Temperature Effects in Closed-Die Forging, ASM Technical Report No. C70-30.1, American Society for Metals, 1970
32. C. R. Boer and G. Schroder, Temperature in Die-Billet Zone in Forging, Annals of The CIRP 1981, Vol. 30, No. 1, pp. 153-157
33. P. Dadras and W. R. Wells, Heat Transfer Aspects of Non-Isothermal Axisymmetric Upset Forging, Journal of Engineering for Industry, Transactions of The ASME, 1984, Vol. 106, pp. 187-195
34. P. Dadras, et al., Thermal Effects in Hammer Forging, Proceedings of NAMRC XIV, Vol. 1, Society of Manufacturing Engineers, 1986, pp. 332-339
35. S. L. Semiatin, E. W. Collings, V. E. Wood and T. Altan, Determination of The Interface Heat Transfer Coefficient for Non-Isothermal Bulk-Forming Processes, Journal of Engineering for Industry, Transactions of The ASME, 1987, Vol. 109, pp. 49-57
36. A. N. Karagiozis and J. G. Lenard, Temperature Distribution in A Slab during Hot Rolling, Journal of Engineering Materials and Technology, Transactions of The ASME, Vol. 110, 1988, pp. 17-21
37. K. J. Stout and J. Sullivan, The Use of 3-D Analysis to Determine the Micro-Geometric Transfer Characteristics of Textured Sheet Surface through Rolling, Annals of The CIRP, Vol. 41, No. 1, 1992, pp. 621-624
38. Mitutoyo, Surface Roughness Measuring System Surface Texture Parameters, User's Manual. 1999.
39 T. Wanheim and N. Bay, A Model for Friction in Metal Forming Processes, Annals of The CIRP, Vol. 27, pp. 189-194, 1978

Appendix 4.1

Definition of the BRC of surface profile

The definition of bearing ratio (material ratio) curve requires a co-ordinate system, as shown in Fig. 4.1.1. The x-axis is in tangent to the lowest valley of the surface profile. y is an arbitrary distance perpendicular to the x-axis. A $0 \le y \le R_t$ represents a line parallel to the x-axis between the highest peak and the lowest valley. Thus, the surface profile would intersect this line at level y. Assuming that the intersected lengths of the line by surface profile are $x_1, x_2, \cdots, x_n$, as shown in Fig.4.1.1. X and Y are defined as

$$X = \frac{1}{L}\sum x_i \times 100\% \qquad (4.1\text{-}1)$$

$$Y = \frac{y}{R_t} \times 100\% \qquad (4.1\text{-}2)$$

X and Y would define a point (X,Y) on $X-Y$ plane at a intersection level y. y varies continuously from 0 to R_t. Thus, the locus of point (X,Y) is a continuous curve on $X-Y$ plane, as shown in Fig. 4.1.2. This curve is referred to as bearing ratio (material ratio) curve.

Appendix 4.2

The BRC and the surface parameters it represents

A4.2.1 Arithmetic deviation to mean line R_a

In order to show that bearing ratio curve presents the arithmetic deviation to mean line, the significance of surrounding area by bearing ratio curve should be analysed first.

A4.2.1.1 Area surrounded by bearing ratio curve

First, let us discuss what is the practical meaning of the surrounding area of the BRC and the co-ordinate axes (surrounding area only thereafter). Assuming that the surrounding area being A_b, referring to Fig.4.1.2, we have

$$A_b = \int_0^1 X dY \tag{4.2-1}$$

Substituting equations (4.1-1) and (4.1-2) into (4.2-1), it can be obtained

$$A_b = \frac{1}{LR_t}\int_0^{R_t}\left(\sum x_i\right)dy \tag{4.2-2}$$

Note that $\sum x_i$ is the sum of intersection segments at intersection level y. From Fig.4.2.1, it is understandable that the integration is the area surrounded by surface profile and x axis, as shown by the shadow area in Fig.4.2.1. Assuming that the area surrounded by surface profile is A_p,

$$A_p = \int_0^{R_t}\left(\sum x_i\right)dy$$

From equation (4.2-2)

$$A_p = LR_t A_b \tag{4.2-3}$$

Equation (4.2-3) shows that area surrounded by surface profile is proportional to that surrounded by the BRC with proportional coefficient LR_t.

A4.2.1.2 Surface roughness determined by the BRC

It can be shown in this section that surface roughness, according to its definition, can be determined by the BRC. First, the relative location of mean line in $X-Y$ plane (refer to Appendix 4.1) to the BRC can be determined. From the definition of mean line, its position can be determined by the condition of minimisation of the square deviation to mean line of the surface profile. Let's take the co-ordinate system in Fig. 4.2.3 as a reference. Assuming that the distance between mean line and x axis is y_0,

$$D = \int_0^L (y - y_0)^2 dx$$

The position of mean line is determined by the minimisation of D. Let,

$$\frac{\partial D}{\partial y_0} = 2\int_0^L (y - y_0)dx = 0$$

or,
$$y_0 = \frac{1}{L}\int_0^L y dx \tag{4.2-4}$$

or
$$Y_0 = \frac{y_0}{R_t} = \int_0^L \frac{y}{R_t} d\left(\frac{x}{L}\right) = \int_0^1 Y dX \tag{4.2-5}$$

where Y_0 is the relative position of mean line in $X-Y$ plane with respect to bearing ratio curve. It is easy to prove mathematically that line $Y = Y_0$ satisfies the definition of mean line to the BRC; the sum of squares of deviation of the BRC to line $Y = Y_0$ is minimum. Thus, it is referred to as the mean line to the BRC. Equation (4.2-5) shows that the relative position of mean line to the BRC can be determined like this: calculate the surrounding area of the BRC and draw a square with this area, and side-length 1 coinciding with X axis in $X-Y$ plane. Then the other side of the square is the position of the mean line, as shown in Fig.4.2.2. Or simply finding a parallel line to X-axis to enable the area, $S_{b\Delta}$, above this line to equal to the area, $S_{b\nabla}$, below this line, as shown in Fig.4.2.2, then, this line is the mean line relative to the BRC. Obviously in Fig.4.2.2 $S_{b\Delta}$ and $S_{b\nabla}$ can be written as

$$S_{b\Delta} = \int_{Y_0}^1 X dY \tag{4.2-6}$$

$$S_{b\nabla} = \int_0^{Y_0} (1 - X)dY \tag{4.2-7}$$

Substituting equations (4.1-1) and (4.1-2) into equations (4.2-6) and (4.2-7), transforming the integration variable, we have

$$S_{b\Delta} = \frac{1}{R_t L}\int_{y_0}^{R_t} \left(\sum x_i\right)dy \tag{4.2-8}$$

It is understandable that the integration included in equation (4.2-8) is the area surrounded by the surface profile above mean line. –refer to Fig.4.2.1. From equation (4.2-8)

$$S_{b\Delta} = \frac{1}{R_t L}\sum S_{i\Delta} \tag{4.2-9}$$

Similarly, $$S_{b\nabla} = \frac{1}{R_t L}\sum S_{j\nabla} \qquad (4.2\text{-}10)$$

Adding equation (4.2-9) and (4.2-10), from the definition of arithmetic deviation of surface profile to men line it can be obtained:

$$S_{b\Delta} + S_{b\nabla} = \frac{1}{R_t L}\left(\sum S_{i\Delta} + \sum S_{j\nabla}\right)$$

or $$S_{b\Delta} + S_{b\nabla} = \frac{1}{R_t}\frac{\sum S_{i\Delta} + \sum S_{j\nabla}}{L}$$

$$S_{b\Delta} + S_{b\nabla} = \frac{R_a}{R_t}$$

$$R_a = R_t\left(S_{b\Delta} + S_{b\nabla}\right) \qquad (4.2\text{-}11)$$

Equation (4.2-11) shows that bearing ratio curve with surface profile height contains all necessary information that evaluation of the surface roughness R_a requires. If the BRC and total height of the surface profile is known, then surface roughness is uniquely determined.

A4.2.2 Root-mean-square deviation determined by the BRC

Root-mean-square deviation R_q can also be determined by the BRC. From the definition of root-mean-square deviation,

$$R_q^2 = \frac{1}{L}\int_0^L (y - y_0)^2\, dx \qquad (4.2\text{-}12)$$

There are two approaches to compute the integration (4.2-12). One approach is shown in Fig. 4.2.3a and the other, in Fig. 4.2.3b. As shown in Fig. 4.2.3b, two lines parallel to x-axis are drawn, the distance between them being a small value dy. Thus, many small intersection-segments of these two parallel lines are obtained by the intersection of the surface profile. Using $x_1, x_2, \ldots, x_n$ denotes the projections of these small intersection segments at level y on x-axis, and using $x_1', x_2', \ldots, x_n'$ denotes the projections of those small intersection segments at level $y + dy$ on x-axis. Thus, we obtained the intersectional segment increment dx_k for the k^{th} peak

$$dx_k = x_k - x_k'$$

Sum up $$\sum dx_k = \sum (x_k - x_k')$$

From the definition of root-mean-square deviation

$$\begin{aligned} dR_q^2 &= \frac{1}{L}\left(\sum dx_k\right)(y - y_0)^2 \\ &= \frac{1}{L}(y - y_0)^2\left(\sum dx_k\right) \end{aligned} \tag{4.2-13}$$

Paying attention to the definitions (4.1-1) and (4.1-2) and equation (4.2-5), we have

$$\begin{aligned} dX &= \frac{1}{L}\sum dx_k = \frac{1}{L}d\left(\sum x_k\right) \\ y - y_0 &= \frac{1}{R_t}(Y - Y_0) \end{aligned} \tag{4.2-14}$$

Note that when y varies from R_t to 0 in Fig. 4.2.3b, $\sum x_k$ varies from 0 to L. Substituting equation (4.2-14) into equation (4.2-13) and transforming the integration limits, we can obtain

$$R_q^2 = R_t^2 \int_0^1 (Y - Y_0)^2 dX$$

or $$R_q = R_t \sqrt{\int_0^1 (Y - Y_0)^2 dX} \tag{4.2-15}$$

Equation (4.2-15) shows that the product of root-mean-square deviation of the BRC to Y_0 and R_t is the root-mean-square deviation of the surface profile to mean line. Thus, bearing ratio curve and surface profile height have all necessary information for the determination of root-mean-square deviation of the surface profile.

Summarising the above analysis, bearing ratio curve and total height of the surface profile can be used for the determination of the surface texture characters

- mean line position,
- intersection area at any level,
- surface roughness,
- and root-mean-square deviation of the surface profile.

BRC is one of the most important characters of a random surface texture.

A4.2.3 The EBRC

Although BRC and surface profile height can be used to present the basic random characters of a surface profile, the surface parameters determined by the BRC are proportional to the surface parameters of the actual surface profile; the proportional coefficient is the total height of the surface profile. Therefore, the form of the BRC can not be used directly to construct an imaged surface asperity; the BRC is a pure number (ratio), describing a surface without dimension. It should be expanded to enable the basic surface parameters it presents exactly the same as those of the surface profile.

Assuming that we have already obtained the BRC of a surface profile, as shown in Fig.4.2.2. Now let the ordinate Y of the BRC in $X-Y$ plane multiplied by the total height, R_t, of the surface profile and abscissa X multiplied by an *arbitrary* length $\bar{L}>0$. Thus, a curve similar to the BRC, referred to as **expanded bearing ratio curve (EBRC)**, as shown in Fig.4.2.4 in $\bar{x}-\bar{y}$ co-ordinate system, is obtained. The EBRC is different from the BRC in dimensions. The BRC is without dimension, the ordinate and abscissa of which are both pure numbers; while the ordinate and abscissa of the EBRC have the dimension of length.

Obviously, the relationship between Fig.4.2.4 and Fig.4.2.2 can be expressed as

$$\begin{aligned} \bar{y} &= R_t Y = y \\ \bar{x} &= \bar{L}X = \frac{\bar{L}}{L}\sum x_i \end{aligned} \tag{4.2-16}$$

The relative position of mean line to the EBRC, as can be shown, is exactly y_0, the mean line position of the surface profile. The area above the mean line, labelled as $\bar{S}_{b\Delta}$, is

$$\bar{S}_{b\Delta} = \int_{y_0}^{R_t} \bar{x}\, d\bar{y} \tag{4.2-17}$$

Considering equation (4.2-16)

$$\bar{S}_{b\Delta} = \frac{\bar{L}}{L}\int_{y_0}^{R_t} \sum x_i\, dy = \frac{\bar{L}}{L}\sum S_{i\Delta} \tag{4.2-18}$$

From equation (4.2-18), $\overline{S}_{b\Delta}$ is proportional to the area surrounded by surface profile peaks above mean line, with a proportional coefficient dependent on $\overline{L}$.

Similarly,

$$\overline{S}_{b\nabla} = \frac{\overline{L}}{L}\int_0^{y_0}\sum x_i dy = \frac{\overline{L}}{L}\sum S_{J\Delta} \tag{4.2-19}$$

According to the definition of the surface roughness, the EBRC defines a surface with arithmetic mean deviation

$$\begin{aligned}\frac{\overline{S}_{b\Delta}+\overline{S}_{b\nabla}}{\overline{L}} &= \frac{1}{\overline{L}}\left(\frac{\overline{L}}{L}\sum S_{I\Delta}+\frac{\overline{L}}{L}\sum S_{J\nabla}\right)\\ &= \frac{\sum S_{I\Delta}+\sum S_{J\nabla}}{L} = R_a\end{aligned} \tag{4.2-20}$$

Therefore, the EBRC represents exact the same surface roughness as that of the surface profile. Attention should be paid to the fact that the determination of surface roughness by the EBRC is *without* relation to the length of $\overline{L}>0$. Therefore, $\overline{L}$ can be arbitrary.

Now let's define the mean-square deviation R_q that the EBRC represents:

$$\begin{aligned}\frac{1}{\overline{L}}\int_0^{\overline{L}}(\overline{y}-\overline{y}_0)^2 d\overline{x} &= \frac{1}{\overline{L}}\int_0^{\overline{L}}(R_t Y - R_t Y_0)^2 d(\overline{L}X)\\ &= R_t^2\int_0^1 (Y-Y_0)^2 dX\\ &= R_q^2\end{aligned} \tag{4.2-21}$$

where the first step refers to equation (4.2-16) and second step to equation (4.2-15). Equation (4.2-21) shows that the mean-square deviation that the EBRC represents is also exactly the same as that of the surface profile. The above discussion results in:

If the ordinate of the bearing ratio curve is multiplied by total height R_t, the surface roughness and root-mean-square deviation represented by this expanded bearing ratio curve are exactly the same as those of the surface profile, regardless of X direction of the bearing ratio being expanded or not, or how much having been expanded.

Summarising the above analysis, the EBRC represents the same

- mean line position,
- intersected area at any intersectional level,
- surface roughness,
- and root-mean-square deviation

as those of the actual surface profile. Therefore, the form of an EBRC can be applied to construct the form of an equivalent asperity which represents the basic geometric characters of an isotropic random surface.

Appendix 4.3

The equivalent asperity based FE model for determining friction coefficient

A possible application of the equivalent asperity FE model is to predict the contact area ratio and further to predict the friction coefficient between a rough surface and a smooth rigid plane. Wanheim and Bay [39] presented the model. Slipline field method was used to determine the real contact area; therefore, the rough surface asperities were simplified as a simple two-dimensional, infinitely long ridge asperity. The friction factor on the actual contacted area is assumed constant. Thus, friction coefficient between a rough surface and a plane is a function of the contact area ratio and the assumed friction factor. Obviously, contact area ratio can be also determined by the FE simulation model established in this research. The basic assumptions used in the FE simulation model is more realistic than those used in [39], and equivalent asperity is a more suitable representation of a real surface than a simple two-dimensional infinitely ridge asperity is. Therefore, the established FE simulation model can be applied to predict friction coefficient between a rough surface and a smooth rigid plane more realistically.

Besides, from the surface measurement results in this research, contact area ratio not only related to the equivalent asperity, but also the surface macro-irregularities.

Therefore, if friction factor on contacted area is constant, friction coefficient between the surface and the rigid plane will be closely related to the rough surface texture. Even lubrication conditions are the same for two rough surfaces with the same material and same surface roughness, the friction coefficient may be different due to difference in surface texture, in particular the surface macro-irregularities which may lead to quite different contact area ratio. Measurements of surface friction coefficients, in these two cases, are surely different. This may be an explanation why friction coefficient is elusive and changeable even for the same lubrication condition. Random surface texture has a strong influence on friction coefficient; therefore, friction coefficient, on some extent, has also a random characteristic.

Further research is required for these applications of the equivalent asperity, based on FE simulation model established for surface deformation prediction.

Chapter Five

FE simulation of heat transfer at material-contact interface

5.1 Summary

Different thermal models have been reviewed. Most of these thermal models were validated by experimental data at low nominal interfacial pressures (<10 MPa). These data were found to be inapplicable to cold forming operations. Thermal contact conductance at high nominal interfacial pressure has been evaluated using calibration methods. These methods consider thermal contact conductance as a constant regardless of surface texture or interfacial pressure. Surface texture and nominal interfacial pressure play an active part in the heat transfer between tool and billet in cold forming.

An FE simulation model based on the equivalent asperity (refer to Chapter 4) was established; two thermal models, an area ratio thermal model and a local thermal model are presented. The equivalent asperity, representing the surface texture, was based on surface measurements. The thermo-mechanically coupled contact between an elastic plane and an isotropic and uniform rough surface was simulated to derive the area ratio and local interfacial pressure. Further, thermal contact conductance was derived using these thermal models.

Parameters involved in the thermal models were determined by the correlation between h-values computed from experiments and those derived by FE simulations. Thermal contact conductance was shown to be varying linearly with the nominal interfacial pressure up to 0~180 MPa in experiments; this was confirmed by the FE simulations. Fine textured specimens with small surface macro-irregularities results

in higher h-values and greater slope of the h-value relative to the nominal interfacial pressure; this is compared well with experimental data. The typical h-value at a nominal interfacial pressure of 200 MPa changes from 25~160 $kWm^{-2}K^{-1}$ with a change of the initial surface texture from $R_a = 0.74 \sim 0.97$ μm to $R_a = 3.51 \sim 4.97$ μm. Surface macro-irregularities, asperity flow strength and surface measurement accuracy are the main factors influencing the accuracy of FE simulation of the h-value.

5.2 Nomenclature

a	Equivalent radius of a surface asperity	μm
c	Specific heat	$Jkg^{-1}K^{-1}$
C	Constant	
C_a	Constant coefficient in area thermal model	$kW\,m^{-1}K^{-1}$
C_c	Dimensionless and relative h-value	
A	Real contact area	μm^{-2}
E	Young's modulus of material	MPa
h	Thermal contact conductance	$kWm^{-2}K^{-1}$
H_c	Micro-hardness of softer material in contact	MPa
m	Exponential coefficient	
n	Mean slope of surface profile	
k	Conductivity of material	$W\,m^{-1}K^{-1}$
p	Local interfacial pressure	MPa
P	Nominal interfacial pressure at interface	MPa
Q	Sum of squares	$\left(kWm^{-2}K^{-1}\right)^2$
q	Heat flux density	Wm^{-2}
r	Area ratio	
R_a	Surface roughness	μm
R_t	Total height of the surface profile	μm
T	Temperature	$^{\bullet}C$

t	Time	s
x, y	Co-ordinate used to describe the equivalent asperity or nodal co-ordinate	
δ	Thickness of interfacial layer	mm
θ	Density of contact spots	mm^{-2}
ς	Exponential constant in area ratio h-value model	
ρ	Mass density	$kg\,m^{-3}$
λ	Small constant in area ratio h-value model, $\lambda > 0$	μm
ΔT	Temperature drop	$^{\bullet}C$

Subscripts

0	Initial or critical
1	Body 1
2	Body 2
a	Area thermal contact conductance model
e	Experiment
f	FE simulation
i	The i^{th} term, or the i^{th} node on the equivalent asperity profile
l	Local thermal contact conductance model
max	Maximum
n	Nominal
p	Asperity
t	Tool
s	Specimen

Superscripts

ψ	Exponential coefficient in exponential correlation model
ν	Exponential constant in area ratio thermal model
γ	Exponential constant in area ratio thermal model
β	Exponential constant in area ratio thermal model
m	Exponential constant number in local thermal model

Example: A_{pn} : the nominal asperity contact area, A_p : Asperity contact area.

5.3 Glossary

Disordered area: A one-dimensional heat flow field through a contact interface will not be one-dimensional near the interface due to the contact surfaces asperities; there is a small area near the interface in which the heat flow is three-dimensional. This small area is referred to as disordered area.

Cross-sectional area: When a surface asperity is intersected by a perfectly flat plane, the cross-sectional area of the asperity at the intersected depth is defined as cross-sectional area of the asperity.

5.4 Introduction

Thermal contact conductance (h) is of significance in many engineering fields. It defines the heat exchange pattern between bodies that are in close contact. In electronics, thermal contact conductance is investigated with a view to improving heat dissipation when devices are in operation. In the nuclear engineering industry, thermal contact conductance is studied for the purpose of maximising heat exchange thus improving the usage efficiency of nuclear reactions. In metal forming, thermal contact conductance is researched in order to improve the understanding of the mechanical and thermal behaviour of both, the work- and tool-materials, during forming. This would enable a more accurate prediction of the form, geometric dimensions and the microstructure of components.

Thermal model is one of the sub-models of a model of heat transfer between two contact surfaces [1]. The thermal model defines the thermal contact property at the interface, which governs the heat transfer across the interface. Thermal contact conductance is this thermal property. Different thermal models have been presented in literature.

5.4.1 Asperity-based models

The most widely cited thermal model was presented by Cooper et al. [2] and is expressed as

$$h = \frac{2\left(k_s^{-1} + k_t^{-1}\right)^{-1} \theta\alpha}{\left(1 - \sqrt{A_p / A_{pn}}\right)^{1.5}} \tag{5-1}$$

where A_p / A_{pn} is referred to as the ratio between the real contact area to nominal contact area – the *area ratio*. Each surface geometrical model requires a different computational approach for determining the real contact area, contact spot density and the contact radius [3]; each thermal model has been based on a different surface geometry. These models have been referred to as a family of asperity-based models due to the logical similarity of the surface deformation sub-models [5~6].

5.4.2 Dimensionless thermal models

Dimensionless values were considered to be of general importance; these prompted the development of models by Majumdar, Bhusha [7], Mikic [4], and Yovanovich and Hegazy [8]. It was assumed that

$$\left(A_p / A_{pn}\right) = \left(P / H_c\right) \tag{5-2}$$

Antonetti [9] and Hegazy [10] suggested a dimensionless value

$$C_c = \left(R_a / \sqrt{n_t^2 + n_s^2}\right)\left[h\left(k_s^{-1} + k_t^{-1}\right)\right] \tag{5-3}$$

which was suitable for replacing thermal contact conductance. The relationship between equations (5-2) and (5-3) was established by referring to equation (5-1). Thus, the h-value was expressed as a function of nominal interfacial pressure. These led to the development of different dimensionless forms of thermal models. In the different thermal models mentioned above, the surface deformation was either elastic, plastic, or elastic-plastic; these models were converted into the corresponding dimensionless thermal models [4~6].

5.4.3 Exponential correlation models

Another type of thermal model is referred to as exponential correlation models, in which h-value is considered as the exponential function of the nominal interfacial pressure. The exponential correlation models were neither the direct results of theoretical analysis, nor the outcome of experimental data correlation; instead, they were statistical and numerical correlation of the thermal models [11]. The general expression for the exponential correlation model is:

$$h = CP^{\psi} \tag{5-4}$$

The constant C was referred to the surface profile, contact conditions and the matched materials. Exponential coefficient ψ is either a constant or conditionally constant, and was a function of surface profile, contact conditions and the coupled materials. Materials with different contact conditions led to different values of C and ψ. Several research programs compared experimental results with equation (5-4) [12-14]. It is worth emphasising that the range of exponential coefficient ψ is small, $\psi \approx 0.94 \sim 0.95$ [11]. Thus, the h-value is approximately *a linear function of the nominal interfacial pressure*. These validation experiments were, however, conducted at low interfacial pressures, of the order of 10% of yield strength of the rough surface material [11].

5.4.4 Value of h under high interfacial pressure – The calibration method

The thermal models discussed above were validated for low interfacial pressures. Thermal contact properties at low interfacial pressure are not relevant to metal forming operations. Investigations of h under high interfacial pressure were conducted using the calibration method, which does not require a thermal model; the research conducted by Kellow et al. [15,16] was not based on either of the thermal models referred to. As shown in Fig. 5.1, Kellow et al. considered two contact bodies, body 1 and body 2, with different initial temperatures T_{10} and T_{20} and a contact layer with thickness δ, without considering the influence of the contact surface texture. A transient temperature field is thus formed. Kellow et al. assumed that

- the transient heat flow field is one dimensional near the contact interface;
- the interface layer has no thermal capacity of its own;
- the temperature drop in the interface layer is linear;
- and the temperature of some points within the interface layer remains constant during heat transfer.

Based on these assumptions it was obtained that:

$$\frac{T_1 - T_{10}}{T_{20} - T_{10}} = \frac{b_2}{b_1 + b_2}\left\{\left[erfc\left(\frac{x}{2\sqrt{K_1 t}}\right)\right] - \left[\exp\left(\frac{2hx}{b_1\sqrt{K_1}} + \frac{4h^2 t}{b_1^2}\right)\right]\cdot\left[erfc\left(\frac{x}{2\sqrt{K_1 t}} + \frac{2h\sqrt{t}}{b_1}\right)\right]\right\} \tag{5-5}$$

where x is the co-ordinate system shown in Fig. 5.1, and $b = \sqrt{k\rho c}$, $K = k/(\rho c)$. The calibration method was used to determine transient values of thermal contact conductance. Initially, several calibration curves of T_1 at a given location vs. t for different values of h were derived using equation (5-5); by measuring T_1 curve at the location against time t and comparing this with the calibration curves, the best match provided an indication of the prevailing h-value. This transient temperature based measurement assumes that the value of h remains constant during thermal contact.

Calibration curves can be plotted by either analytical method, as Kellow et al. illustrated [15,16], or by numerical methods. Dadras and Wells [17], Semiatin et al. [18], and Li and Sellars [19] presented different calibration methods. Several numerical techniques were used to simulate the temperature-time distribution for different values of h. These calibration curves were then compared to the results of experiments, allowing the allocation of a unique h-value. The least-squares-method was applied by Nshama, Jeswiet and Oosthuzien [20] and Hu, Brooks and Dean [21]. An improved approach was developed by Malinowski [22] to evaluate the value of h as a function of interfacial pressure, time and temperature, using the least-squares-method. However, the influence of surface texture during contact was ignored due to the limitation of both, the experimental equipment and FE simulation.

There is an electrical analogy in thermal contact resistance [23]; the approach for measuring electrical resistance was also used for the evaluation of h-value. The measured value of electric resistance can be translated into heat transfer resistance using the Wiederman-Franz law [23]. Shamasundar [24] used the measurement of electrical resistance in high-pressure contact to compute the value of h; Fig. 5.2 shows the experimental configuration. However, the electric resistance of wires and the junctions between wires and die surfaces are also included in the measurement, resulting in a confused interpretation of the value of h.

Several attempts have been made to measure surface temperature by using surface thermocouples. These have already been discussed into details in Chapter 3.

5.4.5 Conventional thermal models

The problem common to conventional methods of computing h-value is that these relied on cross-sectional areas of asperities instead of the real contact area and did not refer to plasticity considerations. The conventional thermal models compute h values quite accurately for low interfacial pressures. However, there are few applications for these findings in metal forming. It can be concluded that the main approaches used for computation of h-values at high interfacial pressure are the calibration methods [17-22]. The h-value was considered a constant for calibration methods. An exception is the approach adopted by Malinowski [22] who had obtained a relationship between h, interfacial pressure and temperature by finite element method, using an iterative procedure. However, all calibration or reverse methods did not include the influence of surface texture on h-value for high interfacial pressures.

In this research, thermal FE models, based on the concept of the equivalent asperity, are presented; the real contact area and local interfacial pressure can be defined using elastic-plastic FE analysis of the micro-deformation of surface. Thus, the plastic deformation of surface will be included in the evaluation of the real contact area; the real contact area and local interfacial pressure, therefore, can be further used to define the thermal contact conductance instead of the conventional cross-sectional area of asperities.

5.5 FE simulation model

5.5.1 Assumptions

Generally, the h-value is a function of surface texture, interfacial pressure, contact temperature, lubrication condition and the contacting materials. The test material used in the experimental programme was Ma8, and N910 was used for tools. The temperature of the main heater was set at $200^{\circ}C$ and the inner cooler at $10^{\circ}C$. – refer to Fig. 3.3. When these settings prevailed, the specimen temperature was about 90~95 $^{\circ}C$, depending on the specimen surface texture and the nominal interfacial pressure. Contact temperature can be considered constant in this investigation. Based

on these simplifications, the h-value is assumed to be a function of surface texture and interfacial pressure.

The FE analysis will be based on the following assumptions.

(1) Value of h is a function of surface texture and interfacial pressure at constant contact temperature.

(2) Contact is between an elastic perfect tool surface and a specimen surface with isotropic, uniform surface texture.

(3) The surface texture can be represented by the equivalent asperity.

(4) The compression of the active surface of the specimen can be modelled by considering the elastic-plastic deformation of the equivalent asperity.

(5) A cylinder parallel to the axis of the specimen before contact remains a cylinder after surface deformation.

(6) Surfaces are not lubricated and free of surface contamination and oxidation.

Assumption (1) allows a variety of interfacial pressures and surface textures to be considered in the FE simulation. Assumptions (2) and (3) provide the conditions for establishing the geometric model for FE simulation. Assumption (4) enables the representation of the surface with an equivalent asperity and the use of FE simulation to evaluate the real contact area and local interfacial pressure. The validity of this assumption depends on the assumed effective diameter of the equivalent asperity. It was established that surface parameters such as roughness and root-mean-square deviation do not refer to the diameter of the equivalent asperity. Thus, if surface texture was to be analysed, the diameter of equivalent asperity would not feature in the analysis. However, in the FE simulation of thermal contact conductance, it is recognised that the interfacial pressure is a dominant factor. The local interfacial pressure would depend on the diameter of the equivalent asperity.

Fig. 5.3a shows an equivalent asperity with diameter D, supported by an infinitely long cylinder with the same diameter, while Fig. 5.3b shows one with a diameter $5D$. If both equivalent asperities were compressed by a rigid/elastic plane to the same extent a, a greater plastic strain would be induced in the case shown in Fig. 5.3a; consequently, the local interfacial pressure would be also different. Therefore,

choosing a suitable diameter for the equivalent asperity is a key-step towards establishing an equivalent asperity.

The Mean Spacing is the mean distance from peak to peak of a surface profile. If the evaluation length. –the scan length in surface measurement, is much larger than the mean spacing, the latter can be considered the mean width occupied by each asperity; therefore, mean spacing can be regarded as the mean diameter of the asperities. Finally, assumptions (5) and (6) establish the definition of the boundary conditions of the FE model.

5.5.2 Mesh model of FE simulation

Dimensions of the tool and specimen used are shown in Figs. 5.4a~5.4b. The geometry of the FE model consists of three parts, an upper elastic tool cylinder, an equivalent asperity and a substrate cylinder supporting the equivalent asperity, as shown in Fig. 5.5. The diameters of cylinders and the asperity are the mean spacing of the surface profile, obtained from surface measurements on the specimen.

During mechanical contact of upsetting, the interfacial pressure would be higher at the rim than at the centre, if friction exists [31]. This would be the case without considering surface deformation. For real surface textures, the local plastic deformation of the surface asperities will weaken this "end effect". The nominal interfacial pressure is, therefore, assumed uniform; or the nominal interfacial pressure is considered as the mean actual interfacial pressure. Further, the dimensions of contact bodies are infinite in comparison with the dimensions of equivalent asperity. Thus, the FE simulation model can be regarded to be axisymmetric with reference to mechanical, geometrical and in thermal aspects. The geometry and mesh model for FE simulation is shown in Fig. 5.6. Parameter S is the mean spacing of the surface profile, and R_t is the total height. The height of the cylinder from the upper tool was defined as twice of the mean spacing; other dimensions and the virtual cylinder for the interaction between asperities have been analysed in Chapter 4.

The mesh of the equivalent asperity before contact is shown in Fig. 5.7. The interaction between asperities during thermal and mechanical contact is shown in Fig. 5.8, as "A". Had the virtual cylinder not been incorporated, the material would flow beyond the virtual cylinder and interference between material in neighbouring asperities would occur.

Finally, equivalent asperity is defined to represent an isotropic and uniform surface texture without macro-irregularities; therefore, the influence of surface macro-irregularities is not included in the following FE simulation.

5.5.3 Thermal models used in FE simulation

Two thermal models were established. Thermal contact conductance is regarded as a function of contact area ratio in the first thermal model while in the second, the heat flux density through an interface is assumed to be a function of location at the interface and determined by the local interfacial pressure. The latter presents a new concept of local thermal contact conductance; local thermal contact conductance determines the heat flux density at a point at interface.

5.5.3.1 Thermal contact conductance as a function of area ratio

It is assumed that thermal contact conductance can be expressed by the function:

$$h = \frac{C_a r^{\nu}}{S\left(1 - r^{\beta}\right)^{\gamma} + \lambda} \tag{5-6}$$

where λ is a small value (>0) with length dimension and C_a is constant coefficient with dimension of conductivity.

Parameters λ and C_a are important to the simulation of thermal contact conductance. For high interfacial pressure, the real contact area may be assumed to approximate to the nominal surface area. Therefore, area ratio $r = 1$ and

$$h_{\max} = \frac{C_a}{\lambda}. \tag{5-7}$$

Expression (5-7) indicates that under high nominal interfacial pressures thermal contact conductance is a constant instead of infinity as assumed in earlier models (5-

1) [2]. This assumption has yet to be confirmed experimentally. Infinite thermal contact conductance results in zero thermal resistance implying that the contact interface does not exist in a thermal sense. The value of h prevails as in equations (5-6) and (5-7). Both, the temperature drop and thermal contact conductance are nearly constant, instead of infinity, with increasing interfacial pressure up till a saturation level. Unfortunately, this study [29] failed to specify the critical value of pressure beyond which the thermal contact conductance remains constant.

When interfacial pressure is high, area ratio r closes to 1 and equation (5-6) is reduced into equation (5-7), regardless of initial surface texture, and the thermal contact conductance closes to a constant defined by equation (5-7). Therefore, the assumption in equation (5-6) that constant thermal contact conductance is activated at high interfacial pressure would imply that thermal contact conductance at high interfacial pressure is a function of contact materials and temperature, and is independent of surface texture ($r = 1$).

The difference between conventional thermal models (5-1) and that proposed by equation (5-6) is that the former predicts that perfect contact results in zero thermal contact resistance, while equation (5-7) implies a constant thermal resistance. Regardless, the task of validating the approach experimentally would be difficult. This arises from the difficulty of measuring the temperature drop accurately; this difficulty increases with the interfacial pressure and improved surface texture. However, it has been shown by the "transient method" that thermal contact conductance acquires a constant value at high interfacial pressures [29]. Thermal model (5-6) is referred to as the *area ratio thermal model* in the subsequent analyses.

Mean spacing is a key component of the thermal model; finer surfaces have smaller mean spacing S. Therefore, greater thermal contact conductance would occur for finer surfaces by the proposed thermal model. This is practical and has been shown by the experimental investigation.

The following text compares the area ratio model (5-6) with the traditional thermal model (5-1). When the equivalent asperity is used to represent the surface texture, the contact spot density θ in the thermal model (5-1) is

$$\theta = \frac{1}{\frac{\pi}{4}S^2} \tag{5-8}$$

The area ratio r is $$r = \frac{\pi a^2}{\frac{\pi}{4}S^2} = \left(\frac{2a}{S}\right)^2$$

Therefore $$a = \frac{S}{2}\sqrt{r} \tag{5-9}$$

Substituting equation (5-8) and (5-9) into equation (5-1)

$$h = \frac{\frac{4}{\pi}\left(k_s^{-1} + k_f^{-1}\right)^{-1}\sqrt{r}}{S\left(1-\sqrt{r}\right)^{1.5}} \tag{5-10}$$

Comparing equations (5-10) and (5-6), the area ratio thermal model is equivalent to the traditional thermal model (5-1) when nominal interfacial pressure is low. In fact, for low nominal interfacial pressure, $r \approx 0$ and the small value of λ can be ignored. However, parameters C_a, β, γ and ν would have to be determined from experimental data.

5.5.3.2 Thermal contact conductance as a function of local interfacial pressure

Heat flux density through a contact interface may be a function of location due to the non-uniform distribution of the local interfacial pressure. Therefore, thermal contact conductance can be regarded as a function of the local interfacial pressure. Thermal contact conductance at the point where materials contact is referred to as *local thermal contact conductance* (local h-value). Heat flux through a given contact area is the integration of heat flux density with respect to the contact area, while the heat flux density is defined by the local thermal contact conductance. Local thermal contact conductance is defined as a function of contact materials, local interfacial pressure, and does not depend on surface texture or other nominal surface contact parameters. Local h-value is a thermal contact property of the contacting materials.

In particular, heat flux through a contact asperity can be considered as an integration of heat flux density with respect to the contact area. From this point of view, the area ratio thermal model is a macro-level consideration, while the local thermal model is defined in micro-level.

By using h_l to denote local h-value, it is assumed that h_l is the polynomial function of local interfacial pressure, i.e.,

$$h_l = \begin{cases} \sum C_i (p/p_0)^i & p < p_0 \\ \sum C_i & p \geq p_0 \end{cases} \qquad (5\text{-}11)$$

For easy of application, only one term will be used in FE simulations, i.e.,

$$h_l = \begin{cases} C_l (p/p_0)^m & p < p_0 \\ C_l & p \geq p_0 \end{cases} \qquad (5\text{-}12)$$

Heat transfer between two contact surfaces in a small contact area is closely related to the mean distance between the two surfaces in the contact area. This distance depends on the local interfacial pressure. It is assumed that this mean distance is greater than the distance between molecules inside the corresponding solid, regardless of the local interfacial pressure. This is assumed to apply to most metal materials. Therefore, the heat resistance between two contact surfaces is greater than zero. Thermal models (5-11) and (5-12) are based on this assumption; there is a critical value of the local interfacial pressure, below which the local h-value will increase with the local interfacial pressure, and beyond which the local h-value is constant. In Fig. 5.9, the solid line shows the assumed variation of the local h-value, and the dashed line shows the simplified form of this variation (5-12). This thermal model, (5-11) or (5-12), is referred to as *local thermal model.*

5.5.4 Materials

Tools were manufactured from N910 that has a Young's modulus 210 *GPa* and a Poisson's ration of 0.3. Specimens were made from Ma8 steel with a Young's modulus 210 *GPa* and Poisson's ratio of 0.3. Constitutive equation and thermal properties are defined in Section 3.6. It should be noted that the material property of

the asperities of a specimen might be different from that of substrate due to surface work-hardening during finish-EDM machining. The actual material property of asperity remains unknown. It is assumed that the material properties of asperities and substrate are the same.

5.6 FE simulation procedures

The procedure for each FE simulations of thermal contact conductance is exclusive to the thermal models.

5.6.1 FE simulation procedure for area ratio thermal model

When area ratio thermal model (5-6) is used, only the area ratio has to be predicted by FE simulation; therefore, the FE model is used to simulate mechanical contact; elastic-plastic displacement FE analysis was applied. The nodal co-ordinates of the deformed mesh define the profile of the equivalent asperity after deformation. Thus, by comparing the ordinate of a node on the deformed equivalent asperity profile with that of the tool surface nodes, the contact condition can be established. A contact node on the equivalent asperity profile implies an annular contact area. The sum of the areas of all annular contact areas is the real contact area. Therefore, the area ratio can be defined by

$$r = \frac{4\sum\left(x_{i+1}^2 - x_i^2\right)}{S^2}. \qquad (5\text{-}13)$$

in which x_i is the i^{th} contact node on the equivalent asperity profile. An area ratio corresponds to a nominal interfacial pressure; thus, the area ratio is defined as a function of the nominal interfacial pressure; this function is defined rigorously by FE simulation of mechanical contact. Substituting equation (5-13) into the thermal model (5-6), the corresponding thermal contact conductance can be simulated and expressed as the function of the nominal interfacial pressure.

However, the constants and exponential coefficients included in the area ratio thermal model (5-6) should be determined to enable thermal contact conductance simulation. These thermal model constants were determined by correlating the h-values computed from experiments (refer to Chapter 3) and those derived from the

thermal model (5-6), combined with FE simulations. The least-squares-method can be used to determine these constants. Using Q denotes the sum of squares of the difference of h-values,

$$Q = \sum \left(h_e - h_f\right)^2 .$$

Minimisation of Q leads to

$$\frac{\partial Q}{\partial C_a} = 0; \frac{\partial Q}{\partial \nu} = 0; \frac{\partial Q}{\partial \lambda} = 0; \frac{\partial Q}{\partial \beta} = 0; \frac{\partial Q}{\partial \gamma} = 0 \qquad (5\text{-}14)$$

Equation (5-14) can be used to obtain the constants in area ratio thermal model (5-6) enabling best correlation of h-values between experiments and FE simulations. However, in comparison to equation (5-6), expression (5-14) is a nonlinear simultaneous equation group with five unknowns. The reliability of solutions of

Table 5.1 Constants used in thermal models

Local thermal models			Area ratio thermal models	
m	$C_l\left(kWm^{-2}K^{-1}\right)$	$p_0\left(MPa\right)$	$C_a\left(Wm^{-1}K^{-1}\right)$	$\lambda\left(\mu m\right)$
1	1020.0	1000 *	0.35	0.27
2	1184.0	1200	0.31	0.25
3	1200.0	1000	0.37	0.31
4	1058.9	950	$\nu = 0.5; \beta = 0.05;$	
6	1065.8	950	$\gamma = 1.5$	

*Reference for computation

these depends on the accuracy of the experimental data; the h-values computed from experiments performed under high interfacial pressures would be required in order to determine the unique parameters C_a and λ. A trial-and-error approach may be necessary to define the values of ν, β, γ, λ and C_a. From experimental data in Chapter 4, the FE simulations of surface deformation, and the observation of the contact marks on the specimen surfaces, a few specimens, such as 2.0-C, 2.5-D and 3.0-D and 4.0-D (refer to Figs. 4.18, 4.21, 4.24 and 4.27) appear to be among those with minimal surface macro-irregularities. The experimental data for these specimens were used to determine the parameters ν, β, γ, λ and C_a which are shown in Table 5.1.

$\nu = 0.5$ is an indication that r^{ν} is analogous to the radius parameter a in conventional thermal models (5-1). However, $\beta = 0.05$ does not match the previously adopted value. It is difficult to determine a unique combination of C_a and λ which describes the thermal contact behaviour under high interfacial pressure. However, it was established that different combinations of C_a and λ, which are derived from different specimens, can be used to simulate the h-values for interfacial pressures of less than 180 MPa. The following simulation results are based on parameters $C_a = 0.35\ (Wm^{-1}K^{-1})$ and $\lambda = 0.27\ (\mu m)$. There is no obvious difference by using other combined parameters.

Experimental data of which specimen is used to determine the required thermal model constants is not important; the important aspect is that the macro-irregularities of the chosen specimens should be as small as possible. Theoretically and experimentally, if data of a specimen without macro-irregularities is used to determine a set of thermal model constants, this set of data would be also applicable to other specimens. Surface measurements show that mean spacing of F-scaled specimens (refer to Table 3.1) is about 140~170 μm, about 5~6 times of the mean spacing of A-scaled specimens (22~26 μm). The thermal contact conductance experiment shows that h-values of A-scaled specimens are almost 5 times of those of F-scaled specimens. Therefore, h-value is almost inversely proportional to mean spacing of surface profile of specimens, i.e.,

$$h \propto \frac{1}{S}$$

This relationship is applicable to all specimens and all specimens have an approximate proportional coefficient which is a function of interfacial pressure or area ratio, if the influence of macro-irregularities is not included. It seems that the acquired experimental data pattern can be described in this way. This is just what has been shown by the presented area ratio thermal model (5-6) if the small constant λ is neglected. Due to this numerical relationship between experimental data and the presented thermal model, experimental data of any specimen can be applied to determine the constants in the thermal model, as long as the macro-irregularities of

the specimen is small, and the constants so determined would be applicable to other specimens.

It is worth pointing out that parameters β, C_a and λ are related each other; different combination of them can be used to correlate the experimental results well. Therefore, the parameters shown in Table 5.1 are not unique at current experimental conditions and experimental data; uniquely determining these parameters depends on experimental data at higher interfacial pressure.

5.6.2 FE simulation procedure using the local thermal model

Thermal contact conductance at a macro-level would be of greater interesting in engineering applications. Therefore, the local h-value should be integrated. For the integration of local h-value, the parameter involved in the local thermal model should be defined by correlating the h-values computed from experiments and those derived from FE simulations.

5.6.2.1 Integration of the local h-value

The assumptions suggest that the h-value is independent of temperature. It is, therefore, possible to allocate a temperature boundary condition to the top surface of the tool cylinder and another to the lower surface of the substrate cylinder for the two-dimensional solid elements. –refer to Figs. 5.5~5.6. At the same time, h_l, as a function of local interfacial pressure, is considered an input parameter for the FE model. It is assumed that the temperature field in the experiments is one-dimensional if the *disordered area* at the contact interface is ignored. Thus, zero film coefficients can be allocated to all cylindrical surfaces to enable a one-dimensional heat flow field. Thermo-mechanical coupled elastic-plastic FE analysis is required to simulate the thermo-mechanically coupled contact. Therefore, the mechanical contact and heat flow field at any given nominal interfacial pressure can be established from the any given local h-value. It can be predicted that the heat flow field is linearly distributed at a distant location from the contact interface. The thermal contact conductance of this one-dimensional heat flow field is defined as the integration of the local h-value. Hence, regression analysis can be used to obtain this integrated h-value. An

appropriate dimension is required to provide liner temperature fields to regressively determine the temperature drop ΔT_{stf} and heat flux q to enable the computation of h-value from

$$h = \frac{q}{\Delta T_{stf}} \tag{5-15}$$

Thus, the FE geometry model has a dimensional requirement for both, the tool and the substrate cylinders (refer to Fig. 5.5).

The relationship between local interfacial pressure and local h-value is established from the constitutive equation of the material and the deformation in the simulation of the thermo-mechanical contact. The requirement for using local thermal model for the simulation of the h-value is similar to that required for using the area ratio thermal model: the surface texture and the material properties.

5.6.2.2 Parameters for the local thermal model

The constant parameters used in the local thermal model (5-12) were determined by minimising the difference between h-values computed from experiments and those derived from FE simulations. From the h-value integration procedure, it is understood that the h-value is a function of the local h-value. Therefore, this difference can be minimised either by the least-squares-method or by updating the constants in the thermal model (5-12) using an iterative approach. Unique values of C_l, m and p_0 can be derived from the h-values computed from experiments performed under high interfacial pressures. It was established that different combinations of C_l, m and p_0 can be used to predict the variation of the h-value as the function of the nominal interfacial pressure up to a value of 180 MPa. These parameters are shown in the Table 5.1. Fig. 5.10 shows the diagrams of the used local thermal contact conductance as the function of local interfacial pressure using different combinations of C_l, m and p_0. The square function of the local thermal model was used in subsequent FE simulations. These parameters were determined from FE simulation results and experiments; further discussion of this subject is in section 5.8.

5.7 Results

The deformed mesh after thermo-mechanical contact is shown in Fig. 5.11 and the details of the mesh of the deformed equivalent asperity is shown in Fig. 5.12.

By using the thermo-mechanical coupled FE analysis, temperature field in the proximity of the interface was obtained; the local thermo-mechanical contact states were shown in Figs. 5.13~5.15.

The parameters used in the local thermal models (5-12) were determined for five different exponential functions which were chosen to simulate the local thermal contact conductance and the corresponding integrated h-value; these are linear, second, third, fourth and sixth order exponential functions respectively (refer to Fig. 5.10). An example of the corresponding simulation results and comparison with experimental data are shown in Figs. 5.16~5.17. The mean local interfacial pressure of the equivalent asperity was derived from simulations and is shown in Fig. 5.18. Local thermal model with different constants was also used to simulate an identical thermal contact condition to show the identity of the different combination of parameters; the result is shown in Fig. 5.19.

The area ratio thermal model (5-6) and the local thermal model (5-12) were used in the FE simulations. When the local thermal model was used, the integration procedure mentioned in Section 5.6.2.1 was adopted; further, a thermo-mechanical coupled FE analysis was used to integrate the h-values. If the area ratio thermal model was applied, elastic-plastic FE simulation was employed to simulate the area ratio as a function of the nominal interfacial pressure. The simulated h-value results are shown as a function of the nominal interfacial pressure in Figs. 5.20~5.31.

5.8 Discussions

5.8.1 Temperature field in the proximity of the interface

Previous researches [13,30] assumed that a small area in the proximity of the interface was subjected to a 3-dimensional heat flow field even for a one-dimensional temperature field. This assumption has been confirmed by the thermo-

mechanical coupled contact FE simulations that were conducted. With an assumed local h-value, the temperature distribution along the axis of the tool and the specimen is shown in Fig. 5.13. The temperature distribution is linear at the macro-level; a small disordered temperature distribution area was observed. The details of this disordered temperature field are shown in Fig. 5.14. The size of this disordered area may be, dimensionally, an order higher than the total height of the corresponding surface profile, depending on interfacial pressure. – refer to Figs. 5.13~ 5.15. For coarse surfaces, the total height of the surface profile may be greater than a hundred microns. Therefore, the dimension of the disordered area may be of the order of millimetre. This characteristic of the interface temperature field should be considered in surface temperature measurements [14~15]. A one-dimensional heat flow near the interface [15-16] was not observed.

Fig. 5.15 shows the variation of disordered area with the nominal interfacial pressure. The distribution of temperature is a function of the nominal interfacial pressure. Therefore, the temperature drop at the contact interface is not finite; it is of a continuously varying pattern. The cumulation of the temperature deviation from the macro-linearity of the temperature field, with respect to the height of the disordered area, plus a temperature difference on the contacted interface is the temperature drop at macro-level.

5.8.2 Determination of parameters of thermal models

Parameters in the thermal models should be determined before FE simulations. Values of h of several specimens, which appear to be among those with minimal surface macro-irregularities, were used to determine the parameters involved in the thermal models (5-6) and (5-12). Data for specimen 2.0-C was used as an example to illustrate the procedure for defining these parameters.

Fig. 5.16 shows the comparison between h-values computed from experiments and those derived from FE simulations using different local thermal models for specimen 2.0-C.

It is possible to define the range of the parameters m and p_0 in equation (5-12). The range 0~200 MPa in Fig. 5.16 was magnified for display in Fig. 5.17. Using the local thermal model, the h-value distribution is determined by the local interfacial pressure and the corresponding real contact area. A typical distribution of a mean local interfacial pressure is shown in Fig. 5.18. When the nominal interfacial pressure is low (<50 MPa), extremely high mean local interfacial pressure is activated; as the real contact area increases, the mean local interfacial pressure decreases to the nominal level. The distribution of the mean local interfacial pressure of different specimens is of similar patterns. The form of the equivalent asperity determines the distribution of the mean local interfacial pressure; almost no low local interfacial pressure occurred at the interface of the equivalent asperity and the tool regardless of the nominal interfacial pressure (refer to Fig. 5.5).

Local thermal contact conductance is a function of the local interfacial pressure. At low nominal interfacial pressure (< 50 MPa) on the original specimen surface, changes of the h-value are dominated by the high local interfacial pressure. As a consequence, the value of thermal contact conductance derived from FE simulation fluctuates, as shown in Fig. 5.17. The magnitude of this fluctuation depends on the values of m, p_0 and C_l. However, h-values computed from experiments do not show these fluctuations for low nominal interfacial pressure. This difference between experiment data and FE simulation results suggests that either one or both of the following assumptions apply:

- The local thermal contact conductance, as a function of local interfacial pressure, should be close to a constant; the local thermal conductance cannot be infinite regardless of the local interfacial pressure.
- The exponential parameter m in equation (5-12) should not be greater than 2.

Violation of these two assumptions will lead to differences between the h-values computed from experiments and simulated by FE simulations at low nominal interfacial pressure.

It is not possible to confirm whether both these conditions are correct at current experimental data. The fluctuation in the simulated results can be eliminated by modifying either the exponential parameter m or the critical interfacial pressure p_0; or both. This can only be confirmed by performing experiments at high nominal interfacial pressures; the influence of m on the h-value is obvious when the nominal interfacial pressure is high (>400 MPa). –refer to Fig. 5.16. More accurate instrument for measuring temperature is required to confirm the parameters used in the local thermal model (5-12).

It would be difficult to establish unique values of m and p_0; it is possible, however, to determine different combinations, under which the h-values can be predicted accurately for nominal interfacial pressures up to 180 MPa (refer to Fig. 5.19); the h-value for the specimen 2.0-C was predicted by different combinations of m, p_0 to the same degree of accuracy. The different combinations of parameters which are available for h-value FE simulation are listed in the Table 5.1.

In Fig. 5.18, the mean local interfacial pressure varies between 950~1250 MPa beyond nominal interfacial pressures greater than 50 MPa. If this mean local interfacial pressure is used to represent the local interfacial pressure, it can be observed from Fig. 5.10 that the local thermal contact conductance would have a value greater than 950 $kWm^{-2}K^{-1}$ since the local interfacial pressure is greater than 950 MPa. The upper-limit of the variation range is dependent on the assumed exponential parameter m. If $m=1$, the upper-limit cannot be defined for the experimental interfacial pressure range data; if $m=2$, the upper-limit is about 1600 $kWm^{-2}K^{-1}$; if $m\geq 3$, the upper-limit is less than 1200 $kWm^{-2}K^{-1}$. These results suggest that local thermal contact conductance varies over a narrow range, the lower-limit of which is about 950 $kWm^{-2}K^{-1}$ and the upper-limit should be confirmed by the experimental data under higher nominal interfacial pressures. Local thermal contact conductance may be possibly simplified into a constant. This conclusion is significant, because the local thermal contact conductance at high local interfacial pressure can be considered as thermal contact conductance at perfect contact

condition that is applicable for the contact in cold forming. However, more experimental investigations and data at higher interfacial pressures are required to support this.

This variation range of the local thermal contact conductance is of significance to the determination of the h-value using the area ratio thermal model considering above discussions. It can be inferred that the thermal contact conductance under perfect contact for N910 and Ma8 should be greater than 950 $kWm^{-2}K^{-1}$ and the upper-limit should be determined by performing experiments at high nominal interfacial pressures. It is predictable that the variation range of thermal contact conductance at perfect contact condition should be also small, just like that of local thermal contact conductance. Therefore, the experimental data and FE simulation results in this research have shown that the basic assumption in area ratio thermal model (5-6), which assumes that value of h at high interfacial pressure is close to a constant, applies. Parameter pairs, C_a and λ, m and p_0, equivalently describing the h-value at high nominal interfacial pressure, can be confirmed only by experimental data at high nominal interfacial pressures.

It should be pointed out that if $m \geq 3$ is used in the FE simulation, from Fig. 5.10, local h-value, in fact, is almost simplified into a constant 1050~1200 $kWm^{-2}K^{-1}$. Therefore, experimental data can be fitted well by using a constant local h-value in FE simulations. Local thermal contact conductance is probably a constant, and this constant probably is the thermal contact conductance at perfect contact condition.

5.8.3 Comparison between h-values computed from experiments and derived from FE simulations.

Comparisons between h-values computed from experiments and derived from FE simulations are shown in Figs. 5.20~5.31. All diagrams contain three sets of data, – derived from the local thermal model (5-12), the area ratio thermal model (5-6), and the experimental data.

From the experimental data shown in Figs. 3.18~3.24 and the measured initial specimen mean spacing, it can be found out that h-value computed from experiments are almost inversely proportional to the mean spacing. This is the foundation and basic reason to present an area-ratio thermal model shown by equation (5-6). Therefore, the basic thermal model constants determined by one specimen can be also used to present the h-value for other specimens without much difference.

Both, simulation and experimental results, show that h-value is approximately a linear function of the nominal interfacial pressure in range 0~180 MPa. –refer to diagrams Figs. 5.20~5.31. This linear relationship was derived using the same set of parameters for the local thermal model, shown in Fig. 5.19; different combinations of C_1, p_0 and m were selected for the simulation. Similar results were obtained using the area ratio thermal model. This linear distribution of h-values was also reported by other researchers [11]. However, experimental data shows a nonlinear trend. –refer to Figs. 5.24, 5.26, 5.28 and 5.31 for specimen 2.0-E, 2.5-E, 3.0-F and 4.0-E, which had relatively coarse surface textures (refer to Table 3.1).

It was observed that if the surface texture changes predicted by FE simulation (Chapter 4) matched experimental measurements, the thermal contact conductance predicted by FE simulations matched the experimental h-values well. The h-values derived from FE for specimens 2.0-C, 2.5-D, 3.0-D and 4.0-D, shown in Figs. 5.22, 5.25, 5.27 and 5.30 respectively, are the typical examples of these; the corresponding surface deformation simulations and surface measurements are shown in Figs. 4.18, 4.21, 4.24 and 4.27 respectively. Similarly, if the differences surface parameters were large, the differences in h-value were also large. Examples were shown in Figs. 5.28 and 5.29 for specimens 3.0-F and 4.0-C; the corresponding surface measurements and surface deformation predicted by FE simulations are shown in Figs. 4.25 and 4.26, respectively. It is understandable that the equivalent asperity is defined based on isotropic and uniform surface texture. Thus, the FE model of the equivalent asperity can be used to predict the h-value of a surface with isotropic and uniform texture. Surface measurement data shows that surface parameters of some specimens, especially after initial compression, are dependent on measuring location; the surface

is not isotropic and uniform. Therefore, the FE simulation results are different from the experimental data. An exception is also shown in Fig. 5.24 for specimen 2.0-E. The surface deformation predicted by FE simulation for this specimen is in agreement with the surface measurements (refer to Fig. 4.19); the difference between h-values computed from experiments and derived from FE simulations is relatively large. This may imply that there are other factors that influence the accuracy of the h-value.

5.8.4 Factors influencing the accuracy of h-value FE simulation

5.8.4.1 Surface macro-irregularities

Surface macro-irregularities result in non-uniform contact between tool and specimen, and this non-uniform is at macro-level. Non-uniform contact further results in non-uniform surface texture and surface anisotropy. Surface macro-irregularities divide specimen surface into two parts, contact part and non-contact part. The real contact area, influenced by these macro-irregularities, will be less than it should be when without these macro-irregularities. Therefore, surface macro-irregularities will decrease the h-value. At the same time, increasing of nominal interfacial pressure reduces surface macro-irregularities by surface deformation; both, the contact area of individual asperity and the number of the contact asperities, will increase with the increase of the nominal interfacial pressure. Therefore, the slope of h-value with respect to nominal interfacial pressure is greater than that of a specimen without macro-irregularities and with the same level of surface roughness; macro-irregularities are one of factors that cause nonlinearity between thermal contact conductance and nominal interfacial pressure.

5.8.4.2 Yield Strength of surface asperities

Yield Strength of asperities may influence the evaluation of thermal contact conductance as a function of the nominal interfacial pressure. The Yield Strength of specimen surface asperities may be different from that of specimen as specified by equation (3-11) which was obtained from upsetting test; this difference is caused by the specimen preparation operations, in particular the EDM-machining operation. Surface hardening effect by cutting and grinding operations may be removed by the

finish-EDM-machining operation. The surface hardening effect of EDM-machining operation remains. Electric discharging heats the local material at specimen surface to a temperature higher than the corresponding melting point of the material in a liquid insulator cooling media. This operation hardens the specimen surface. The influence of the Yield Strength of asperities on h-value evaluation should be the same for all specimens. The hardened surface asperities influence the relationship between the nominal interfacial pressure and the local interfacial pressure, and the deformation of individual asperity, and further influence the relationship between thermal contact conductance and nominal interfacial pressure, as well as the relationship between thermal contact conductance and area ratio. The Yield Strength of surface asperities would be difficult to establish accurately.

5.8.4.3 Accuracy of initial surface measurement and initial surface texture

The geometry of the simulation model was based on the equivalent asperity derived from surface measurements. If the initial surface is not isotropic and uniform, the measured parameters cannot represent the actual surface texture; further, the corresponding equivalent asperity would not represent this surface. In this case, there will be obvious difference between the h-values computed from experiments and those derived from FE simulations. Surface measurements with large evaluation length and using the average parameter of the measurements may improve the simulation accuracy.

Factors influencing the accuracy of the simulated h-value are complex. Accuracy of the h-values computed from experiments is also influenced by many factors. Therefore, the factors affecting the difference between h-values computed from experiments and simulation are more complex. Precise explanation of the difference for all specimens shown in Figs. 5.20~5.31 would be difficult. This may suggest that there are some other factors that influence the FE simulation accuracy or the accuracy of h-value computation from experiments, and have not been recognised.

5.9 Further considerations

Relative sliding, surface expansion, lubrication and surface contamination are not considered in the thermal contact conductance FE simulation models established in this research, due to the limitation of the current experimental conditions and experimental data. These are important contact characteristics of the billet/tool interface in cold forming and influence the thermal contact property actively. Although thermal contact conductance can be evaluated by a steady-state heat transfer process, the heat transfer across the interface of billet/tool interface in cold forming is usually not a steady process [32]. Transient and dynamic heat transfer, actual active contact conditions in cold forming should be considered further in both, the experimental and analytical or numerical investigations.

On the other hand, determination of constants used thermal models relies on the experiments at higher interfacial pressures, which may be obstructed by the threshold.

5.10 Future work

In this section, it is pointed out that uniquely determine thermal model constants is possible by using the current experimental equipment. A few improvements have to be conducted first.

1. Temperature gradient should be decreased, for more accurately calibrate thermocouples.

In fact, in temperature range of cold forging, h-value is almost independent of temperature. If the temperature of the one-dimensional field can be controlled within 100 degree, the in- or out-cooler can be applied to calibrate the thermocouples. These coolers have stability accuracy within 0.01 degree. Therefore, thermocouples accuracy can be calibrated with a relative accuracy 0.01 degree. In this case, temperature gradient is about 1300 degrees per meter. The heat flux density would be about $q = 1300 \times 20 = 26\ kWm^{-2}$. Assuming that the h-value at perfect contact is

about 1000 $kWm^{-2}K^{-1}$ according to the work in this Chapter. Thus, the temperature drop would be

$$\Delta T = \frac{26}{1000} = 0.026\ ^{\circ}C$$

2. Optimally positioning thermocouples. These can control uncertainty coefficient within 0.45.

3. Using thin thickness specimens, for example, t=0.5~1.5 mm. In this case, the uncertainty caused by specimen can be ignored.

Therefore, the uncertainty in such designed experiment would be

$$E_u = 0.45 \times \frac{0.01}{0.026} = 17\%$$

This error is acceptable; and it is possible to obtain the unique thermal model constants. And finally, a method and equipment for measurement of surface flatness has to be determined to evaluate surface flatness. This parameter is very important to the heat transfer across the contact interface.

5.11 Conclusions

(1) Equivalent asperity and the established FE geometric model can be used to simulate thermal contact conductance between an isotropic, uniform rough surface and a perfect plane;

(2) Thermal contact conductance is nearly a linear function of nominal interfacial pressure up to 180 *MPa* for the matching materials N910 and Ma8; surface texture and macro-irregularities influence the slope of the distribution; finer surfaces and lower macro-irregularities result in higher h-values and higher slopes of the h-value. A typical h-value range at 200 MPa is from 25 ~160 $kWm^{-2}K^{-1}$ with a change of initial surface texture from $R_a = 0.74 \sim 0.97\ \mu m$ to $R_a = 3.51 \sim 4.97\ \mu m$ for materials N910 and Ma8.

(3) Thermal contact conductance between materials N910 and Ma8 under perfect contact conditions ($r=1$) is greater than 950 $kWm^{-2}K^{-1}$; the upper-limit, varying in a small range, may be established by performing experiments under high nominal interfacial pressures. This validates the assumption that thermal contact conductance tends to a constant at high interfacial pressure.

(4) Both, the area ratio thermal model and the local thermal model, are presented and used to simulate h-values; results are in agreement with the h-values computed from experiments. Unique determination of thermal model parameters requires experimental data at high nominal interfacial pressures. Probably, local thermal contact conductance can be simplified as a constant. This constant is also the h-value at high interfacial pressure.

(5) The temperature field in the proximity of the interface is three-dimensional; the temperature drop at the interface is a continuous cumulation of the temperature deviation from the macro-distribution and the drop at contacted interface; this disordered area may have a dimension of the order of one millimetre.

(6) Surface macro-irregularities, surface measurement accuracy and the Yield Strength of the asperities are the main factors that influence the accuracy of h-value simulation. However, there may be unknown factors.

(7) A possibility of to determine unique thermal model constants has been analysed.

5.12 Reference

1. M. R. Sridhar, M. M. Yovanovich, Elastoplastic Contact Conductance Model for Isotropic Conforming Rough Surface and Comparison with Experiments, Journal of Heat Transfer, Transactions of the ASME, Vol. 118, 1996, pp. 3-9
2. M. G. Cooper, B. B. Mikic and M. M. Yovanovch, Thermal Contact Conductance, International Journal of Heat and Mass Transfer, Vol. 12, No. 3, 1969, pp. 270-300

3. J. A. Greenwood and J. B. P. Williamson, Contact of Nominally Flat Surfaces, Proceedings of the Royal Society of London , A295, 1966, pp. 300-319
4. B. B. Mikic, Thermal Contact Conductance; Theoretical Considerations, International Journal of Heat and Mass Transfer, Vol. 17, 1974, pp. 205-214
5. A. W. Bush, R. D. Gibson and T. R. Thomas, The Elastic Contact of A Rough Surface, Wear, Vol. 35, No. 2, 1975, pp. 87-111
6. D. J. Whitehouse and J. F. Archard, The Properties of Random Surfaces of Significance in Their Contact, Proceedings of Royal Society of London, A316, No. 1524, 1970, pp. 97-121
7. A. Majumdar and C. L. Tien, Fractal Network Model for Contact Conductance, Journal of Heat Transfer, Vol. 113, 1991, pp. 516-525
8. M. M. Yovanovich and A. Hegazy, An Accurate Universal Contact Conductance Correlation for Conforming Rough Surfaces with Different Micro-Hardness Profile, AIAA, paper 83-1434,1983
9. V. W. Antonetti, On the Use of Metallic Coatings to Enhance Thermal Contact Conductance, Ph.D. Dissertation, University of Waterloo, Waterloo, Ontario, Canada, 1983
10. A. A. Hegzay, Thermal Joint Conductance Conforming Rough Surfaces, Ph.D. Dissertation, University of Waterloo, Waterloo, Ontario, Canada, 1985
11. M. R. Sridhar and M. M. Yovanovich, Thermal Contact Conductance of Tool Steel and Comparison with Model, International Journal of Heat and Mass Transfer, Vol. 39, No. 4, 1996, pp. 831-839
12. D.G. Blanchard and L. S. Fletcher, Contact Conductance of Selected Metal-Matrix Composites, Journal of Thermophysics and Heat Transfer, Vol. 9, No. 3, 1995, pp. 391-396
13. K. Nishino, S. Yamashita and K Torii, Thermal Contact Conductance Under Low Applied Load in A Vacuum Environment, Experimental Thermal and Fluid Science, Vol. 10, 1995, pp. 258-271
14. M. A. Lambert and L. S. Fletcher, Review of the Thermal Contact Conductance of Junctions with Metallic Coatings and Films, Journal of Thermophysics and Heat Transfer Vol. 7, No. 4,1993, pp. 547-554

15. M. A. Kellow, A. N. Bramley and F. K. Bannister, The Measurement of Temperature in Forging Dies, International Journal of Machine Tool Design and Research, 1969, Vol. 9, pp. 239-260
16. M. A. Kellow, et al., The Oxidation of Steel at High Temperature and Its Effect on Die Surface Temperature in Hot Forging, Proceedings of 17th MTDR Conference, 1977, pp. 335-346
17. P. Dadras and W. R. Wells, Heat Transfer Aspects of Nonisothermal axisymmetric Upset Forging , Journal of Engineering for Industry, Transactions of the ASME, 1984, Vol. 106, pp. 187-195
18. S. L. Semiatin, E. W. Collings, V. E. Wood and T. Altan, Determination of the Interface Heat Transfer Coefficient for Non-Isothermal Bulk-Forming Processes, Journal of Engineering for Industry, Transactions of the ASME, 1987, Vol. 109, pp. 49-57
19. Y.H. Li and C. M. Sellars, Evaluation of Interfacial Heat Transfer and Its Effects on Hot Forming Processes, Ironmaking and Steelmaking, Vol. 23, No. 1, 1996, pp. 58-61
20. W. Nshama, J. Jeswiet and P.H. Oosthuzien, Evaluation of Temperature and Heat Transfer Conditions at Metal-Forming Interface, Annals of the CIRP, Vol. 44, No. 1, 1995, pp. 201-204
21. Z. M. Hu, J. W. Brooks and T. A. Dean, The Interfacial Heat Transfer Coefficient in Hot Die Forging of Titanium Alloy, Proceedings of Institute of Mechanical Engineers, Vol. 212, Part C, 1998, pp. 485-496
22. Z. Malinowski et al., A Study of the Heat-Transfer Coefficient as A Function of Temperature and Pressure, Journal of Material Processing Technology, 1994, Vol. 41, pp. 125-142
23. E. R. Ecket and R. M. Drake, Jr., Analysis of Heat and Mass Transfer, Hemisphere, New York, 1987
24. Shamasundar, et al., Numerical and Experimental Study of the Thermal Behaviour of Coining and Upsetting Processes, Journal of Materials Processing Technology, 1993. Vol. 36, No. 2, pp. 199-221
25. B. Sanith, S. D. Probert and W. P. O'Callaghan, Thermal Resistance of Pressed Contact, Applied Energy , Vol. 22, 1986, pp. 510-523

26. M. M. Yovanovich, Overall Constriction Resistance Between Contacting Rough Wavy Surfaces, International Journal of Heat and Mass Transfer, Vol. 12, 1969, pp. 1517-1520
27. A. M. Clausing and B. T. Chao, Thermal Contact Resistance in A Vacuum Environment, Transactions of The ASME, Journal of Heat Transfer, Vol. 87, No. 2, 1965, pp. 243-251
28. K. Sanokawa, Heat Transfer Between Metallic Surfaces in Contact (4th Report, The Effects of the Shape of Surface Roughness and the Waviness, and the Approximate Method of Calculating Thermal Contact Resistance), Bull. JSME, Vol. 11, No. 44, 1968, pp. 287-293
29. S. L. Semiatin, E. W. Collings, V. E. Wood and T. Altan, Determination of the Interface Heat Transfer Coefficient for Non-Isothermal Bulk-Forming Processes, Journal of Engineering for Industry, Transactions of the ASME, 1987, Vol. 109, pp. 49-57
30. M. Leung, C. K. Hsieh and D. Y. Goswami, Prediction of Thermal Contact Conductance in Vacuum by Statistical Mechanics, Journal of Heat Transfer, Transactions of The ASME, Vol. 120, pp. 51-57, 1998
31. S. Y. Lin, Investigation of Die-Workpiece Interface Friction with Lubrication During the Upsetting Process, International Journal of Advanced Manufacturing Technology, Vol. 15, pp. 666-673, 1999
32. A. S. Marchand and M. Raynaud, Numerical Determination of Thermal Contact Resistance for Nonisothermal Forging Processes, Transactions of ASME, Journal of Heat Transfer, Vol. 122, pp. 776-784, 2000

Chapter Six

Continuously variable interference fitting of forming tools – A mathematical concept

6.1 Summary

Pre-stressed chambers, produced by compounding two cylinders, have long been used as an approach to enhance die strength, in particular for extrusion dies [1]. Recently, researchers have begun to consider the application of this type of die for improvement of forging accuracy [2]. However, in most cases, the interference between the cylinders was uniform; profiled interference was rarely found applications in forging [3], perhaps for want of exact analytical considerations.

Two methods, one using die surface deflection equations, the other, using minimisation technique, and the both combining FE simulations with fundamental analysis, are presented in this research for the determination of the required contoured interference, with a view to compensating for die elasticity or component form-error. Interference specified at the shrink-fitting interface of a die would contract the working surface of the tool due to shrink-fitting force. This contraction, referred to as pre-deflection, is defined as a function of die surface location and the contour of the interference. Physically and mathematically, a contoured interference can be defined to pre-deflect the die surface in a way towards compensation for die-elasticity or overall component-error.

Together with FE analysis, an iterative procedure for determining of this profiled interference was established; manufacturability of the profiled interference form was taken into account. The established approach was used to define the required profiled interference of a closed-die-forging tool. FE simulations showed that, with the specified profiled interference, the die deflection during forming can be controlled to

be a straight line contour instead of the curved; die stiffness is enhanced without resorting to the conventional approach of increasing the die dimensions.

By using the developed component-error minimisation technique, together with thermo-mechanical coupled FE simulations, optimum continuous profiled interference was obtained, by which overall component-error was minimised to a few microns. Sufficient die surface pre-stress can be provided by this profiled interference. Therefore, precision cold forming component can be produced with satisfactory working life of tools by the optimisation technique. Different influential factors on minimisation of component-error were discussed and analysed.

6.2 Nomenclature

A Interface stiffness matrix

a Element of matrix A

B Interface compliance matrix

b Element of matrix B

E Overall component-error

f Friction factor

l Number of die surface nodes on which constraints are required to be satisfied

m Total number of nodes on die surface

n Total number of nodal pairs on shrink-fitting interface

p Normal nodal contact force on shrink-fitting interface

s Co-ordinate along axial direction

T Sum of squares

X Required interference vector on shrink-fitting interface

x Normal nodal interference value on shrink-fitting interface

Y A force vector acting on insert shrink-fitting surface due to shrink-fitting

Z Simplified profiled interference vector

z Coefficient of independent interference or the component of vector Z

ξ Die surface deflection

ϕ Component-form error disparity

α Weight coefficient

δX	Increment of design variable vector X
δx	Increment of a component of design variable vector X
δ	Actual surface deflection at a die surface node
Δx	Searching step increment of a component of design variable vector X
$d\xi$	Perfect differential of ξ at initial design point
ΔX	Searching step increment of design variable vector
ΔT	Increment of T
$\bar{u}$	Translation displacement
φ	Distributed interference function
ζ, ε	Parameters to control the termination of iteration

Subscripts

0	Initial or original
1	Constant one
2	Constant two
a	Accurate value
e	Pre-deflection predicted by FE simulation
i	One of the following meaning
	• the i^{th} row of a matrix
	• the i^{th} component of a vector
	• the i^{th} node (element)
j	The j^{th} column of a matrix, or similar to subscript i
max	Maximum
min	Minimum
p	Pre-deflection
r	Actual surface deflection

Superscripts

(0)	Initial or original
(j)	The j^{th} cycle iteration
(i)	The i^{th} iteration

6.3 Glossary

Pre-deflection: The die surface will elastically and permanently deflect due to the specified interference; this dimension is the pre-deflection.

General profiled interference: A contour of interference that is a function of shrink-fitting interface location without linearisation, and by which die elasticity or overall component-error can be compensated for.

Linear profiled interference: A profiled interference that is a linear function of shrink-fitting location in segments.

Unit interference: A linearly profiled interference, defined by equation (6-10).

Interference vector: Linear profiled interference can be defined by the interference values at active nodes; interference values at active nodes form a vector, referred to as interference vector.

Active node: A node on the shrink-fitted interface, on which shrink-fitting force is greater than zero, or a node on which a special shrink-fitting interference is specified.

Component-form error disparity: Dimensional difference between component surface and die surface after ejection and cooling down.

Direct compensation: Component form-error is compensated for by directly modifying the die surface form and dimensions.

Translation displacement: A uniform modification of die surface dimension in normal direction by which direct compensation is conducted.

6.4 Introduction

The accuracy of a cold-forged component depends on several factors that derive from the forming process. As the billet deforms in the die cavity, high contact pressures are generated on the die surface. This high contact pressure results in die deflection. Had the die surface been designed to match the ideal component surface, this expansion of the die surface would result in form-errors on the final cold-forged component. Die deflection is a major contributor to the form-error of component.

Investigation of die deflection originates from the need to minimise processing costs. High precision cold-forging invariably imposes a high pressure on the die surface, which, in turn, results in die deflection [4,5] and tool wear [6]. Component form-error

caused by die deflection is comparable to those caused by other error-contributors, such as Secondary Yielding [7], which refers to plastic deformation during the retraction of forging loads. Temperature changes and work-material elasticity make further contribution to the overall component form-error [7-8]. Compensation for die deflection would be a significant contribution to the manufacture of high precision engineering components by cold forging.

One approach to error-compensation is to modify die form. This method has been systematically researched by Balendra, Qin and Lu [9], and has been successfully applied [4-5,10]. However, it is difficult to determine die surface compensation data accurately, either by FE simulation or by direct measurement of the component form [9]. Therefore, the direct die surface compensation process would have to be iterative. Since this compensation process involves the modification, re-designing and re-manufacturing of the die surface, this approach incurs long lead times. Meanwhile, die deflection is usually a complex function of die surface location; the manufacture of the die surface to micron level accuracy is difficult and expensive.

The alternative is to improve component accuracy by use of shrink-fitting to compensate for die-deflection or component form-error. A pre-stressed die has a pre-deflected die-surface; pre-deflection dimensions and form depend on the specified interference. Forming pressure profile on the die surface is usually not uniform; it is, therefore, difficult to design uniform interference to compensate for die deflection or overall component-error effectively [2,11]. With the development of computer techniques and numerical methods, it is possible to use Finite-Element methods to define a profiled interference as a function of the interface location to enable a pre-deflection which compensates for actual die deflection or component form-error. By this approach, the manufacturing requirements are transferred from the complex inner surface of the insert to its external surface.

Recently, Qiang et al. [12] reported an application of shrink-fitting for synthesising diamonds. Basically, the shrink-fitted die was designed to reduce the working stress on the die surface. The improvement of component accuracy by shrink-fitted die has

evolved in recent years, however. An analysis of shrink-fitted die enabling die deflection compensation for axisymmetric components was reported [2]. A uniform interference is specified on to the shrink-fitting interface between die insert and stress-ring. An assumption of uniform pressure over the entire die surface was introduced in order to apply thick-cylinder theory [11]. This assumption would not be valid for closed die-forging.

Die optimisation was also extensively investigated in recent years. Different targets were selected as optimum objectives. Optimisations of die surface contour [13-16], billet shape and positioning [11,17-18], wear, strength and life span of die [12,19-22], were investigated by different researchers. Investigations on optimisation of component accuracy were also reported. Zhao, Wright and Grandhi [23] developed a sensitivity analysis for preform die shape design in nett-shape forging process using rigid viscoplastic finite element method. Preform die shapes were represented by cubic B-spline curves. Control points or coefficients of B-spline were used as design variables. The objective was to minimise the zone where the actual and desired final forged shapes did not coincide. Badrinarayanan and Zabaras [24] researched a similar method. Die- and work-materials elasticity was neglected due to the application of rigid-plastic FE analysis. Wanheim, Balendra and Qin [25] proposed a novel structure in forward extrusion to compensate for component-error due to die elasticity. Finite element simulation verified its effectiveness.

From the engineering point of view, it is the component overall form-error that is important. It appears that there is not much attention paid to the compensation for overall component form-error.

This reported research presents methods for determining the interference for forging dies using FE simulation, aimed first at die-deflection compensation for non-uniform axisymmetric components by specifying a *profiled interference* on shrink-fitting interface, and second at overall component-error compensation, including the influence of elasticity of tool- and work-materials, temperature and Secondary Yielding, by a minimisation technique. Since the numerical method will be used, it is not necessary to

assume the forming pressure distribution pattern on the die-surface; also, it can be noted that the analysis is limited to axisymmetric components due to the limitation of manufacturing technologies. Numerical methods will be developed for the determination of the most suitable profiled interference on shrink-fitting interface, either for die-elasticity or overall component-error compensation. Meanwhile, after choosing the optimum geometric design parameters, the optimum pre-stress at the die surface may also be achievable.

6.5 Die elasticity compensation algorithm

It is assumed that friction at the shrink-fitting interface can be ignored. The friction force at interface depends on the surface conditions and the assembly procedure. A shrink-fitted forging die consists of an insert and stress-rings or containers. The number of rings determines the number of shrink-fitting layers. – refer to Fig. 6.1. Fig. 6.1a shows a die with one layer of shrink-fitting interface and Fig. 6.1b, with two layers. The reported research only considers a single layer.

6.5.1 Unit force, FE models and interface compliance matrix

In order to determine a profiled interference, the numerical relationship between the shrink-fitting force and die-surface pre-deflection should be determined. This relationship is defined by a so-called unit force FE model.

A mechanics model, referred to as *general mechanics model,* should be established for the forming process, including tooling configuration. Fig. 6.2a shows a closed-die upsetting process; the corresponding mechanics model is shown in Fig. 6.2b. This mechanics model defines the FE mesh model, boundary conditions and loading pattern. The FE model can be finalised according to the general mechanics model after defining the materials properties and the contact conditions. Figs. 6.2c~d show how unit force mechanics models are established from the general mechanics model. Three factors should be considered. These include (1) considering only the insert or stress-ring, (2) replacing the contact between the ring and insert with a pair of unit normal nodal forces, and (3) reinstating the insert (ring) related boundary conditions as in the general mechanics model. A unit force mechanics model for the insert is shown in Fig. 6.2c,

and that for stress-ring, in Fig. 6.2d. Thereafter, unit force FE models can be established based on these unit force mechanics models, geometric conditions and further considering the insert and stress-ring materials, respectively.

From the unit force FE models, the relationship between the shrink-fitting force and die surface pre-deflection can be obtained; this can be described by a matrix, referred to as *interface compliance matrix B*,

$$B = \left(b_{ij}\right) \tag{6-1}$$

where b_{ij} is die surface pre-deflection in normal direction at node i when a unit force acts at shrink-fitting surface node j of insert along its normal direction. Obviously, B is a $m \times n$ matrix and obtained from numerical simulations using unit force FE models. This interface compliance matrix is uniquely determined by die dimensions and materials, without any relation to either forming process or working material; it is a numerical description of the mechanical performance of the die.

6.5.2 Shrink-fitting model

Let vector Y denote nodal forces at the interface on the insert, i.e.

$$Y = \left(p_1\, p_2 \cdots p_j \cdots p_n\right)^T \tag{6-2}$$

If the insert can be considered linearly elastic, the linear superposition principle can be applied [26]. Therefore,

$$\xi_p = BY \tag{6-3}$$

Equation (6-3) is the physical significance of the interface compliance matrix B. If matrix B is obtained, the pre-deflection under any force vector Y can be defined; matrix B connects the pre-deflection with the shrink-fitting force. Let

$$\xi_p + \xi_r = 0 \tag{6-4}$$

where

$$\xi_r = \left(\delta_1\, \delta_2 \cdots \delta_m\right) \tag{6-5}$$

Equation (6-4) shows that the die deflection occurs both before and during forming in opposite directions, and the linear superposition of two opposite deflections leads to die elasticity compensation. Substituting equation (6-4) into equation (6-3), a linear simultaneous equation group is obtained

$$BY = -\xi_r \tag{6-6}$$

for a perfect die elasticity compensation. When actual die deflection ξ_r is given, force vector Y acting at all nodes of insert on shrink-fitting surface is defined by equation (6-6). Note that a force, $-Y$, the counteracting force vector of Y, acts on the shrink-fitting surface of the stress-ring. Thus, from equation (6-6), two mechanics models, one, for the insert, loaded with Y, the other, for the stress-ring, loaded with $-Y$, are defined, as shown by Fig. 6.3. From these two mechanics models, two elastic FE simulation models can be established. After simulations with the corresponding FE models, the required relative displacements vector X between the two shrink-fitting surfaces, or the profiled interference on shrink-fitting interface, can be defined as

$$X = (x_1\ x_2 \ldots x_n)^T \tag{6-7}$$

It must be pointed out that the j^{th} equation in linear equation group (6-6) is satisfied means that the corresponding pre-deflection of j^{th} node on die surface is confined to $-\delta_j$. Therefore, equation group (6-6) can be also considered constraints specified on die surface nodes, which constrains pre-deflection of every node to the expected value. This technical term, the constraint, will be used in the following text.

6.5.3 Nonlinear contact iterative approach

6.5.3.1 Different cases of contact equation

Equation (6-6) describes the contact at shrink-fitting interface. The mesh pattern determines the form of the matrix B. Matrix B may not be square; nodes on shrink-fitting surface n may not be the same as that on die surface, m. However, equation (6-6) has a unique solution under a condition that matrix B should be non-singular. This requires that matrix B should be square, at least. There are three possible forms of matrix B according to the mesh patterns; their physical significance and how to transform them into a square form are explained in appendix 6.1.

No matter which case it is, matrix B can be finally transformed into a square. -refer to appendix 6.1. It is, therefore, assumed that the nodes on shrink-fitting surface and those on die surface are equal, and interface compliance matrix is square.

6.5.3.2 Non-linear iteration approach

Equation (6-6) seems likely to be a simple linear equation group. Actually, it describes a complex non-linear contact between the two shrink-fitting surfaces. Note that interference in shrink-fitting surface must be non-negative; shrink-fitting pressure should be positive. Therefore, every component of solution from equation (6-6) must satisfy the following inequalities

$$p_j \geq 0 \qquad (6\text{-}8)$$

or

$$x_j \geq 0 \qquad (6\text{-}9)$$

Any solution of equation (6-6) which is in contradiction with inequalities (6-8) or (6-9) makes no sense, physically. Thus, the die elasticity compensation leads to a mathematical problem for a non-negative solution from equation (6-6).

Fig. 6.4 shows a case where shrink-fitting force on a node is negative. An iteration procedure is established for a non-negative solution by mathematical analysis. –refer to appendix 6.2.

Assuming there are l nodes on die surfaces, the constraints on which must be satisfied. Summarising the analysis in appendix 6.2, the non-linear iteration procedure of equation (6-6) for a non-negative solution is:

(1) Obtaining solution of linear equation group (6-6); if all $p_i \geq 0 (i = 1, 2, ..., l)$ go to 3; or

(2) Deleting the non-negative constraint with biggest pressure or closest to the negative constraint, forming a new equation group, return to1,

(3) If all $p_j \geq 0$ then go to 5, or

(4) Deleting corresponding negative constraints, forming a new equation group, return to 1,

(5) End.

6.5.4 Manufacturing considerations and displacement approach

6.5.4.1 Segmental linearisation of the profiled interference

The profiled interference obtained by the method presented in the previous sections may be a complex curved surface that is difficult to manufacture. It is, therefore, necessary to simplify the obtained profiled interference. An interference value with its position on shrink-fitting surface forms a space point; all interference points connected one by one form the profiled interface. Profiled interference is a curve in case of axisymmetry. A schematic diagram of linearisation of a profiled interface is illustrated by Fig. 6.5 for axisymmetric component; the general profiled interference is shown by solid line and the linear profiled interference is presented by dashed line (I) or thin solid line (II). Choosing the type of linearised profiled interference is determined by accuracy requirement. After this linearisation, the complex revolutionary surface is simplified into a finite truncated conical surface; manufacturing of this surface is easier.

Die surface pre-deflection may be sensitive to interference. Therefore, the replacement of the general profiled interference with linearised interference in segments may influence the compensation effect. However, there are no basic differences between the general profiled interference and the linearised interference in segments. In fact, the general profiled interference is one of the linearised interference with elemental length as its segmental length. At the same time, it is the interference at active nodes that play active parts; the pre-deflection is not sensitive to the interference at non-active nodes. A linearised interference more close to the general profiled interference can be chosen, as shown by the thin solid line in Fig. 6.5 (II); however, it is also relatively difficult to manufacture.

Due to that the pre-deflection under this linear interference may be different from that under the profiled interference from equation (6-6), a further analysis is required. An analytical method is thus presented to obtain the best linearisation of the profiled interference, as shown in the following text.

6.5.4.2 Displacement approach

6.5.4.2.1 Unit interference and interference vector

As shown in Fig. 6.6, interference at node j, with axial ordinate s_j, is unit and linearly distributed along axial direction. Node j is referred to as an *active node*, and the interference, as *unit interference*, denoted by φ_j. Obviously, φ_j can be expressed by a function

$$\varphi_j(s)=\begin{cases}\dfrac{s}{s_j} & (s_0 \le s \le s_j)\\[2ex] \dfrac{s_n-s}{s_n-s_j} & (s_j < s \le s_n)\end{cases} \qquad (6\text{-}10)$$

where $s_0=0$. Similarly, if interference value at node j is z_j instead of unit with the similar distribution, it is referred to as *independent interference*. Truncated conical surface can be considered a linear superposition of different independent interference along shrink-fitting surface. Therefore, if different independent interference $z_0\varphi_0$, $z_1\varphi_1, \cdots, z_k\varphi_k$ at active nodes are known, the overall interference can be superposed by

$$\varphi(s)=z_0\varphi_0(s)+z_1\varphi_1(s)+\cdots+z_k\varphi_k(s) \qquad (6\text{-}11)$$

which is shown in Fig. 6.7 by thick solid segments. The coefficients $z_l\ (l=0,1,2,\cdots k)$ are main parameters to describe the distribution of a linearly profiled interference. A vector, referred to as *interference vector* Z, is defined to show this distribution:

$$Z=(z_0,z_1,\cdots z_k)^T \qquad (6\text{-}12)$$

On the other hand, if the distribution of a linearly profiled interference $\varphi(s)$ is known, it can be defined that

$$\varphi(s_j)=\sum_{l=1}^{k} z_l\varphi_l(s_j) \quad (j=1,2,\ldots,k) \qquad (6\text{-}13)$$

Equation (6-13) is a linear simultaneous equation group since φ_l is unit defined by equation (6-10). Thus, interference vector Z can be defined by a linear profiled interference in segments. Equation (6-13) shows that equations (6-11) and (6-12) are equivalent to each other based on equation (10).

6.5.4.2.2 Interface stiffness matrix A and displacement approach

Assuming that interference at an active node j of shrink-fitting interface is unit and the corresponding pre-deflection at die surface node i is defined as a_{ij}. Thus a matrix, referred to as interface stiffness matrix A, is defined

$$A = (a_{ij}) \tag{6-14}$$

by FE simulations, similar to the approach of obtaining interface compliance matrix B. Interface stiffness matrix A defines the relationship between die pre-deflection and interference on shrink-fitting interface. When interference vector defined by equation (6-12) is known, the corresponding die pre-deflection ξ_p is determined by

$$\xi_p = AZ \tag{6-15}$$

Especially, interference vector Z can be defined by the actual deflection ξ_r by equation (6-16) to compensate for die elasticity

$$AZ = -\xi_r \tag{6-16}$$

Basic difference between equation (6-6) and (6-16) is that the profiled interference obtained from them is different; dimensions of matrix A depend on the number of active nodes defined. Profiled interference from equation (6-6) may be complex and that from equation (6-16) is a linear profiled interference in segments. Therefore, combining equation (6-6) and (6-16) defines an approach to determine a linear profiled interference for die elasticity compensation. The combination is necessary; equation (6-6) defines the general form of the profiled interference; further, the necessary active nodes can be defined (e.g., $s_1 \sim s_4$ in Fig. 6.5) and equation (6-16) is used to define the values of the linear profiled interference. It is necessary to point out that solution of equation (6-16) also should satisfy inequalities (6-8) and (6-9). The iteration approach is similar to that presented in section 6.5.4.2.

6.6 Compensation for overall component-error by minimisation

6.6.1 Design variables and objective function

An optimum model consists of design variables, objective function and the constraints. Interference value x_i between nodal pair i at shrink-fitting interface is

chosen as design variable. Thus, all design variables consist of a design vector X in an n-dimensional space, as shown by equation (6-7).

Objective of optimisation is to try to acquire a design vector $X=(x_1 x_2 \cdots x_n)^T$ to be specified on shrink-fitting interface to minimise the overall component form-error, including those caused by die elasticity, temperature, Secondary Yielding and work-material elasticity. The objective is expressed as function of component-form error disparities and pre-deflection. Fig. 6.8 shows the geometric relation between component-form error disparity, pre-deflection and component-error. Now it is assumed that there are m nodes on die surfaces that may be in contact with billet and X_0 is a known initial profiled interference,

$$X = X_0 \tag{6-17}$$

Thus,

$$\begin{aligned} \xi_{pj} &= \xi_{pj}(X) \\ \phi_j &= \phi_j(X) \end{aligned} \tag{6-18}$$

ξ_{pj} on node j can be obtained from an elastic FE simulation and ϕ_j, from an elastic-plastic FE simulation. Component-error at node j can be expressed as

$$E_j = \phi_j(X) - \xi_{pj}(X) \tag{6-19}$$

Thus, component-error is a function of the profiled interference on shrink-fitting interface. The sum of squares of difference between ϕ_j and ξ_{pj} forms a function

$$T = \sum_{j=1}^{m} \alpha_j (\phi_j - \xi_{pj})^2 \tag{6-20}$$

If component-error at node j is not important, α_j can be set to a small value or zero, or a relatively large one. It is easy to know from equations (6-19) and (6-20) that T is the sum of squares of component-errors at all related die surface nodes when $\alpha_j = 1.0$.

In equation (6-19), component-from error disparity ϕ_j is dependent of die stiffness, work-material properties, die surface geometry, contact conditions and the profiled interference; pre-deflection ξ_{pj} is mainly determined by the specified interference on

shrink-fitting interface. $T=0$ means exactly $\phi_j=\xi_{pj}$ $(\alpha_j>0)$, or complete component-error compensation. Therefore, equation (6-20) can be used to design an optimum profiled interference vector X to minimise T. Equation (6-20) is, thus, defined as the objective function of the optimisation.

6.6.2 Constraints

Assembly conditions, manufacturing conditions and die surface strength, as well as the possibility of optimising process (too large interference may cause computational problems), must be taken into account when constraint functions are defined. Manufacturing conditions mean the profiled interference function must be selective. Usually, flat, cylindrical and conical surfaces can be easily manufactured. Thus, manufacturing constraints can be satisfied by choosing different profiled interference functions. Both assembly and die surface strength conditions can be satisfied by choosing suitable maximum interference. Therefore, the objective function (6-20) can be regarded as non-constraint by selecting suitable parameters.

6.6.3 Optimisation algorithm

6.6.3.1 Extended reverse algorithm

Obviously, if objective T reaches its minimum, from expression (6-20),

$$\frac{\partial T}{\partial x_k}=2\sum_{i=1}^{m}\alpha_i\left(\phi_i-\xi_{pi}\right)\left(\frac{\partial\phi_i}{\partial x_k}-\frac{\partial\xi_{pi}}{\partial x_k}\right)=0 \qquad (k=1,2,\ldots n) \qquad (6\text{-}21)$$

It should be noted that although both, ϕ_i and ξ_{pi}, are functions of X, ξ_{pi} is defined only by X for the given die dimensions; while ϕ_i depends on many other factors, such as Secondary Yielding, temperature, work-material elasticity. These factors are independent of X; it is also a fact that small change in die surface dimension changes component-errors, but not change the component-form error disparity; the change of ϕ_i caused by a change of X is, therefore, small; ϕ_i is almost a constant with respect to X. Thus, for simplicity of analysis, it is assumed in equation (6-21) that

$$\left|\frac{\partial\phi_i}{\partial x_k}\right|\approx 0 \qquad (k=1,2,\ldots,n) \qquad (6\text{-}22)$$

hence,
$$\frac{\partial \phi_i}{\partial x_k} - \frac{\partial \xi_{pi}}{\partial x_k} \approx -\frac{\partial \xi_{pi}}{\partial x_k} \tag{6-23}$$

and,
$$\frac{\partial T}{\partial x_k} \approx 2\sum_{i=1}^{m} \alpha_i \left(\phi_i - \xi_{pi}\right)\left(-\frac{\partial \xi_{pi}}{\partial x_k}\right) = 0 \quad (k = 1,2,...,n) \tag{6-24}$$

where
$$\frac{\partial \xi_{pi}}{\partial x_k} = \lim_{\delta x_k \to 0} \frac{\xi_{pi}(X + \delta X_k) - \xi_{pi}(X)}{\delta x_k} \tag{6-25}$$

and $\delta X_k = (0 0 ... \delta x_k ... 0)^T$. Differential $\frac{\partial \xi_{pi}}{\partial x_k}$ can be obtained by two-times elastic FE simulations. Assuming that $X^{(0)} = \left(x_1^{(0)} x_2^{(0)} .. x_n^{(0)}\right)^T$ is a known initial design vector in design space (6-7), the pre-deflection of which is ξ_{pi0}. $X = (x_1 x_2 ... x_n)^T$ is the optimum design vector which satisfies equation (6-21), the pre-deflection of which is ξ_{pi}. Let $X = X^{(0)} + \Delta X$. Obviously, if $X^{(0)}$ is a design vector sufficiently close to the optimum design vector, mathematically pre-deflection at X can be expressed as the sum of pre-deflection at $X^{(0)}$ and a perfect differential of pre-deflection at $X^{(0)}$,

$$\xi_{pi} = \xi_{pi0} + d\xi_{pi} \tag{6-26}$$

and
$$d\xi_{pi} = \sum_{j=1}^{n} \frac{\partial \xi_{pi0}}{\partial x_j} \Delta x_j \quad (i = 1,2,...,m) \tag{6-27}$$

Substituting equations (6-26) and (6-27) into equation (6-24), it can be obtained

$$\sum_{j=1}^{n}\left[\sum_{k=1}^{m} \alpha_k \left(\frac{\partial \xi_{pk}}{\partial x_i}\frac{\partial \xi_{pk0}}{\partial x_j}\right)\right]\Delta x_j = \sum_{k=1}^{m} \alpha_k \left(\phi_k - \xi_{pk0}\right)\frac{\partial \xi_{pk}}{\partial x_i} \tag{6-28}$$

Attention should be paid to equation (6-18) that ξ_{pi} is pre-deflection; it is a linear function of interference X. Thus, it can be obtained that

$$\frac{\partial \xi_{pk}}{\partial x_i} = \frac{\partial \xi_{pk0}}{\partial x_i} \tag{6-29}$$

Inserting equation (6-29) into (6-28) leads to

$$\sum_{j=1}^{n}\left[\sum_{k=1}^{m} \alpha_k \left(\frac{\partial \xi_{pk0}}{\partial x_i}\frac{\partial \xi_{pk0}}{\partial x_j}\right)\right]\Delta x_j = \frac{1}{2}\frac{\partial T}{\partial x_i} \quad (i = 1,2,...,n) \tag{6-30}$$

Equation (6-30) is a linear algebra equation group; its coefficient matrix α_{ij} is

$$a_{ij} = \sum_{k=1}^{m} \alpha_k \frac{\partial \xi_{pk0}}{\partial x_i} \frac{\partial \xi_{pk0}}{\partial x_j} \tag{6-31}$$

with right end term b_i $$b_i = \frac{1}{2}\frac{\partial T}{\partial x_i} = \sum_{k=1}^{m} \alpha_k \left(\phi_k - \xi_{pk0}\right) \frac{\partial \xi_{pk0}}{\partial x_i} \tag{6-32}$$

Equation (6-30) shows a fact that if an initial design point $X^{(0)}$ has been chosen, its increment to minimise component form-error can be determined by the numerical solution of equation (6-30), $\Delta X = \left(\Delta x_1\ \Delta x_2 \ldots \Delta x_n\right)^T$, thus, a new design vector

$$X = X^{(0)} + \Delta X \tag{6-33}$$

is defined for the minimisation of component-error. The significance of equation (6-30) is that, theoretically, the value of objective function T at X defined by equation (6-30) will be the lowest; thus X determined by equation (6-33) will be the optimum design vector, since X satisfies equation (6-30) and then also satisfies equation (6-21). However, three facts indicate that the solution can only be obtained by iteration. First, component-form error disparity ϕ_k in equation (6-22) is, more or less, related to the design variable X. Therefore, before the optimum design vector X is obtained, accurate component-form error disparity ϕ_k is remained unknown. Secondly, equations (6-31) and (6-32) show that all coefficient terms in equation (6-30) have to be defined by numerical simulations and are dependent on output accuracy of FE simulations. Lastly, equation (6-30) is based on a perfect differential equation (6-26), the accuracy of which depends on the choice of the initial design vector $X^{(0)}$. An iteration procedure is, therefore, developed in the following text for more accurate specification of the design vector X.

The subscripts i and j in equation (6-31) can exchange their position without changing the value of a_{ij}, or $a_{ij} = a_{ji}$. This shows that the coefficient matrix of the linear algebraic equation (6-30) is symmetric. The reverse algorithm was first proposed by Nshama [27], and developed by Hu et al. [28] in one-dimensional cases for measuring heat conductivity between contact surfaces. It is now extended into multi-dimensional cases and applied to the optimisation of die design.

6.6.3.2 Gradient approach

It is quite interesting to know from equation (6-30) that the right end term of equation group (6-30) also forms a search direction [29]:

$$B = \left(b_1\, b_2 \ldots b_n\right)^T = \frac{1}{2}\left(\frac{\partial T}{\partial x_1}\frac{\partial T}{\partial x_2}\cdots\frac{\partial T}{\partial x_n}\right)^T$$

along which the minimisation of objective value T is most effective at point $X^{(k)}$. Therefore,

$$\Delta X = \beta\left(b_1\, b_2 \ldots b_n\right)^T$$

is also an increment at $X^{(0)}$ for minimisation of T, where β is a searching step length which is determined in computation process [29]. This method is easy to program since there is no need to solve equation (6-30).

6.6.4 Combined compensation method

Considering the combined-influence of temperature, tool- and work-material elasticity and Secondary Yielding on component accuracy leads to difficulties in form-error compensation. For example, for some work-materials and dies, a negative dimensional-error may occur [8]. Obviously, a shrink-fitted die cannot be applied to compensate for negative component-error. There are other two cases that should be taken into account when the shrink-fitted die with profiled interference is applied for component-error compensation. If component error is small, the interference required for component accuracy should be also small. On the other hand, if component error is too large, the required interference for component-error compensation may lead to assembly difficulties; shrink-fitting stress may thus exceed the strength of tool material. All these cases require the following combined compensation method.

Compensating for component-error can be achieved by directly modifying die surface, referred to as direct die surface compensation. Combined compensation refers to shrink-fitting and *uniform* direct compensation simultaneously. A shrink-fitted die is used to compensate for positive component-errors, while direct compensation can be used for either positive or negative component-errors. Excessive pre-stress and assembly difficulties can be avoided for large compensation requirements. The other

reason for the use of the combined compensation method is the need to increase interference values occasionally.

6.6.5 Manufacturing considerations and interference linearisation

Similar to the analysis in section 6.5.4, the optimal profiled interference may be linearised considering manufacturing process. –refer to Fig. 6.5. The interference values of design variables can be re-chosen for the active nodes; interference values at those between active nodes are assumed to be linear.

6.7 Simulation procedures

6.7.1 Simulation procedure for die deflection compensation

Before a successful design of precision cold forming process, the designer may only know the required component specifications; the actual die surface deflection is unknown. In fact, die deflection is a function of the dimensions, structure, materials and the interference of die/tool. Therefore, before finalising the tool design, the die deflection cannot be accurately determined. During iteration, the actual die forming deflection, the required pre-deflection and the profiled interference that results in such a pre-deflection could be determined at the same time. The flow chart of simulation procedure is shown in Fig. 6.9. Actual die-deflection $\xi_r^{(0)}$ can be obtained by FE simulation under interference $X = X^{(0)}(=0)$ or any other possible initial values, and the corresponding shrink-fitting force $Y^{(1)}$ can be acquired by letting

$$BY^{(1)} = -\xi_r^{(0)} \tag{6-34}$$

Theoretically, corresponding to $Y = Y^{(1)}$ the interference should be

$$X = X^{(1)} \tag{6-35}$$

Again, the actual die deflection $\xi_r^{(1)}$ under $X^{(1)}$ should be simulated; the value of which may be different from $\xi_r^{(0)}$. If the difference between $\xi_r^{(1)}$ and $\xi_r^{(0)}$ is within requirement, the corresponding $Y = Y_1$ is the required shrink-fitting load vector. The search for the interference force vector corresponding to $\xi_r^{(1)}$ continues the iterative procedure till

$$Max\left|\delta_n^{(J-1)} - \delta_n^{(J)}\right| < \zeta \tag{6-36}$$

Obviously, in this way both the required profiled interference and the actual die deflection can be determined.

After the general profiled interference is determined by equation (6-6) and following the iteration procedure, the active nodes required by the linear profiled interference can be also defined; the displacement method can be applied to finalise the best linear profiled interference for the compensation of die deflection, considering the limitations of manufacturing process.

The algorithm for die elasticity compensation is summarised as follows: (1) forming interface force matrix B; (2) obtaining interference from equation (6-6) by nonlinear iterations; (3) determining the active nodes; (4) forming interface displacement matrix A; (5) obtaining the best linear profiled interference. Elastic-plastic simulations are employed only for a few times for the determination of the actual die surface deflection. All other simulations are elastic. Thus the whole process is costly effective, and the method is practical. The whole iteration procedure is shown in Fig. 6.9.

6.7.2 Optimum procedure

The simulation procedure for overall component-error compensation by minimisation technique is similar to that of die deflection compensation, including (1) optimisation without linearisation, (2) determination of the number of active nodes and their locations, and (3) the optimisation with linearisation.

The optimum procedures for both, the profiled interference with and without linearisation, are similar. The first cycle of optimisation

$$\min : T = \sum_{j=1}^{m} \alpha_j \left(\phi_j^{(0)} - \xi_{pj}^{(0)} \right)^2 \qquad (6\text{-}37)$$

starts from specifying an assuming profiled interference $X^{(0)}$ on the shrink-fitting interface. A new profiled interference $X^{(1)}$ can be determined by optimum cycle (6-37). Generally, the i^{th} cycle of optimisation

$$\min : T = \sum_{j=1}^{m} \alpha_j \left(\phi_j^{(i)} - \xi_{pj}^{(i)} \right)^2 \qquad (6\text{-}38)$$

can start from a previously determined profiled interference $X^{(i)}$, and a new profiled interference $X^{(i+1)}$ can be determined by the optimum cycle (6-38). If

$$\max_{1\le j\le m}\left|\phi_j^{(i)} - \xi_{pj}^{(i)}\right| < \varepsilon_1 \tag{6-39}$$

or

$$\left|\Delta T\right| < \varepsilon_2 \tag{6-40}$$

Table 6.1 Parameters used in simulations

Billet:	
Dimensions	Diameter Φ40.00 *mm* height Φ40.00*mm*
Material	E1CM Aluminium
Flow strength	$\sigma = 190(0.17+\varepsilon)^{0.29}$ (MPa)
Young's modulus	70 (MPa)
Poisson's ratio	0.33
Density	2700 $(kg\,m^{-3})$
Thermal parameters	Inelastic fraction 0.9 Expasion coefficient 2.875×10^{-5} (K^{-1}) Specific heat 896 $(J\,kg^{-1}K^{-1})$
Thermal conductivity	204 206 215 228 249 $(W\,m^{-1}K^{-1})$ 20 100 200 300 400 (K)
Die:	
Dimensions	See Fig. 6.9
Material	Steel
Young's modulus	210 GPa
Poisson's ratio	0.3
Density	7800 $(kg\,m^{-3})$
Thermal parameters	Inelastic fraction 0.9 Expasion coefficient 1.388×10^{-6} (K^{-1}) Specific heat 460 $(J\,kg^{-1}K^{-1})$ Thermal conductivity 50 $(W\,m^{-1}K^{-1})$
Parameters between die and billet	
Gap conductance	0 20×10^{3} $(W\,m^{-2}K^{-1})$ 0 300 (MPa)
Friction factor	0.05, 0.10, 0.15, 0.20 respectively

then, $X^{(i)}$ can be regarded as the optimum result; or starting the next minimisation process till condition (6-39) or (6-40) is satisfied. Flow chart for an optimum profiled interference, using linearised profile interference, is shown in Fig. 6.10. Convergent rate of the iteration is rapid; computation is costly effective since most of iterations only involve elastic FE simulations.

6.8 Material and related parameters used in FE simulation

E1CM aluminium was used in the FE simulations. The related parameters are listed in Table 6.1 [8]. Tooling and component geometry specifications are shown in Fig. 6.11.

6.9 Results

6.9.1 Results on die deflection compensation

Following the procedure specified in section 6.7.1, taking the tooling configuration and component shown in Fig. 6.11 as an example, the die elasticity compensation approach presented above was used to design a profiled interference for the die of a closed die-forging. Element type CAX4T is adapted to model both, the billet and the die, in thermo-mechanical coupled FE analysis [30]. All parameters used in simulations are shown in Table 6.1; the mesh used in FE analysis before and after forming are shown in Figs. 6.12a~b, respectively, to show the work-material flow pattern during cold forging. Different profiled interference functions under different friction factors were derived; an example of which is illustrated in Fig. 6.13. The corresponding linear profiled interference was also obtained, as shown in Fig. 6.14. Figs. 6.15~16 show the required pre-deflection and die deflection for specified linear profiled interference.

6.9.2 Results on die optimisation

An example of optimisation of a completely closed die-forging is presented to illustrate the feasibility of the developed optimisation algorithm. The approach was applied to optimise the die and component shown in Fig. 6.11 for overall component-error compensation. The results of the simulation are shown in Figs 6.17~6.27. Figs. 6.17~6.18 show the die surface pre-deflection and component-form error disparity by specifying a profiled interference on the interface, with and without combining uniform direct compensation. Figs. 6.19~6.20 show the obtained optimum profiled interference under different billet/die friction conditions and the corresponding component-errors by specifying the optimum profiled interference on the interface. Linear optimum profiled interference is illustrated in Fig. 6.21. The variation of component accuracy for different input parameters is illustrated in Figs. 6.23~6.27.

6.10 Discussions

6.10.1 Discussions on die deflection compensation

6.10.1.1 General profiled interference

Fig. 6.13 shows a general profiled interference for die elasticity compensation of a closed-die forging when die/billet interface friction factor $f = 0.10$. Other interference curves for $f = 0.05, 0.15$ and 0.20 have the similar pattern to this one. The form of the profiled interference shows that shrink-fitting forces on the interface are transferred mainly by the contacted active nodes, labelled by A, B, C and D, where A corresponds to O, D, to one end of the interface, and B and C are inter-middle points (refer to Fig. 6.13). The shrink-fitting force components of those nodes lying between active nodes were set to zero by the iteration procedure presented in Section 6.5. It was found that both, the number and locations of the active nodes, remain almost constant for finer or coarser mesh. In fact the number and location of active nodes are defined by the tooling configuration shown in Fig. 6.11a and the corresponding general mechanics model, shown by Fig. 6.2b. Therefore, the active nodes and their locations are independent of mesh pattern. However, finer mesh can be used to determine the active nodal locations more accurately, and this applies to elastic tools. If local plastic deformation is considered, both, the number and location of the active nodes, should refer to the mesh pattern.

Equation (6-6) is used to obtain the general profiled interference; the active nodes and their locations are defined. Thereafter, the displacement approach can be used to finalise the required linear profiled interference. This is a requirement of the combination of the unit force method and unit displacement approach.

It should be noted that although the shrink-fitting force vector components at those nodes between active ones were set to zero, the corresponding components of the profiled interference are usually not zero. –refer to Fig. 6.13; these are defined by the shrink-fitting force components at the active nodes or equation (6-3).

6.10.1.2 Linear profiled interference

The general profiled interference is characterised by the active nodes; further, the form of the linear profiled interference is defined by the active nodes and their locations. Active nodal locations are chosen as the locations where units of interference are specified. Therefore, linearly connecting interference at active nodes forms the linear profiled interference. However, the component value of the interference vector may not be the same as that of the general profiled interference at the corresponding active node; the displacement approach should be applied to determine the components of the interference vector.

Some results of linear profiled interference are illustrated in Fig. 6.14 with billet/die interface friction factor of $f = 0.05$, 0.10, 0.15 and 0.20 respectively. Obviously, these linear profiled interference curves represent a few truncated conical surfaces, which are easy to manufacture. In practice, it is still difficult to manufacture the active node position accurately, labelled with A, B and C.

6.10.1.3 Pre-deflection and die deflection after compensation

Fig. 6.15 shows the required die pre-deflection of the die surface without compensation. Billet/die interface friction influences the extent of die deflection. Therefore, the required pre-deflection for the compensation of die elasticity should be also different. This suggests that it may be difficult to completely compensate for die elasticity; billet/die interface friction is an elusive and changeable parameter which is a function of die and billet surfaces and lubrication conditions. Four cases of billet/die interface friction ($f = 0.05$, 0.10, 0.15 and 0.20) were considered, and the corresponding required pre-deflections are shown in Fig. 6.15.

Using the linear profiled interference curve, the forming die deflections were obtained, as shown in Fig. 6.16. Four curves labelled by 1~4 illustrate the actual die deflection when interference $X = 0$ (without pre-deflection) under friction factors $f = 0.05$, 0.10, 0.15 and 0.20 respectively. The group of curves labelled 5 is the actual die deflections with specified different linear profiled interference for the same range of friction factors. It has been shown that the difference for die elasticity compensation using

either the general profiled interference or linear profiled interference is negligible; the compensation accuracy of the both cases are almost identical, as long as the unit interference is specified for the active nodes. The final die deflection in this example can be controlled to within a few microns range. This shows that the profiled interference may be used to design shrink-fitting of dies to compensate for die elasticity.

In order to compensate for die elasticity, the maximum of interference values is in the order of one hundred microns. –refer to Figs. 6.13~6.14. This value may cause difficult in the assembly of die insert and stress-ring, depending on the assembly approach. However, if the influence of temperature, Secondary Yielding and billet elasticity is included in the compensation, the profiled interference values may not be so large.

6.10.2 Discussions on optimisation of forging die design

6.10.2.1 Translation displacement and compensation accuracy

Fig. 7.17 shows the pre-deflection and component-form error disparities by specifying an optimum profiled interference. As shown by equation (6-19), the difference between component-form error disparities and pre-deflection is the component-error. Therefore, effective compensation of component-error depends on the match between pre-deflection and component-from error disparities. If the component-form error disparity curve is translated a suitable distance $\pm\bar{u}$ upward or downward, i.e., $\phi_j \pm \bar{u}$ is taken as component-form error disparity at node j, the profiled interference X, which matches the pre-deflection to component-form error disparity, can be found, as shown in Fig. 6.18, where $\bar{u} = 50$ microns. It is obvious that a suitable value of $\pm\bar{u}$ can effectively improve the compensation requirement of the component. $\pm\bar{u}$ is referred to as *translation displacement*, being positive or negative depending on the component-form error disparity and its distribution. Using this combined compensation method, the final component-errors for axisymmetric components can be reduced to within a few microns. By selecting a suitable translation displacement, the required accuracy of the component can be achieved; interference values can be specified to enable easy assembly and the required die surface pre-stress.

Precision forgings with minimum working stresses is the objective of many research programmes [1-2,19,22,27]. However, efforts in this research only focus on attaining precision.

6.10.2.2 Optimum profiled interference and its linearisation

Fig. 6.19 shows the optimum profiled interference corresponding to billet/die interface friction factors 0.05, 0.10, 0.15 and 0.20 respectively, without linearisation of the profiled interference and with $\bar{u} = 50\,\mu m$. Fig. 6.20 shows the distribution of component-errors at different forming stages by specifying the optimum-profiled interference on the shrink-fitting interface. The first group of curves shows the component-errors when punch reaches its lowest position. Die surface contracts after withdraw of punch; the radial dimension of workpiece is reduced due to this secondary yielding [7] which leads to the group of curves labelled with 2. The workpiece expands after ejection due to work-material elasticity, which is shown by the group of curves labelled with 3. And finally complete cooling down results in the fourth group of curves which shows the final component-errors; these are almost constant -50 μm. This is the translation displacement value $\bar{u}$; if a 50 μm uniform direct die surface compensation is made beforehand, the final component errors will be within a few microns.

The linearised optimum interference is shown in Fig. 6.21 for frictional factors 0.05, 0.10, 0.15, and 0.20 respectively. FE simulations show that using the linearised profiled interference, the accuracy of component-error compensation is almost the same as that without linearisation. However, the choice of which nodes as design variables, – the active nodes, is critical; it is a result of observation of optimum profiled interference without linearisation. Therefore, both optimisations, with and without linearisation, are necessary.

6.10.2.3 Factors influencing component accuracy

The optimum result discussed above is theoretical. There are many factors that will influence the optimisation of component accuracy in practice, for example the

accuracy of forming parameters, such as friction coefficient, material properties, die manufacturing and forging stroke.

6.10.2.3.1 Friction

Friction is an uncertain but critical factor. Friction factor affects the flow of work-material in the die cavity, which leads to disparities of strain distribution in the component. Therefore, different friction factors may lead to components having different springback, die-deflection and contraction after retraction of the punch. Fig. 6.22 shows different component-form error disparities corresponding to different friction factors for the same die, billet and profiled interference. This illustrates why different friction condition requires different optimum profiled interference on shrink-fitting interface. Curve 3 in Fig. 6.23 shows the component errors with optimum interference when friction factor is 0.10 with translation displacement $\bar{u} = 50\mu m$. Curves 1 and 2 show the component-errors with the same interference when friction factor is 0.08 and 0.09 respectively; and curves 4, 5 and 6, when friction factor is 0.11,0.12 and 0.13 respectively. A 10% of friction factor variation may lead to about one micron component-error in this example. This shows the influence of friction on component accuracy.

6.10.2.3.2 Forging stroke

Optimum profiled interference discussed above is obtained under given stroke at which die cavity is just fully filled. Determination of this stroke accurately needs some skills in FE simulations. As have been known, stroke is a key factor to influence die-deflection in closed die forging although most of this influence is compensated for by Secondary Yielding [7]. Fig. 6.24 shows this influence, where curve 1 is the final component-error under optimum interference for a selected stroke (translation displacement $\bar{u} = 20\mu m$), and curve 2, 3, 4 are the final component-error curves when stroke has an increment of 0.7%, 2.0% and 3.5% respectively. If the accuracy of stroke can be controlled within 1%, then the influence on final component-error will be within 2 μm in this example. The volume accuracy of billet for precision forging is usually controlled within $\pm 0.5\%$ [32]. Thus, relative forming stroke varies with billet volume which further influences component accuracy. Errors

in the stroke would raise forging force in closed die forging, which may results in tool damage.

6.10.2.3.3 Material properties

Many factors can influence the accuracy of work material properties, such as the composition and its distribution, heat-treatment, deformation history, and even material data measuring procedure. Material with identical designation, or even from the same batch may differ. It is, therefore significant to discuss the influence of material property variation on component accuracy. Fig. 6.25 shows this influence. Curve 3 is the final component-error under optimum profiled interference when friction factor is 0.10 and the translation displacement is $\bar{u} = 50\mu m$ for material property of $\bar{\sigma} = 190(0.17 + \bar{\varepsilon})^{0.29} MPa$. If material property is changed into 80%, 90%, 110% and 120% of the defined value, the final component-errors are shown by curve 5, 4, 2 and 1 respectively. 10% of variation of material property may lead to about $5\,\mu m$ variation of component-error. This means the accuracy of material data has a significant influence on final component accuracy. Since the elasticity is constant, higher forming stresses lead to bigger springback; this is shown in Fig. 6.26. The variation of material property causes a forming stress variation of $\Delta\sigma$, which leads to a springback variation of $\Delta\varepsilon$. Material properties also influence die deflection, secondary yielding and temperature induced. All these affect the component accuracy.

6.10.2.3.4 Thermal properties

Thermal properties concern the heat conductivity in the material and heat conductance at the contact interface. Thermal contact conductance influences temperature distribution inside the workpiece and die, and further influences the dimensions of the component by thermal expansion or contraction. Therefore, the thermal contact property may affect component accuracy. Curve 2 in Fig. 6.27 is the component-error for the thermal contact conductance listed in Table 6.1 with optimum profiled interference; curve 1 and 3 are component-errors with 50% and 150% of the specified thermal contact conductance. It appears that the influence of thermal conductance on component-error is not significant. The main reason for this is that the temperature

difference between the billet and die is small and the contact time is short. For those with long time contact and severe friction, accuracy of thermal contact property may play important part and would affect the accuracy of the forging.

6.11 Conclusions

(1) Profiled interference is more effective to be specified on shrink-fitting interface for die elasticity or overall component-error compensation than in uniform interference; the approaches to design this profiled interference, analytical algorithm or optimisation, have been established. Die deflection can be controlled into a straight contour, and overall component-error under different billet/die friction conditions can be reduced to within a few microns.

(2) When shrink-fitting die is used, direct modification of die surfaces for compensation is replaced by modification of outside surfaces of the insert; this reduces the cost of the compensation procedure.

(3) By choosing suitable translation displacement and specifying an optimum profiled interference on the interface, it is possible to obtain sufficient pre-stress on die surface and satisfactory component accuracy.

(4) Critical factors that affect component-error are the accuracy of work material properties, friction coefficient, forging stroke and accuracy of billet volume. 10% variation of friction coefficient, or 0.5% variation of forging stroke, or 2% variation of work-material property may result in a one-micron component-error respectively. Stable and high component accuracy is based on more accurate and stable friction conditions, material properties, forging stroke, and billet volume.

(5) Linearisation of optimum profiled interference would simplify manufacture of dies. Component-error compensation by shrink-fitting die is easier than direct die surface compensation.

(6) Most iterations involve only elastic FE simulations; therefore the design procedure is inexpensive.

6.12 References

1. K. Lange, Handbook of Metal Forming, pp. 15.1-15.99, McGraw-Hill, Inc. 1985
2. A.O.A.Ibhadode, On A Method for Die Container Design in Completely Closed Die Forging, Transactions of the ASME, Vol. 119, pp. 438-440, 1997
3. J. Groenbaek and E. B. Nielsen, New Developments in the Design of High Performance, Strip-Wound Cold Forging Tools, Journal of Materials Processing Technology, Vol. 46, pp. 87-97, 1994
4. X. Lu and R. Balendra Evaluation of FE Models for the Calculation of Die-Cavity Compensation, Journal of Materials Processing Technology, Vol. 58, No. 2-3, pp. 212-216, 1996
5. Y. Qin and R. Balendra, FE simulation of the Influence of Die-Elasticity on Component Dimension in Forward Extrusion, International Journal of Machine Tools and Manufacture, Vol. 37, No. 2, pp. 183-192, 1997
6. M. Knoerr, K. Lange and T. Altan, Fatigue Failure of Cold Forging Tooling: Causes and Possible Solutions Through Fatigue Analysis, Journal of Materials Processing Technology, Vol. 46, pp. 57-71, 1994
7. A. Rosochowski and R. Balendra, Effect of Secondary Yielding on Nett-Shape Forming , Journal of Materials Processing Technology, Vol. 58, No. 2-3, pp. 145-152, 1996
8. H.Long and R.Balendra, The Influence of Thermal and Elastic Effects of the Accuracy of Cold-Formed Components, Proceedings of the Thirty-Second International MATADOR Conference, pp. 361-366, 1997
9. R. Balendra, Y. Qin, X. Lu, Analysis, Evaluation and Compensation of Component-Errors in the Nett-Forming of Engineering Components, Journal of Materials Processing Technology 106: (1-3) 204-211 OCT 31 2000
10. H. Ou, R. Balendra, Die-Elasticity for Precision Forging of Aerofoil Sections Using Finite Element Simulation , Journal of Materials Processing Technology, 76: (1-3) 56-61 APR 1998

11. A.O.A.Ibhadode and T.A.Dean, The Influence of Process Variables on Load and Accuracy When Forging in A Completely Closed Cavity Die, Proceedings of the Institution of Mechanical Engineers, Vol. 202, No. B4, pp. 237-245, 1988
12. W. Qiang,, et al., Strength Analysis and Optimisation for Both the Cylinder and the Anvil of A Belt-Type Ultra-High-Pressure Apparatus by FEM, Journal of Materials Processing Technology, 1995, Vol. 55, No. 1, pp. 5-10
13. J. S. Jinn and S. L. Rong, Optimum die surface design of general 3-dimensional section extrusions by using a surface model with tension parameter, International journal of machine tools and manufacture, 1991, Vol. 31, No. 4, pp. 521-537
14. N. V. Reddy, P. M. Dixit and G. K. Lal, Die design for axisymmetric extrusion, Journal of materials processing technology, 1995, Vol. 55, No. 3-4, pp. 331-339
15. S. W. Lo, An efficient method of designing controlled strain rate dies for extrusions, Journal of the Chinese institute of engineers, 1996, Vol. 19, No. 5, pp. 623-631
16. W. A. Gifford, the use of three-dimensional computational fluid dynamics in the design of extrusion dies, Journal of reinforced plastics and composites, 1997, Vol. 16, No. 7, pp. 661-674
17. A. Morita, S. Hattori, etc., Near nett shape forging of titanium-alloy turbine blade, ISIJ, international, 1991, Vol. 31, No. 8, pp. 827-833
18. S. Sheng and L. Y. Guo, Preform design of axisymmetrical forgings based on reverse simulation technique of die forging process, Journal of materials processing technology, 1992, Vol. 34, No. 1-4, pp. 346-356
19. R. Lapovok, Improvement of die life by minimisation of damage accumulation and optimisation of preform design, Journal of materials processing technology, 1998, Vol. 80-1, pp. 608-612
20. S. Roy, S. Ghosh and R. Shivpuri, A New Approach to Optimal Design of Multi-Stage Metal Forming Processes with Micro Genetic Algorithms, International Journal of Machine Tools & Manufacture, Vol. 37, No. 1, pp. 29-44, 1997
21. B. Falk, U. Engel and M. Geiger, Estimation of tool life in bulk metal forming based on different failure concepts, Journal of materials processing technology, Vol. 80-81, pp. 602-607, 1998

22. M. R. Jensen, F. F. Damborg, etc., Optimisation of the draw-die design in conventional deep-drawing in order to minimise tool wear, Journal of materials processing technology, 1998, Vol. 83, No. 1-3, pp. 106-114
23. G. Q. Zhao, E. Wright and R. V. Grandhi, Sensitivity analysis based preform die shape design for nett-shape forging, International journal of machine tools and manufacture, 1997, Vol. 37, No. 9, pp. 1251-1271
24. S. Badrinarayanan and N. Zabaras, A sensitivity analysis for the optimum design of metal-forming processes, Computer methods in applied mechanics and engineering, 1996, Vol. 129, No. 4, pp. 319-348
25. T. Wanheim, R. Balendra and Y. Qin, Extrusion die for in-process compensation of component-errors due to die-elasticity, Journal of materials processing technology, 1997, Vol. 72, No. 2, pp. 177-182
26. D. Johnson, Advanced Structural Mechanics: An Introduction to Continuum Mechanics and Structural Mechanics, London: Tomas Telford, 2000
27. W. Nshama, J. Jeswiet and P. H. Oosthuizen, Evaluation of temperature and heat-transfer conditions at the metal-forming interface, Journal of materials processing technology, 1994, Vol. 45, No. 1-4, pp. 637-642
28. Z. M. Hu, J. W. Brooks and T. A. Dean, The interfacial heat transfer coefficient in hot die forging of titanium alloy, Proceedings of the institution of mechanical engineers, part C-Journal of mechanical engineering science, 1998, Vol. 212, No. 6, pp. 485-496
29. Jean-Baptiste Hiriart-Urruty, Werner Oettli and Josef Stoer, Optimisation: Theory and Algorithms, Dekker, 1983
30. Hibbitt, Karisson and Sorensen, Inc., 1992, ABAQUS Manual.
31. T. A. Dean, Precision forging, Proceeds of the Institution of Mechanical Engineers Part C-Journal of Engineering Science, 214: (1) 113-126 200

Appendix 6.1

The transformation of interface compliance matrix at different mesh patterns

There are three possible forms for the interface compliance matrix B :

(1) $n > m$ means that there are more nodes on shrink-fitting surface than those on die surface; therefore, the unknowns in equation (6-6) are more than the number of equations. Mathematically, this means there are infinite solutions that can satisfy equation (6-6). Practically, this means there are different combination of the profiled interference values by which the required constraints on die surfaces can be satisfied. In this case, it is possible to arbitrarily chose $n-m$ nodes on shrink-fitting surface and let the shrink-fitting force on these nodes to be any given permissible constant. This enables the unknowns in equation (6-6) equal to the required constraints on die surface. Thus, the $m \times n$ matrix B is transformed into a $m \times m$ square and a unique solution of Y can be determined.

(2) $n = m$ means n equations to determine n unknowns. Mathematically, a unique profiled interference can be obtained from equation (6-6).

(3) $n < m$ means that the nodal number on shrink-fitting surface is less than that on die surface and the number of equations in equation group (6-6) is more than that of unknowns. Mathematically, there is no solution that can satisfy all the equations in (6-6). Practically, this means no matter what kind of profiled interference is specified on shrink-fitting interface, it is impossible to satisfy all the die surface constraints at the same time. However, if $m-n$ constraints on die surface are released, i.e., letting $m-n$ nodes on die surfaces be free to deflect; or $m-n$ equations are deleted from equation group (6-6), then the unknowns and constraints will be equal, and the coefficient matrix of the equation group (6-6) is transformed into a $n \times n$ square matrix. In practice, we can choose those die-surface nodes to be free, the deflection of which is not important to the component accuracy.

Appendix 6.2

Nonlinear iteration for solution of equation (6-6)

In order to establish the approach to obtain non-negative solution from equation (6-6), it is necessary to know what is the practical meaning of a negative component in solution of equation (6-6). Fig. 6.4 illustrates a possible negative component; with blank circle to show the actual die surface deflection and solid circle to show the required pre-deflection. Assuming that the pre-deflection at node i of die surfaces is $-\delta_i$ and there is a $p_j < 0$ at corresponding shrink-fitting surface node j. It is understandable that all other nodal forces $p_k > 0$ $(k \neq j)$ in the shrink-fitting surface enable the pre-deflection at node i to be bigger than necessary, especially for those nodal loads in the vicinity of node j, thus a $p_j < 0$ at node j is required to satisfy

$$b_{i1}p_1 + b_{i2}p_2 + \cdots + b_{in}p_n = -\delta_i$$

Attention should be paid to the fact that $p_j < 0$ means tension stress is being provided by node j due to shrink-fitting, which means node j should be glued onto the shrink-fitting surface of the stress-ring. This is not practical; shrink-fitting structure can only provide $p_j \geq 0$, at extreme case $p_j = 0$. Obviously, the negative loads are resulted from the requirements of all constraints on die surface nodes; mathematically, therefore, an $p_j < 0$ in the solution of equation group (6-6) means the die surface deflection is at least one-nodal overconstrained.

Considering that shrink-fitting structure can only provide $p_j \geq 0$, $p_j = 0$ can be used to replace $p_j < 0$ in the solution of equation (6-6). At the same time, since the die surface is overconstrained by equation (6-6), therefore, an equation should be deleted from equation group (6-6). As a consequence, one constraint in die surface can not be satisfied; n-dimensional equation group (6-6) is simplified into an n-1 dimensional; the deflection of a die surface node will be free; the location of this constraint can be any node on die surface.

The above mathematical analysis shows a fact that not any arbitrary required pre-deflection can be formed by shrink-fitting die; die elasticity compensation accuracy will be related to the distribution of the actual die deflection. Some of distributed actual die deflections may be exactly compensated mathematically; others may not. However, approximate solution is always available and obtainable.

If there are other $p_j < 0$ in the new $n-1$ unknowns equation group, the above procedure should be repeated until equation (6-8) or (6-9) is satisfied. This is the mathematical procedure of non-linear iteration of equation (6-6) for a non-negative solution. Unfortunately, the constraints on some nodes on die surface, which is hoped to remain, may also be abandoned by this iteration approach. Efforts should be made in this case to keep the constraints which are critical, and abandon those which are not if necessary by the following approach.

It is assumed that constraint on node i must be retained and its corresponding load on shrink-fitting surface node j is $p_j < 0$, just as shown in Fig. 6.4. It is a fact in this case that there must be some other nodal loads greater than zero near node j, such as $p_{j+1}, p_{j+2}, p_{j-1}, p_{j-2}\cdots$, etc., as shown in Fig. 6.4, which makes the absolute pre-deflection at die surface node i larger than $|-\delta_i|$ and thus leads to $p_j < 0$. Therefore, cancelling a closest constraint, the nodal load of which is positive, may leads to $p_j > 0$. This ideal leads to the basic iteration process for a non-negative solution from equation (6-6).